

# On the use of deep learning for phase recovery

Kaiqiang Wang<sup>1,2,3,\*</sup>, Li Song<sup>1</sup>, Chutian Wang<sup>1</sup>, Zhenbo Ren<sup>2</sup>, Guangyuan Zhao<sup>3</sup>, Jiazen Dou<sup>4</sup>, Jianglei Di<sup>4</sup>, George Barbastathis<sup>5</sup>, Renjie Zhou<sup>3</sup>, Jianlin Zhao<sup>2,\*</sup>, and Edmund Y. Lam<sup>1,\*</sup>

<sup>1</sup>Department of Electrical and Electronic Engineering, The University of Hong Kong, Hong Kong SAR, China

<sup>2</sup>School of Physical Science and Technology, Northwestern Polytechnical University, Xi'an, China

<sup>3</sup>Department of Biomedical Engineering, The Chinese University of Hong Kong, Hong Kong SAR, China

<sup>4</sup>School of Information Engineering, Guangdong University of Technology, Guangzhou, China

<sup>5</sup>Department of Mechanical Engineering, Massachusetts Institute of Technology, Cambridge, Massachusetts, USA

\*Correspondence: Kaiqiang Wang (kqwang.optics@gmail.com) or Jianlin Zhao (jlzhao@nwpu.edu.cn) or Edmund Y. Lam (elam@eee.hku.hk)

## Abstract

Phase recovery (PR) refers to calculating the phase of the light field from its intensity measurements. As exemplified from quantitative phase imaging and coherent diffraction imaging to adaptive optics, PR is essential for reconstructing the refractive index distribution or topography of an object and correcting the aberration of an imaging system. In recent years, deep learning (DL), often implemented through deep neural networks, has provided unprecedented support for computational imaging, leading to more efficient solutions for various PR problems. In this review, we first briefly introduce conventional methods for PR. Then, we review how DL provides support for PR from the following three stages, namely, pre-processing, in-processing, and post-processing. We also review how DL is used in phase image processing. Finally, we summarize the work in DL for PR and outlook on how to better use DL to improve the reliability and efficiency in PR. Furthermore, we present a live-updating resource (<https://github.com/kqwang/phase-recovery>) for readers to learn more about PR.

## 1. Introduction

Light, as a complex electromagnetic field, has two essential components: amplitude and phase<sup>1</sup>. Optical detectors, usually relying on photon-to-electron conversion (such as charge-coupled device sensors and the human eye), measure the intensity that is proportional to the square of the amplitude of the light field, which in turn relates to the transmittance or reflectance distribution of the sample (Fig. 1a and Fig. 1b). However, they cannot capture the phase of the light field because of their limited sampling frequency<sup>2</sup>.

Actually, in many application scenarios, the phase rather than the amplitude of the light field carries the primary information of the samples<sup>3–6</sup>. For quantitative structural determination of transparent and weakly scattering samples<sup>3</sup> (Fig. 1c), the phase delay is proportional to the sample's thickness or refractive index (RI) distribution, which is critically important for bioimaging because most living cells are transparent. For quantitative characterization of the aberrated wavefront<sup>5</sup> (Fig. 1d and Fig. 1e), the phase aberration is caused by atmospheric turbulence with an inhomogeneous RI distribution in the light path, which is mainly used in adaptive aberration correction. Also, for quantitative measurement of the surface profile<sup>6</sup> (Fig. 1f), the phase delay is proportional to the surface height of the sample, which is very useful in material inspection.

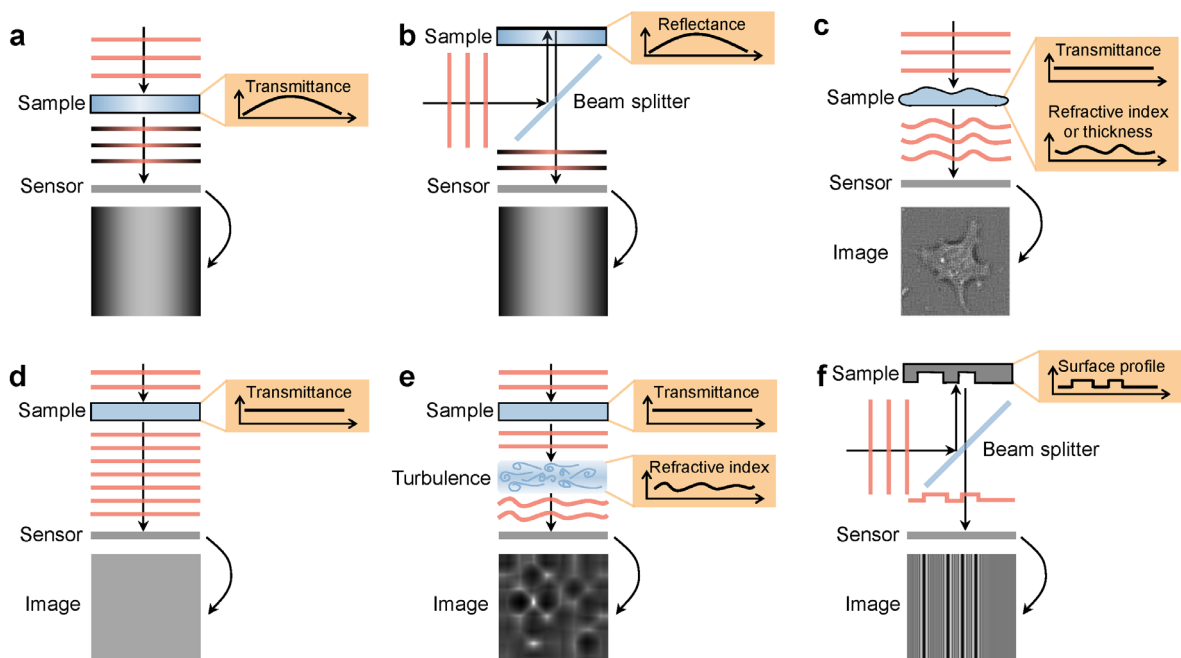


**Fig. 1 Light is transmitted through or reflected from different samples.** **a** An absorptive sample with a nonuniform transmittance distribution. **b** A reflective sample with a nonuniform reflectance distribution. **c** A transparent (weakly-absorbing) sample with a nonuniform RI or thickness distribution. **d** A sample with a

uniform transmittance distribution. **e** A sample with a uniform transmittance distribution placed before atmospheric turbulence with inhomogeneous RI distribution. **f** A reflective sample with a nonuniform surface height distribution.

Since the phase delay across the wavefront is necessary for the above applications, but the optical detection devices can only perceive and record the amplitude of the light field, how can we recover the desired phase? Fortunately, as the light field propagates, the phase delay also causes changes in the amplitude distribution; therefore, we can record the amplitude of the propagated light field and then calculate the corresponding phase. This operation generally comes under different names according to the application domain; for example, it is quantitative phase imaging (QPI) in biomedicine<sup>3</sup>, phase retrieval in coherent diffraction imaging (CDI)<sup>4</sup> which is the most commonly used term in x-ray optics and non-optical analogues such as electrons and other particles, and wavefront sensing in adaptive optics (AO)<sup>5</sup> for astronomy and optical communications. Here, we collectively refer to the way of *calculating the phase of a light field from its intensity measurements* as phase recovery (PR).

As is common in inverse problems, calculating the phase directly from an intensity measurement after propagation is usually ill-posed<sup>7</sup>. Suppose the complex field at the sensor plane is known. We can directly calculate the complex field at the sample plane using numerical propagation<sup>8</sup> (Fig. 2a). However, in reality, the sensor only records the intensity but loses the phase, and, moreover, it is necessarily sampled by pixels of finite area size; because of these complications, the complex field distribution at the sample plane generally cannot be calculated in a straightforward manner (Fig. 2b).

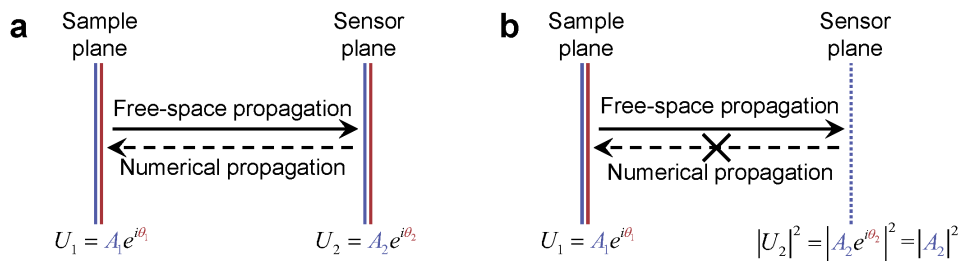


**Fig. 2 Calculating complex field at the sample plane from (a) the complex field or (b) the intensity at the sensor plane.  $U$ : complex field.  $A$ : amplitude.  $\theta$ : phase.**

We can transform phase recovery into a well-posed/deterministic problem by introducing extra information, such as holography or interferometry at the expense of having to introduce a reference wave<sup>8,9</sup>, transport of intensity equation requiring multiple through-focus amplitudes<sup>10,11</sup>, and Shack-Hartmann wavefront sensing which introduces a micro-lens

array at the conjugate plane<sup>12,13</sup>. Alternatively, we can solve this ill-posed phase recovery problem in an iterative manner by optimization, i.e., the so-called phase retrieval such as Gerchberg-Saxton-Fienup algorithm<sup>14–16</sup>, ptychographic iterative engine<sup>17,18</sup>, and Fourier ptychography<sup>19</sup>. Next, we introduce these classical phase recovery methods in more detail.

**Holography/interferometry.** By interfering the unknown wavefront with a known reference wave, the phase difference between the object wave and the reference wave is converted into the intensity of the resulting hologram/interferogram due to alternating constructive and destructive interference of the two waves across their fronts. This enables direct calculation of the phase from the hologram<sup>8</sup>.

In in-line holography, where the object beam and the reference beam are along the same optical axis, four-step phase-shifting algorithm is commonly used for phase recovery (Fig. 3)<sup>20</sup>. At first, the complex field of the object wave at the sensor plane is calculated from the four phase-shifting holograms. Next, the complex field at the sample plane is obtained through numerical propagation. Then, by applying the arctangent function over the final complex field, a phase map in the range of  $(-\pi, \pi]$  is obtained, i.e., the so-called wrapped phase. The final sample phase is obtained after phase unwrapping. Other multiple-step phase-shifting algorithms are also possible for phase recovery<sup>21</sup>. Spatial light interference microscopy (SLIM), as a well-known QPI method, combines the phase-shifting algorithm with a phase contrast microscopy for phase recovery over transparent samples<sup>22</sup>.

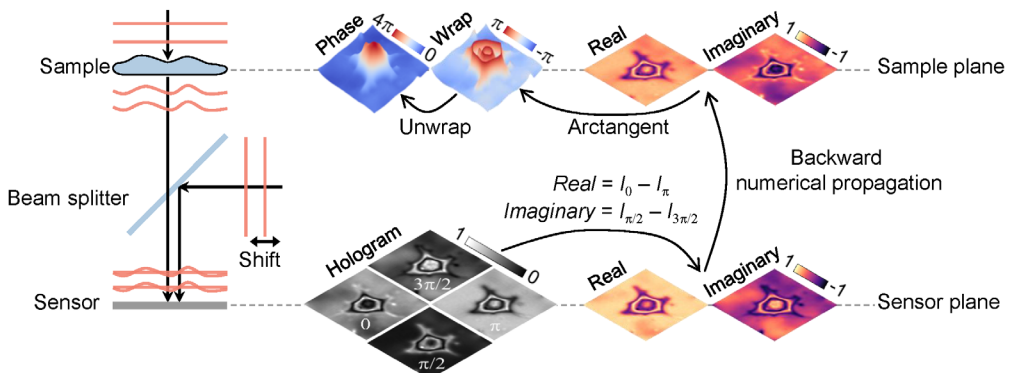


**Fig. 3 Description of in-line holography based on the four-step phase-shifting algorithm.**

In off-axis holography, where the reference beam is slightly tilted from the optical axis, the phase is modulated into a carrier frequency that can be recovered through spatial spectral filtering with only one holographic measurement (Fig. 4)<sup>23</sup>. By appropriately designing the carrier frequency, one can well separate the baseband that contains the reference beam from the object beam. After transforming the measured hologram into the spatial frequency

domain through a Fourier transform (FT), we can select the +1<sup>st</sup> or -1<sup>st</sup> order beam and move it to the baseband. By applying an inverse FT, the complex sample beam can be retrieved. One has to be careful, however, not to exceed the Nyquist limit on the camera as the angle between reference and object increases. Moreover, as only a small part of the spatial spectrum is taken for phase recovery, off-axis holography typically wastes a lot of spatial bandwidth product of the system. To enhance the utilization of the spatial bandwidth product, the Kramers-Kronig relationship and other iterative algorithms have been recently applied in off-axis holography<sup>24–26</sup>.

Both the in-line and off-axis holography discussed above are lensless, where the sensor and sample planes are not mutually conjugate. Therefore a backward numerical propagation from the former to the latter is necessary. The process of numerical propagation can be omitted if additional imaging components are added to conjugate the sensor plane and the sample plane, such as digital holographic microscopy<sup>27</sup>.

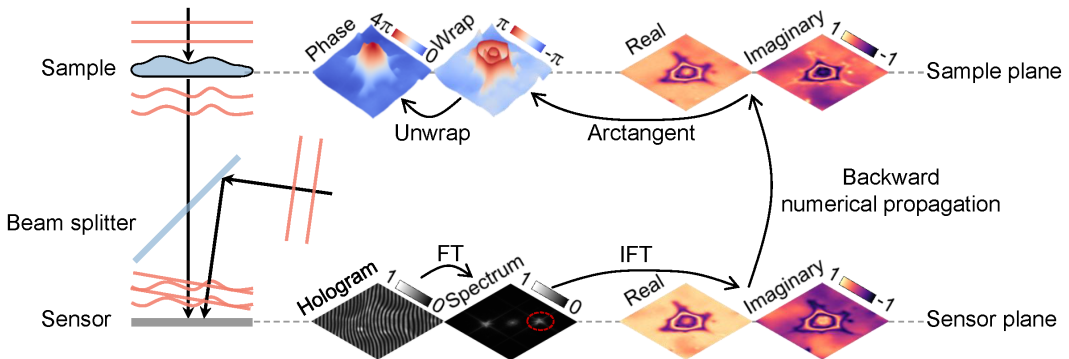


**Fig. 4 Description of off-axis holography based on spatial spectral filtering.**

**Transport of Intensity Equation.** For a light field, the wavefront determines the axial variation of the intensity in the direction of propagation. Specifically, there is a quantitative relationship between the gradient and curvature of the phase and the axial differentiation of intensity, the so-called transport of intensity equation (TIE)<sup>10</sup>. This relationship has an elegant analogy to fluid mechanics, approximating the light intensity as the density of a compressible fluid and the phase gradient as the lateral pressure field. TIE may be derived from the Fresnel-Schrödinger<sup>10</sup>, and it is subject to the scalar, paraxial, and weak-defocusing approximations<sup>28,29</sup>. The gradient and curvature of the phase together determine the shape of the wavefront, whose normal vector is then parallel to the wavevector at each point of the wavefront, and consequently to the direction of energy propagation. In turn, variations in the lateral energy flux also result in axial variations of the intensity. Convergence of light by a convex lens is an intuitive example (Fig. 5): the wavefront in front of the convex lens is a

plane, whose wavevector is parallel to the direction of propagation. As such, the intensity distribution on different planes is constant, that is, the axial variation of the intensity is equal to zero. Then, the convex lens changes the wavefront so that all wavevectors are directed to the focal point, and therefore as the light propagates, the intensity distribution becomes denser and denser, meaning that the intensity varies in the axial direction (equivalent, its axial derivative is not zero).

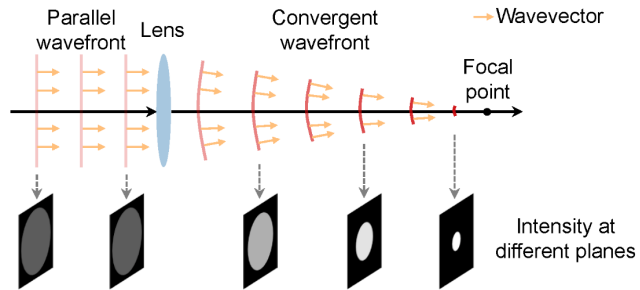


Fig. 5 A convex lens converges light to a focal point.

As there is a quantitative relationship between the gradient and curvature of the phase and the axial differentiation of intensity, we can exploit it for phase recovery (Fig. 6). By shifting the sensor axially, intensity maps at different defocus distances are recorded, which can be used to approximate the axial differential by numerical difference, and thus calculate the phase through TIE. Due to the addition of the imager, the sensor plane and the sample plane are conjugated.

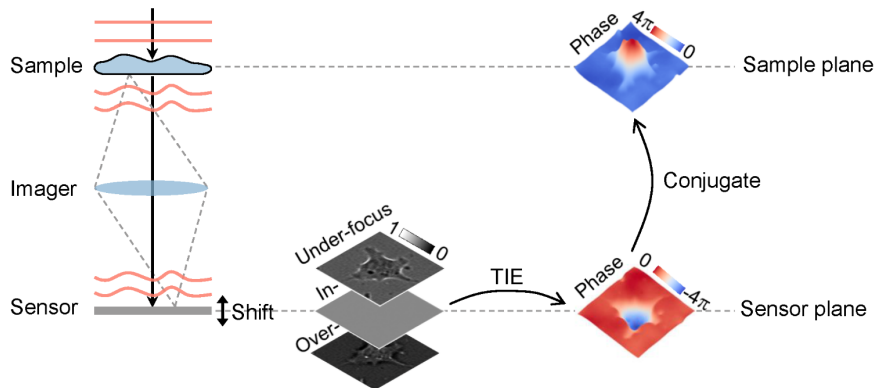


Fig. 6 Description of phase recovery by transport of intensity equation (TIE).

It is worth noting that TIE is suitable for a complete and partially coherent light source, and the resulting phase is continuous and does not require phase unwrapping, while it is only effective in the case of paraxial approximation and weak defocus<sup>11</sup>.

**Shack-Hartmann wavefront sensing.** If we can obtain the horizontal and vertical phase gradients of a wavefront in some ways, then the phase can be recovered by integrating the

phase gradients in these orthogonal directions. Shack-Hartmann wavefront sensor<sup>12,13</sup> is a classic way to do so from the perspective of geometric optics. It usually consists of a microlens array and an image sensor located at its focal plane (Fig. 7). The phase gradient of the wavefront at the surface of each microlens is calculated linearly from the displacement of the focal point on the focal plane, in both horizontal and vertical ( $x$ -axis and  $y$ -axis) directions. The phase can then be computed by integrating the gradient at each point, whose resolution depends on the density of the microlens array. In addition, quantitative differential interference contrast microscopy<sup>30</sup>, quantitative differential phase contrast microscopy<sup>31</sup>, and quadriwave lateral shearing interferometry<sup>32</sup> also recover the phase from its gradients. There may achieve higher resolution than the Shack-Hartmann wavefront sensor.

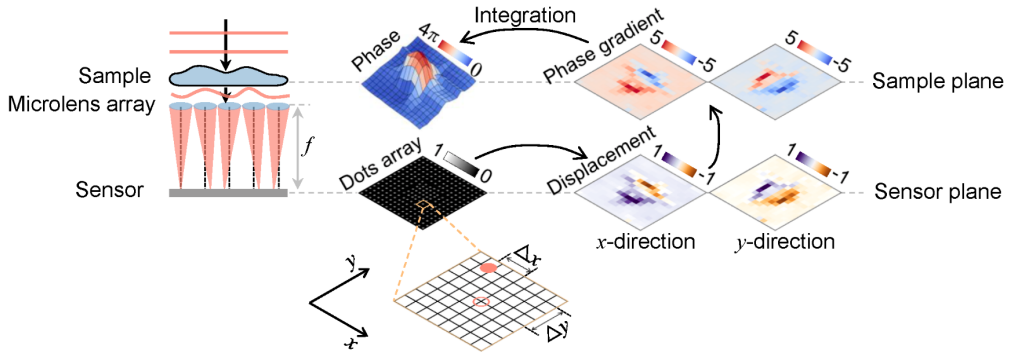
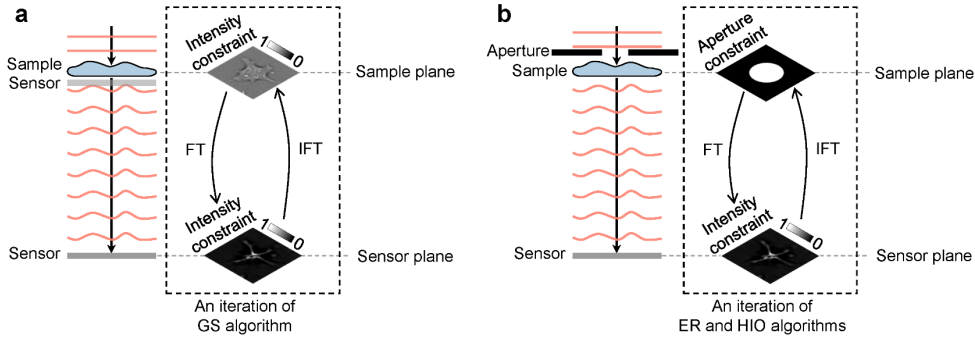


Fig. 7 Description of the Shack-Hartmann wavefront sensor.

**Phase retrieval.** If extra information is not desired to be introduced, then calculating the phase directly from a propagated intensity measurement is an ill-posed problem. We can overcome such difficulty through incorporating prior knowledge. This is also known as regularization. In the Gerchberg-Saxton (GS) algorithm<sup>14</sup>, the intensity at the sample plane and the far-field sensor plane recorded by the sensor are used as constraints. A complex field is projected forward and backward between these two planes using the Fourier transform and constrained by the intensity iteratively; the resulting complex field will gradually approach a solution (Fig. 8a). Fienup changed the intensity constraint at the sample plane to the aperture (support region) constraint, so that the sensor only needs to record one intensity map, resulting in the error reduction (ER) algorithm and the hybrid input-output (HIO) algorithm (Fig. 8b)<sup>15,16</sup>.



**Fig. 8 Description of alternating-projection algorithms.** **a** Gerchberg-Saxton algorithm. **b** Error reduction and hybrid input-output algorithms.

Naturally, if more intensity maps are recorded by the sensor, there will be more prior knowledge for regularization, further reducing the ill-posedness of the problem. By moving the sensor axially, the intensity maps of different defocus distances are recorded as an intensity constraint, and then the complex field is computed iteratively like the GS algorithm (Fig. 9a)<sup>33–35</sup>. In this axial multi-intensity alternating projection method, the distance between the sample plane and the sensor plane is usually kept as close as possible, so that numerical propagation is used for projection instead of Fourier transform. Meanwhile, with a fixed position of the sensor, multiple intensity maps can also be recorded by radially moving the aperture near the sample, and then the complex field is recovered iteratively like the ER and HIO algorithms (Fig. 9b), the so-called ptychographic iterative engine (PIE)<sup>17,18</sup>. In this radial multi-intensity alternating projection method, each adjoining aperture constraint overlaps one another. Furthermore, angular multi-intensity alternating projection is also possible. By switching the aperture constraint from the spatial domain to the frequency domain, multiple intensity maps with different frequency information are recorded by changing the angle of the incident light (Fig. 9c), the so-called Fourier ptychography (FP)<sup>19</sup>.

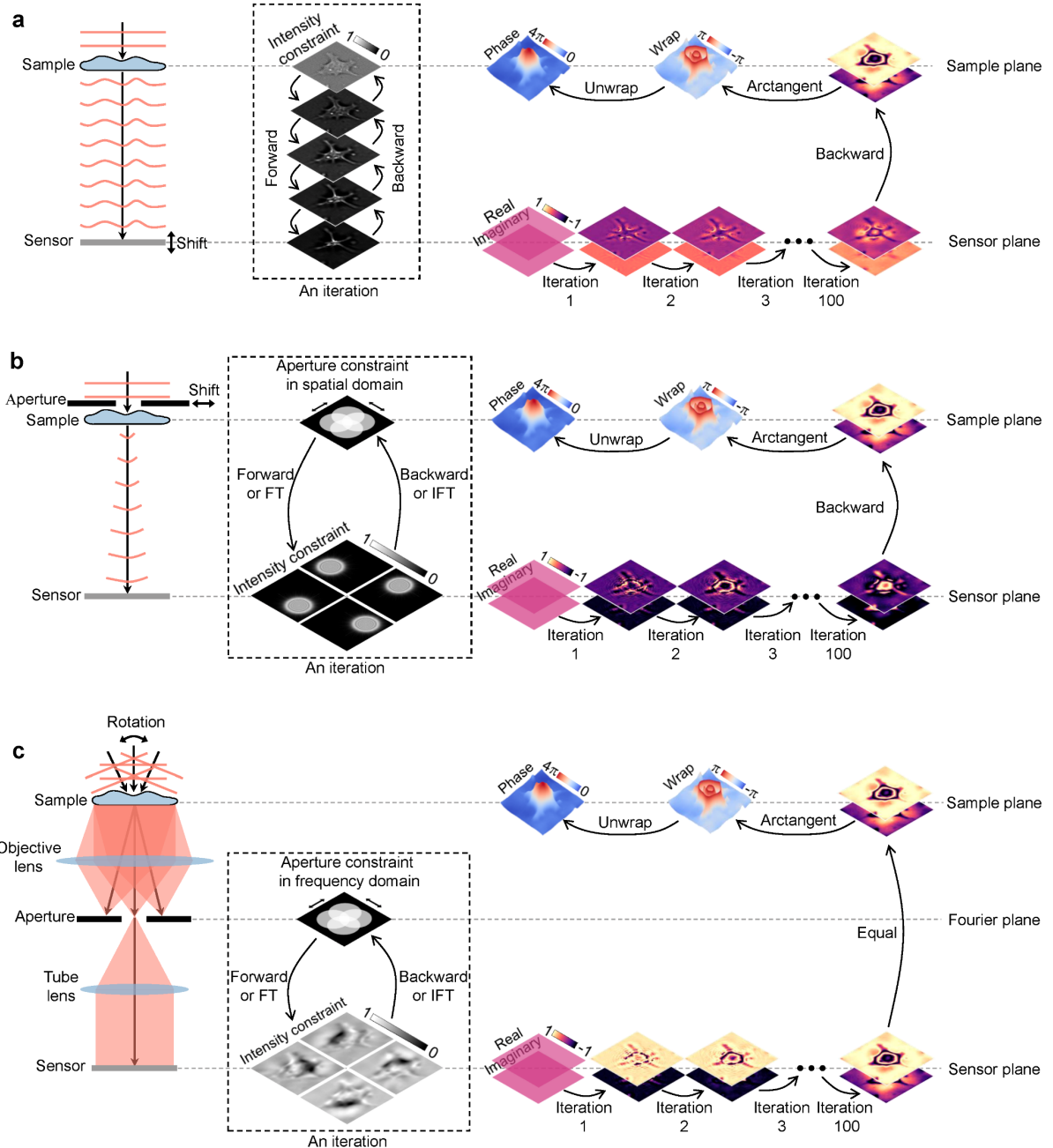


**Fig. 9 Description of multi-intensity alternating projection.** **a** Axial multi-intensity alternating projection. **b** Radial multi-intensity alternating projection. **c** Angular multi-intensity alternating projection. “Forward”: forward numerical propagation. “Backward”: backward numerical propagation.

In addition to alternating projections, there are two most representative non-convex optimization methods, namely the Wirtinger flow<sup>36</sup> and truncated amplitude flow algorithms<sup>37</sup>. They can be transformed into convex optimization problems through semidefinite programming, such as the PhaseLift algorithm<sup>38</sup>.

**Deep learning (DL) for phase recovery.** In recent years, as an important step towards true artificial intelligence (AI), deep learning<sup>39</sup> has achieved unprecedented performance in

many tasks of computer vision with the support of graphics processing units (GPUs) and large datasets. Similarly, since it was first used to solve the inverse problem in imaging in 2016<sup>40</sup>, deep learning has demonstrated good potential in the field of computational imaging<sup>41</sup>. In the meantime, there is a rapidly growing interest in using deep learning for phase recovery (Fig. 10).

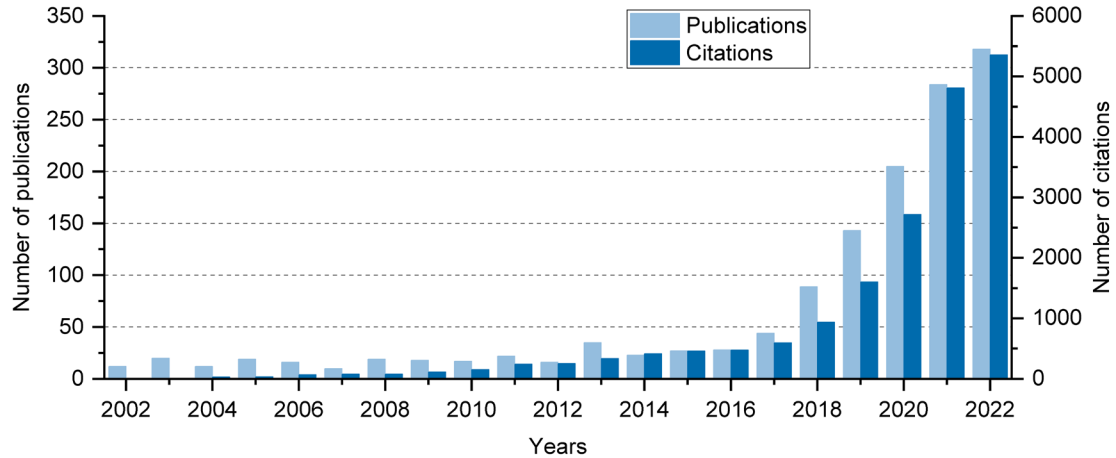


**Fig. 10 Growth in interest in using "deep learning for phase recovery" overtime is depicted by the number of publications and citations on Web of Science.** The used search code is “TS=((“phase recovery” OR “phase retrieval” OR “phase imaging” OR “holography” OR “phase unwrapping” OR “holographic reconstruction” OR “hologram” OR “fringe pattern”) AND (“deep learning” OR “network” OR “deep-learning”))”.

For the vast majority of “DL for PR”, the implementation of deep learning is based on the training and inference of artificial neural networks (ANNs)<sup>42</sup> through input-label paired dataset, known as supervised learning (Fig. 11). In view of its natural advantages in image processing, the convolutional neural network (CNN)<sup>43</sup> is the most widely used ANN for phase recovery. Specifically, in order for the neural network to learn the mapping from physical quantity  $A$  to  $B$ , a large number of paired examples need to be collected to form a training dataset that implicitly contains this mapping relationship (Fig. 11a). Then, the gradient of the loss function is propagated backward through the neural network, and the network parameters are updated iteratively, thus internalizing this mapping relationship (Fig. 11b). After training, the neural network is used to compute  $B_x$  from an unseen  $A_x$  (Fig. 11c). In this way, deep learning has been used in all stages of phase recovery and phase processing.

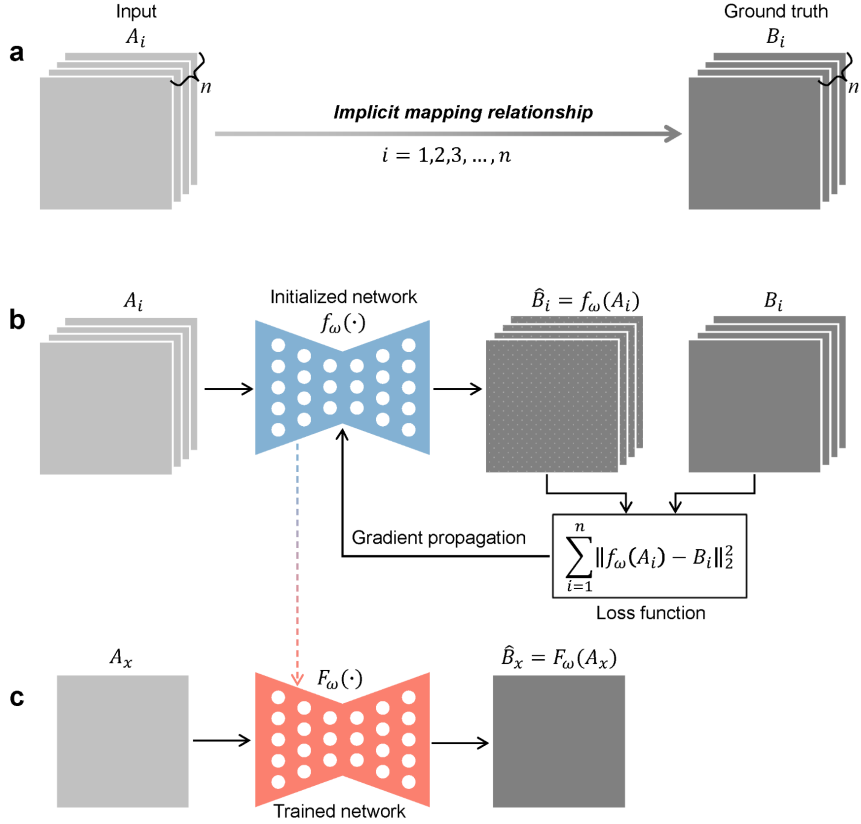


**Fig. 11 Implementation of deep learning with paired dataset and supervised learning.** **a** Datasets collection. **b** Network training. **c** Inference via a trained network.  $\omega$ : the parameters of the neural network,  $n$ : the sample number of the training dataset.

In fact, the rapid pace of deep-learning-based phase recovery has been documented in several excellent review papers. For example, Barbastathis *et al.*<sup>44</sup> and Rivenson *et al.*<sup>45</sup> reviewed how supervised deep learning powers the process of phase retrieval and holographic reconstruction. Zeng *et al.*<sup>46</sup> and Situ *et al.*<sup>47</sup> mainly focused on the use of deep learning in digital holography and its applications. Wang *et al.*<sup>48</sup> reviewed and compared different usage strategies of deep learning in phase unwrapping. Dong *et al.*<sup>49</sup> introduced a unifying framework for various algorithms and applications from the perspective of phase retrieval and presented its advances in machine learning. Differently, depending on where the neural network is used, we review various methods from the following four perspectives:

- In *DL-pre-processing for PR* (Section 2), the neural network performs some pre-processing on the intensity measurement before phase recovery, such as pixel super-resolution (Fig. 12a), noise reduction, hologram generation, and autofocusing.

- In *DL-in-processing for PR* (Section 3), the neural network directly performs phase recovery (Fig. 12b) or participates in the process of phase recovery together with the physical model or physics-based algorithm.
- In *DL-post-processing for PR* (Section 4), the neural network performs some post-processing after phase recovery, such as noise reduction (Fig. 12c), resolution enhancement, aberration correction, and phase unwrapping.
- In *DL for phase processing* (Section 5), the neural network uses the recovered phase for specific applications, such as segmentation (Fig. 12d), classification, and imaging modal transformation.

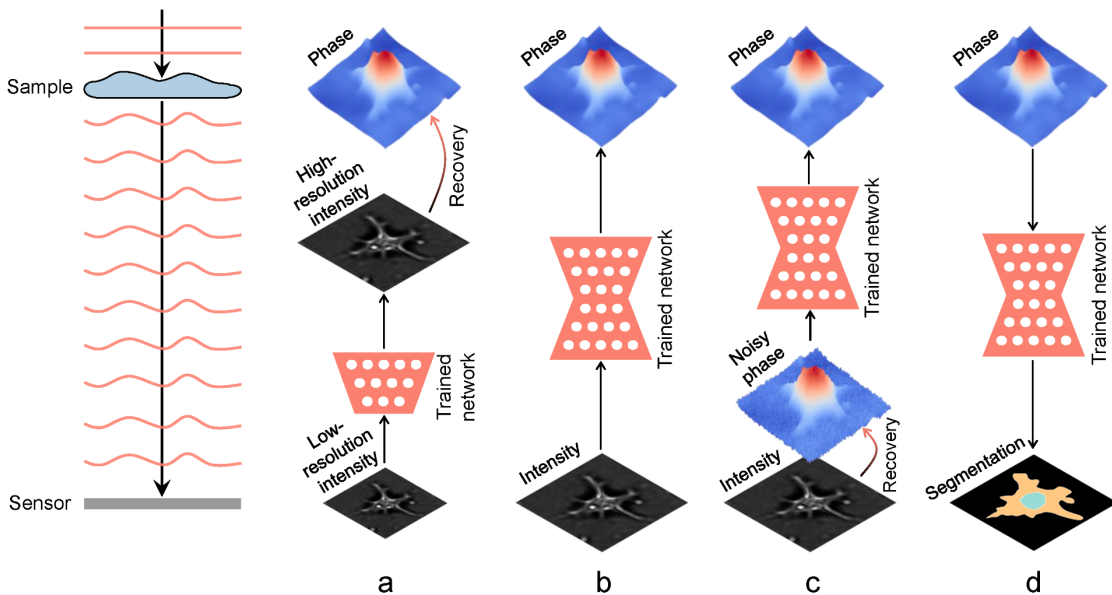


**Fig. 12** Overview example of “deep learning (DL) for phase recovery (PR) and phase processing”. **a** DL-pre-processing for PR. **b** DL-in-processing for PR. **c** DL-post-processing for PR. **d** DL for phase processing.

Finally, we summarize how to effectively use deep learning in phase recovery and look forward to potential development directions (Section 6). To let readers learn more about phase recovery, we present a live-updating resource (<https://github.com/kqwang/phase-recovery>).

## 2. DL-pre-processing for phase recovery

A summary of “DL-pre-processing for phase recovery” is presented in Table 1 and is described below, including pixel super-resolution (Section 2.1), noise reduction (Section 2.2), hologram generation (Section 2.3), and autofocusing (Section 2.4).

**Table 1** Summary of “DL-pre-processing for phase recovery”

Task	Reference	Input	Output	Network	Training dataset	Loss function
Pixel resolution super-resolution	Luo <i>et al.</i> <sup>50</sup>	Sub-pixel LR holograms	HR hologram	U-Net	Expt. and Sim.: 1,600 pairs	SSIM
	Byeon <i>et al.</i> <sup>51</sup>	LR hologram	HR hologram	SRCNN	Sim.: 192 pairs	$l_2$ -norm
	Xin <i>et al.</i> <sup>52</sup>	LR hologram	HR hologram	Fast SRCNN	Sim.: 5,000 pairs	$l_2$ -norm
	Ren <i>et al.</i> <sup>53</sup>	LR hologram	HR hologram	ResNet and SubPixelNet	Expt.: 800 pairs	$l_2$ -norm
Noise reduction	Yan <i>et al.</i> <sup>54</sup>	Noisy fringe pattern	Noise-free fringe pattern	DnCNN	Sim.: 80,000 pairs	$l_1$ -norm
	Lin <i>et al.</i> <sup>55</sup>	Noisy fringe pattern	Noise-free fringe pattern	CNN	Sim.: 230,400 pairs	$l_2$ -norm
	Hao <i>et al.</i> <sup>56</sup>	Noisy fringe sub-pattern	Noise-free fringe sub-pattern	FFDNet	Sim.: 1,200 pairs	$l_2$ -norm
	Zhou <i>et al.</i> <sup>57,58</sup>	Noisy fringe pattern	Noise-free fringe pattern	Spectral CNN	Sim.: 1,200 pairs	---
	Reyes-Figueroa <i>et al.</i> <sup>59</sup>	Noisy fringe pattern	Noise-free fringe pattern	U-Net and ResNet	Sim.: 25,000 pairs	$l_1$ -norm
	Gurrola-Ramos <i>et al.</i> <sup>60</sup>	Noisy fringe pattern	Noise-free fringe pattern	U-Net and DenseNet	Sim.: 1,500 pairs	$l_1$ -norm
Hologram generation	Zhang <i>et al.</i> <sup>61,62</sup>	Hologram	Phase-shifting holograms	Y-Net	Sim.: ---	$l_2$ -norm
	Yan <i>et al.</i> <sup>63</sup>	Hologram	Single phase-shifting hologram	ResNet	Sim: 12,000 pairs	GAN loss
	Zhao <i>et al.</i> <sup>64</sup>	Hologram	Phase-shifting holograms	MPRNet	Sim.: ---	Charbonnier and Edge
	Huang <i>et al.</i> <sup>65</sup>	Hologram	Phase-shifting holograms	Y-Net	Expt.: 4,000 pairs	$l_2$ -norm
	Wu <i>et al.</i> <sup>66</sup>	Hologram	Single phase-shifting hologram	U-Net	Sim.: 6,400 pairs	GAN loss
	Luo <i>et al.</i> <sup>67</sup>	Hologram	Multi-distance holograms	U-Net	Sim.: 440 pairs	GAN loss
	Li <i>et al.</i> <sup>68</sup>	Hologram	Hologram with another wavelength	U-Net	Sim.: 20,000 pairs	GAN loss
	Li <i>et al.</i> <sup>69</sup>	Two holograms	Hologram with another wavelength	Y-Net	Sim.: 8,000 pairs	$l_1$ -norm
	Xu <i>et al.</i> <sup>70</sup>	dual-wavelength hologram	Two single-wavelength holograms	U-Net	Sim.: 1,800 pairs	$l_2$ -norm
	Pitkäaho <i>et al.</i> <sup>71</sup>	Hologram	Defocus distance (21 types)	AlexNet	Expt. and sim.: 485,856 pairs	Cross entropy
Autofocusing	Ren <i>et al.</i> <sup>72</sup>	Hologram	Defocus distance (5 types)	CNN	Expt.: > 5,000 pairs	Cross entropy
	Son <i>et al.</i> <sup>73</sup>	Hologram	Defocus distance (10 types)	CNN	Sim.: 40,180 pairs	Cross entropy
	Couturier <i>et al.</i> <sup>74</sup>	Hologram	Defocus distance (101 types)	DenseNet	Expt.: 7,000 pairs	Cross entropy
	Ren <i>et al.</i> <sup>75</sup>	Hologram (amplitude or phase object)	Defocus distance	CNN	Expt.: 5,000 and 2,000 pairs	$l_1$ -norm
	Pitkäaho <i>et al.</i> <sup>76</sup>	Hologram (cells)	Defocus distance	AlexNet and VGG	Expt.: 437,271 pairs	$l_2$ -norm
	Jaferzadeh <i>et al.</i> <sup>77</sup> and Moon <i>et al.</i> <sup>78</sup>	Hologram (single cell)	Defocus distance	CNN	Expt.: 3,000 and 2,400 pairs	$l_2$ -norm
	Tang <i>et al.</i> <sup>79</sup>	Fixed tensor	Defocus distance	MLP (untrained)	Expt.: 1	$l_2$ -norm
	Cuenat <i>et al.</i> <sup>80,81</sup>	Hologram (USAF 1951)	Defocus distance	ViT	Expt.: 104,400 pairs Sim.: 40,000 pairs	log cosh
	Lee <i>et al.</i> <sup>82</sup>	Spatial spectrum	Defocus distance	CNN	Sim.: ---	$l_2$ -norm
	Shimobaba <i>et al.</i> <sup>83</sup>	1/4 power spectrum	Defocus distance	CNN	Sim.: ---	$l_2$ -norm

“---” indicates not available. “LR” is short for low-resolution. “HR” is short for high-resolution. “Expt.” is short for experiment. “Sim.” is short for simulation. “GAN loss” means training the network in an adversarial generative way. “MLP” is short for multi-layer perceptron.

## 2.1 Pixel super-resolution

A high-resolution image generally reveals more detailed information about the object of interest. Therefore, it is desirable to recover a high-resolution image from one or multiple

low-resolution measurements of the same field of view, a process known as pixel super-resolution. Similarly, from multiple sub-pixel-shifted low-resolution holograms, a high-resolution hologram can be recovered by pixel super-resolution algorithms<sup>84</sup>. Luo *et al.*<sup>50</sup> proposed to use the U-Net for this purpose. Compared with iterative pixel super-resolution algorithms, this deep learning method has an advantage in inference time while ensuring a same level of resolution improvement, and maintains high performance even with a reduced number of input low-resolution holograms.

After the pixel super-resolution CNN (SRCNN) was proposed for single-image super-resolution in the field of image processing<sup>85</sup>, this type of deep learning method was also used in other optical super-resolution problems, such as brightfield microscopy<sup>86</sup> and fluorescence microscopy<sup>87</sup>. Similarly, this method of inferring corresponding high-resolution images from low-resolution versions via deep neural networks can also be used for holograms pixel super-resolution before doing phase recovery by conventional recovery methods (Fig. 13).

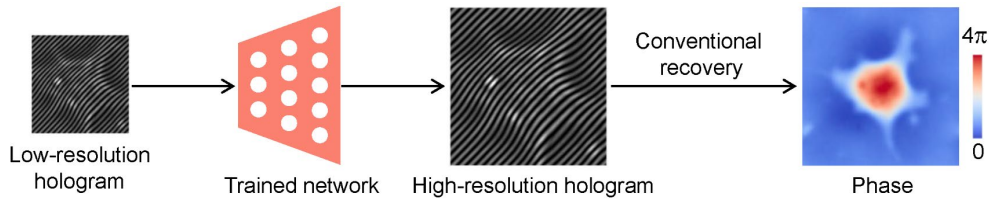


Fig. 13 Description of deep-learning-based hologram super-resolution.

Byeon *et al.*<sup>51</sup> first applied the SRCNN to hologram pixel super-resolution, and named it HG-SRCNN. Compared with conventional focused-image-trained SRCNN and bicubic interpolation, this method, trained with defocus in-line holograms, can infer higher-quality high-resolution holograms. Xin *et al.*<sup>52</sup> used an improved fast SRCNN (FSRCNN) to do pixel super-resolution for white-light holograms, significantly improving the identification and accuracy of three-dimensional (3D) measurement results. Under the premise of improved accuracy, the inference speed of FSRCNN is nearly ten times faster than that of SRCNN.

Ren *et al.*<sup>53</sup> proposed to use a CNN, incorporating the residual network (ResNet) and sub-pixel network (SubPixelNet), for pixel super-resolution of a single off-axis hologram. They found that compared to  $l_1$ -norm and structural similarity index (SSIM)<sup>88</sup>, the neural network trained using  $l_2$ -norm as the loss function performed best. Moreover, this deep learning method reconstructs high-resolution off-axis holograms with better quality, compared with conventional image super-resolution methods, such as bicubic, bilinear, and nearest-neighbor interpolations.

## 2.2 Noise reduction

Most phase recovery methods, especially holography, are performed with a coherent light source; therefore, coherent noise is an unavoidable issue. In addition, noise can be caused by environmental disturbances and the recording process of the image sensor. Therefore, it is very important to reduce the noise from the hologram before phase recovery. Filter-based methods, such as windowed Fourier transform (WFT)<sup>89</sup>, have been widely used in hologram noise reduction, but most of these methods face a trade-off between good filtering performance and time cost.

In 2017, Zhang *et al.*<sup>90</sup> opened the door to image denoising using the deep CNN, called DnCNN. Subsequently, the DCNN was introduced to the field of fringe analysis for fringe pattern denoising (Fig. 14).

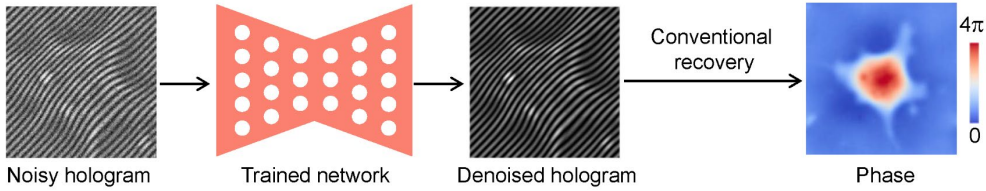


Fig. 14 Description of deep-learning-based hologram noise reduction.

Yan *et al.*<sup>54</sup> first applied the DnCNN to fringe pattern denoising, which has higher precision around image boundaries and needs less inference time than WFT. Similar conclusions can also be seen in the work of Lin *et al.*<sup>55</sup>. Then, inspired by the FFDNet<sup>91</sup>, Hao *et al.*<sup>56</sup> downsampled the input fringe pattern into four sub-images before using the DnCNN for denoising, leading to a faster inference speed. Furthermore, Zhou *et al.*<sup>57,58</sup> converted this batch-denoising DnCNN into the frequency domain. Specifically, they first computed the Fourier transform of the downsampled sub-images, and then used the DnCNN to achieve noise reduction in the frequency domain, and finally applied upsampling and inverse Fourier transform to obtain the denoised fringe pattern. From the comparison results, their method outperforms that of Yan *et al.* and Hao *et al.* at different noise levels. Reyes-Figueroa *et al.*<sup>59</sup> further showed that the U-Net and its improved version (V-Net) are better than DnCNN for fringe pattern denoising, because their proposed V-Net has more channels on the outer side than on the inner side, retaining more details. Given the U-Net's outstanding mapping capabilities, Gurrola-Ramos *et al.*<sup>60</sup> also improved it for fringe pattern denoising, where dense blocks are leveraged for reusing feature layers, local residual learning is used to address the vanishing gradient problem, and global residual learning is used to estimate the noise of the image instead of the denoised image directly. Compared with other neural

networks mentioned above, it has a minor model complexity while maintaining the highest accuracy.

### 2.3 Hologram generation

As mentioned in Introduction, in order to recover the phase, multiple intensity maps are needed in many cases, such as phase-shifting holography and axial multi-intensity alternating projection. Given its excellent mapping capability, the neural network can be used to generate other relevant holograms from known ones, thus enabling phase recovery that requires multiple holograms (Fig. 15). In this approach, the input and output usually belong to the same imaging modality with high feature similarity, so it is easier for the neural network to learn. Moreover, the dataset is collected only by experimental record or simulation generation, without the need for phase recovery as ground-truth in advance by conventional methods.

Zhang *et al.*<sup>61,62</sup> first proposed the idea of generating holograms with holograms before phase recovery with the conventional method (Fig. 15a). From a single hologram, the other three holograms with  $\pi/2$ ,  $\pi$ , and  $3\pi/2$  phase shifts were simultaneously generated by the Y-Net<sup>92</sup>, and then phase recovery was implemented by the four-step phase-shifting method. The motivation to infer holograms instead of phase via a network is that for different types of samples, the spatial differences between their holograms were significantly lower than that of their phase. Accordingly, this phase recovery based on the hologram generation has better generalization ability than recovering phase from holograms directly with the neural network, especially when the spatial characteristics differences of the phase between the training and testing datasets are relatively large<sup>62</sup>. Since the phase-shift between the generated holograms are equal, Yan *et al.*<sup>63</sup> proposed to generate noise-free phase-shifting holograms using a simple end-to-end generative adversarial network (GAN) in a manner of sequential concatenation. Subsequently, for better performance in balancing spatial details and high-level semantic information, Zhao *et al.*<sup>64</sup> applied the multi-stage progressive image restoration network (MPRNet)<sup>93</sup> for phase-shifting hologram generation. Huang *et al.*<sup>65</sup> and Wu *et al.*<sup>66</sup> then expanded this approach from four-step to three-step and two-step phase-shifting methods, respectively.

Luo *et al.*<sup>67</sup> proposed to generate holograms with different defocus distances from one hologram via a neural network, and then achieve phase recovery with alternating projection (Fig. 15b). Similar to the work of Zhang *et al.*<sup>62</sup>, they proved that the use of neural networks with less difference between the source domain and the target domain could enhance the generalization ability. As for multi-wavelength holography, Li *et al.*<sup>68,69</sup> harnessed a neural

network to generate a hologram of another wavelength from one or two holograms of known wavelength, thereby realizing two-wavelength and three-wavelength holography. At the same time, Xu *et al.*<sup>70</sup> realized a one-shot two-wavelength and three-wavelength holography by generating the corresponding single-wavelength holograms from a two-wavelength or three-wavelength hologram with information crosstalk.

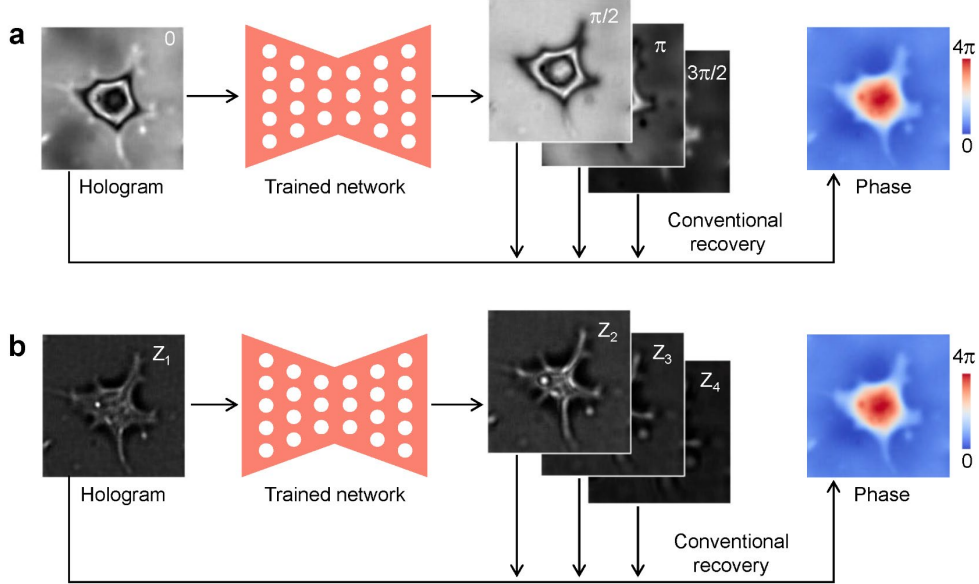


Fig. 15 Description of deep-learning-based hologram generation for (a) phase-shifting method and (b) axial multi-intensity alternating projection method.

## 2.4 Autofocusing

In lensless holography, the phase of the sample plane can only be recovered if the distance between the sensor plane and the sample plane is known. Defocus distance estimation thus becomes a fundamental problem in holography, which is also known as autofocusing.

Deep learning methods for autofocus essentially use the neural network to estimate the defocus distance from the hologram (Fig. 16), which can be regarded as either a classification problem<sup>71–74</sup> or a regression problem<sup>75–78,80–83</sup>.

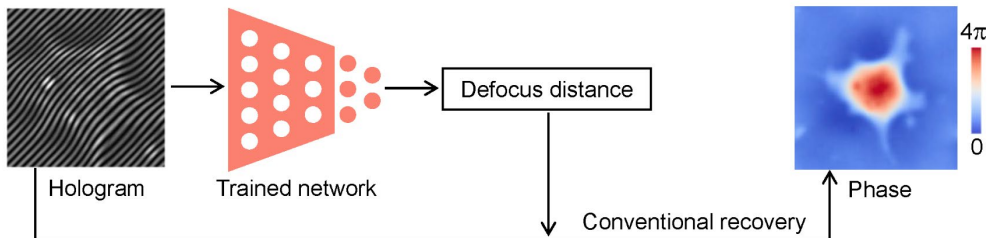


Fig. 16 Description of deep-learning-based hologram numerical refocusing.

From the perspective of classification, Pitkäaho *et al.*<sup>71</sup> first proposed to estimate the defocus distance from the hologram by a CNN. In their scheme, the zero-order and twin-image terms need to be removed before the trained neural network classifies the holograms into different discrete defocus distances. Meanwhile, Ren *et al.*<sup>72</sup> advocate directly using raw holograms collected at different defocus distances as the input of the neural networks. Furthermore, they revealed the advantages of neural networks over other machine learning algorithms in the task of autofocusing. Immediately afterward, Son *et al.*<sup>73</sup> also verified the feasibility of autofocus by classification through numerical simulations. Subsequently, Couturier *et al.*<sup>74</sup> improved the accuracy of defocus distance estimation by using a deeper CNN for categorizing defocus distance into a greater number of classes.

Nevertheless, no matter how many classes there are, the defocus distance estimated by these classification-based methods is also discrete, which is still not precise enough in practice. Thus, Ren *et al.*<sup>75</sup> further developed an approach to treat the defocus distance estimation as a regression problem, where the output of the neural network is continuous. They verified the superiority of this deep-learning-based regression method with amplitude samples and phase samples, respectively, and tested the adaptability under different exposure times and incident angles. Later, Pitkäaho *et al.*<sup>76</sup> also extended their previous classification-based work<sup>71</sup> to this regression-based approach. While these methods estimate the defocus distance of the entire hologram, Jaferzadeh *et al.*<sup>77</sup> and Moon *et al.*<sup>78</sup> proposed to take out the region of interest from the whole hologram as the input to estimate the defocus distance. In order to get rid of the constraint of known defocus distance as the label of the training dataset, Tang *et al.*<sup>79</sup> proposed to iteratively infer the defocus distance by an untrained network with a defocus hologram and its in-focus phase. Later on, Cuenat *et al.*<sup>81</sup> demonstrated the superiority of the vision Transformer (ViT) over typical CNNs in defocus distance estimation. Because the spatial spectrum information is also helpful for the defocus distance estimation<sup>94</sup>, Lee *et al.*<sup>82</sup> and Shimobaba *et al.*<sup>83</sup> proposed to use the spatial spectrum or power spectrum of holograms as the network input to estimate the defocus distance.

### 3. DL-in-processing for phase recovery

In “DL-in-processing for phase recovery”, the neural network directly performs the inference process from the measured intensity image to the phase (network-only strategy in Section 3.1), or together with the physical model or physics-based algorithm to achieve the inference (network-with-physics strategy in Section 3.2).

### 3.1 Network-only strategy

The network-only strategy uses a neural network to perform phase recovery, where the network input is the measured intensity image and the output is the phase. A summary of various methods is presented in Table 2 and described below, where we classify them into dataset-driven (DD) approaches and physics-driven (PD) approaches.

**Table 2 Summary of network-only strategy**

Task	Reference	Input	Output	Network	Training dataset	Loss function
Dataset-driven (DD) approach	Sinha <i>et al.</i> <sup>95</sup>	Diffraction image	Phase	U-Net and ResNet	Expt.: 10,000 pairs	$l_1$ -norm
	Li <i>et al.</i> <sup>96</sup>	Diffraction image	Phase	U-Net and ResNet	Expt.: 10,000 pairs	NPCC
	Deng <i>et al.</i> <sup>97</sup>	Diffraction image	Phase	U-Net and ResNet	Expt.: 10,000 pairs	NPCC
	Goy <i>et al.</i> <sup>98</sup>	Weak-light diffraction	Phase	U-Net and ResNet	Expt.: 9,500 pairs	NPCC
	Wang <i>et al.</i> <sup>99</sup>	In-line hologram	Phase	U-Net and ResNet	Expt.: 9000 and 11623 pairs	$l_2$ -norm
	Nguyen <i>et al.</i> <sup>100</sup>	Multiple LR intensity images (FP)	HR phase	U-Net and DenseNet	Expt.: ---	GAN loss and $l_1$ -norm
	Cheng <i>et al.</i> <sup>101</sup>	LR intensity image (FP)	HR phase and amplitude	CNN and ResNet	Expt.: 20 fields-of-view	$l_2$ -norm
	Cherukara <i>et al.</i> <sup>102</sup>	Far-field diffraction	Phase or amplitude (two)	SegNet	Sim.: 180,000 pairs	Cross-entropy
	Ren <i>et al.</i> <sup>103</sup>	Off-axis hologram	Phase or amplitude	ResNet and SubPixelNet	Expt.: >10,000 pairs	$l_2$ -norm
	Yin <i>et al.</i> <sup>104</sup>	Hologram	Phase	U-Net	Expt.: 2,400 and 200-2,000 (unpaired)	Cycle-GAN loss
	Lee <i>et al.</i> <sup>105</sup>	Hologram	Phase and amplitude	U-Net and CNN	Expt.: 600-9,060 (unpaired)	Cycle-GAN loss and SSIM
	Hu <i>et al.</i> <sup>106</sup>	Spots' intensity image	Phase	U-Net and ResNet	Sim.: 46,080 pairs	$l_2$ -norm
	Wang <i>et al.</i> <sup>107</sup>	Defocus intensity image	Phase	U-Net and ResNet	Expt.: 20,037 pairs	$l_2$ -norm
	Pirone <i>et al.</i> <sup>108</sup>	Hologram in different angles	Phase	CAN	Expt.: 4,000 pairs	$l_1$ -norm
	Xue <i>et al.</i> <sup>109</sup>	Bright- and dark-field images	Phase	U-Net and BNN	Expt.: 185 groups	$l_1$ -norm and uncertainty term
	Li <i>et al.</i> <sup>110</sup>	Two images of symmetric illumination	Phase	U-Net	Sim.: 1,301 groups	GAN loss
	Wang <i>et al.</i> <sup>92,111</sup>	Hologram	Phase and amplitude	Y-Net	Expt.: 1,331 pairs	$l_2$ -norm
	Zeng <i>et al.</i> <sup>112</sup>	Hologram	Phase or amplitude	CapsNet	Expt.: ---	$l_2$ -norm
	Wu <i>et al.</i> <sup>113</sup>	Far-field diffraction	Phase and amplitude	Y-Net	Sim.: 142,500 groups	Loss in real and reciprocal space
	Huang <i>et al.</i> <sup>114</sup>	Two or 3 holograms	Complex field	U-Net and Recurrent CNN	Expt.: 208 groups	GAN loss and $l_1$ -norm and SSIM
	Uelwer <i>et al.</i> <sup>115</sup>	Far-field diffraction	Phase	Cascaded neural network	Sim.: ---	$l_2$ -norm or $l_1$ -norm
	Castaneda <i>et al.</i> <sup>116</sup>	Off-axis hologram	Wrapped phase	U-Net	Expt.: 1,512 pairs	GAN loss and TSM and STD
	Jaferzadeh <i>et al.</i> <sup>117</sup>	Off-axis hologram	Phase	U-Net	Expt.: 900 pairs	GAN loss
	Luo <i>et al.</i> <sup>118</sup>	Hologram	Phase	MCN	Expt.: 1 pair	Bucket error rate (BER) loss
	Ding <i>et al.</i> <sup>119</sup>	LR image	HR phase	U-Net and ViT	Expt.: 3,500 and 3,500 (unpaired)	Cycle-GAN loss
	Ye <i>et al.</i> <sup>120</sup>	Far-field diffraction	Complex field	MLP and CNN	Sim. and Expt.: ---	$l_1$ -norm
	Chen <i>et al.</i> <sup>121,122</sup>	Three or 4 holograms	Complex field	ResNet and Fourier module (FIN)	Expt.: 600 groups	$l_1$ -norm, complex domain and perceptual loss

	Shu <i>et al.</i> <sup>123</sup>	Hologram	Phase	Network based on NAS	Expt.: 276 pairs	MixGE and binary and sparsity loss
Physics-driven (PD) approach	Boominathan <i>et al.</i> <sup>124</sup>	LR intensity images (FP)	HR Phase and amplitude	U-Net	Sim.: 1 (input only)	$l_2$ -norm with physical model
	Wang <i>et al.</i> <sup>125</sup>	Diffraction image	Phase	U-Net	Sim. and Expt.: 1 (input only)	$l_2$ -norm with physical model
	Zhang <i>et al.</i> <sup>126</sup>	Diffraction image	Phase	U-Net	Sim. and Expt.: 1 (input only)	$l_2$ -norm with defocus distance and physical model
	Yang <i>et al.</i> <sup>127,128</sup>	Diffraction image	Phase and amplitude	U-Net	Sim. and Expt.: 1-180 (input only)	$l_2$ -norm with aperture constraint
	Bai <i>et al.</i> <sup>129</sup>	Hologram	dual-wavelength Phase	CDD	Expt.: 1 (input only)	$l_2$ -norm with physical model
	Galande <i>et al.</i> <sup>130</sup>	Hologram	Phase and amplitude	U-Net	Expt.: 1 (input only)	$l_2$ -norm with physical model and denoiser
	Yao <i>et al.</i> <sup>131</sup>	3D diffraction image	Phase and amplitude	3D Y-Net	Sim.: 52,000 (input only)	$l_2$ -norm with physical model
	Li <i>et al.</i> <sup>132</sup>	Two diffraction images	Phase	Two-to-one Y-Net	Sim.: 500 (input only)	$l_2$ -norm with physical model
	Bouchama <i>et al.</i> <sup>133</sup>	LR intensity images (FP)	HR Phase and amplitude	U-Net	Sim.: 10,000 (input only)	$l_2$ -norm with physical model
	Huang <i>et al.</i> <sup>134</sup>	Two holograms	Phase and amplitude	---	Sim.: 100,000 (input only)	$l_2$ -norm and Fourier domain $l_1$ -norm

**Dataset-driven approach.** As one of the most commonly adopted strategies, data-driven deep learning phase recovery methods presuppose a large number of paired input-label datasets. Usually, it is necessary to experimentally collect a significant number of intensity images (such as diffraction images or holograms, etc.) as input, and use conventional methods to calculate the corresponding phase as ground-truth (Fig. 17a). The key lies in that this paired dataset implicitly contains the mapping relationship from intensity to phase. Then, an untrained/initialized neural network is iteratively trained with the paired dataset as an *implicit prior*, where the gradient of the loss function propagates into the neural network to update the parameters (Fig. 17b). After training, the network is used as an end-to-end mapping to infer the phase from intensity (Fig. 17c). Therefore, the DD approach is to guide/drive the training of the neural network with this implicit mapping, which is internalized into the neural network as the parameters are iteratively updated.

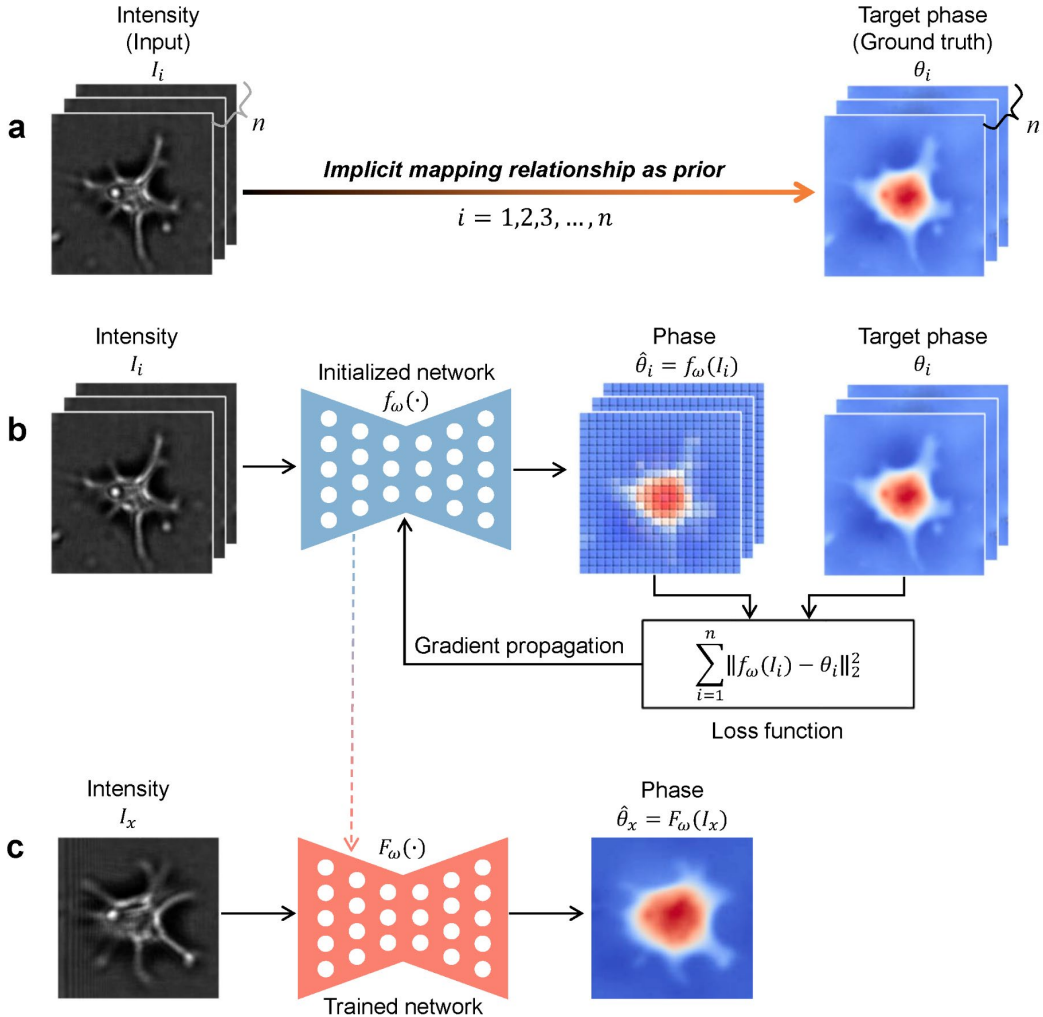


**Fig. 17 Description of dataset-driven approach for phase recovery.** **a** Dataset collection. **b** Network training. **c** Inference via a trained network.

Sinha *et al.*<sup>95</sup> were among the first to demonstrate this end-to-end deep learning strategy for phase recovery, in which the phase of objects is inferred from corresponding diffraction images via a trained deep neural network. In dataset collection, they used a phase-only spatial light modulator (SLM) to load different public image datasets to generate the phase as ground-truth, and after a certain distance, place the image sensor to record the diffraction image as input. The advantage is that both the diffraction image and the phase are known, and is easily collected in large quantities. Through comparative tests, they verified the adaptability of the deep neural network to unseen types of datasets and different defocus distances. Although this scheme cannot be used in practical application due to the use of the phase-type spatial light modulator, their pioneering work opens the door to deep-learning-inference phase recovery. For instance, Li *et al.*<sup>96</sup> introduced the negative Pearson correlation coefficient (NPCC)<sup>135</sup> as a loss function to train the neural network, and enhanced the spatial

resolution by a factor of two by flattening the power spectral density of the training dataset. Deng *et al.*<sup>97</sup> found that the higher the Shannon entropy of the training dataset, the stronger the generalization ability of the trained neural network. Goy *et al.*<sup>98</sup> extended the work to phase recovery under weak-light illumination.

Meanwhile, Wang *et al.*<sup>99</sup> extended the diffraction device of Sinha *et al.*<sup>95</sup> to an in-line holographic device by adding a coaxial reference beam, and used the in-line hologram instead of the diffraction image as the input to a neural network for phase recovery. Nguyen *et al.*<sup>100</sup> applied this end-to-end strategy for FP, inferring the high-resolution phase from a series of low-resolution intensity images via a U-Net, and Cheng *et al.*<sup>101</sup> further used a single low-resolution intensity image under optimized illumination as the neural network input. Cherukara *et al.*<sup>102</sup> extended this end-to-end deep learning strategy to CDI, in which they trained two neural networks with simulation datasets to infer the amplitude or phase of objects from far-field diffraction intensity maps, respectively. Ren *et al.*<sup>103</sup> demonstrated the time and accuracy superiority of this end-to-end deep learning strategy over conventional numerical algorithms in the case of off-axis holography. Yin *et al.*<sup>104</sup> introduced the cycle-GAN to extend this end-to-end deep learning strategy to the application scenario of unpaired datasets. Lee *et al.*<sup>105</sup> replaced the forward generator of the cycle-GAN by numerical propagation, improving the phase recovery robustness of neural networks in highly perturbative configurations. Hu *et al.*<sup>106</sup> applied this end-to-end deep learning strategy to the Shack-Hartmann wavefront sensor, inferring the phase directly from a spot intensity image after the micro-lens array. Wang *et al.*<sup>107</sup> extended this end-to-end deep learning strategy to TIE, using a trained neural network to infer the phase of the cell object from a defocus intensity image illuminated by partially coherent light. Pirone *et al.*<sup>108</sup> applied this hologram-to-phase deep learning strategy to improve the reconstruction speed of 3D optical diffraction tomography (ODT) from tens of minutes to a few seconds. Tayal *et al.*<sup>136</sup> demonstrated the use of data augmentation and a symmetric invariant loss function to break the symmetry in the end-to-end deep learning phase recovery.

In addition to expanding the application scenarios of this end-to-end deep learning strategy, some researchers focused on the performance and advantages of different neural networks in phase recovery. Xue *et al.*<sup>109</sup> applied Bayesian neural network (BNN) into FP for inferring model uncertainty while doing phase recovery. Li *et al.*<sup>110</sup> applied GAN for phase recovery, inferring the phase from two symmetric-illumination intensity images. Wang *et al.*<sup>92,111</sup> proposed a one-to-multi CNN, Y-Net<sup>92</sup>, from which the amplitude and phase of an object can be inferred from the input intensity simultaneously. Zeng *et al.*<sup>112</sup> introduce the

capsule network to overcome information loss in the pooling operation and internal data representation of CNN. Compared with conventional CNN, their proposed capsule-based CNN (RedCap) saves 75% of network parameters while ensuring higher holographic reconstruction accuracy. Wu *et al.*<sup>113</sup> applied the Y-Net<sup>92</sup> to CDI for simultaneous inference of phase and amplitude. Huang *et al.*<sup>114</sup> introduced a recurrent convolution module into U-Net, trained using GAN, for holographic reconstruction with autofocus. Uelwer *et al.*<sup>115</sup> used a cascaded neural network for end-to-end phase recovery. Castaneda *et al.*<sup>116</sup> and Jaferzadeh *et al.*<sup>117</sup> introduced GAN into off-axis holographic reconstruction. Luo *et al.*<sup>118</sup> added dilated convolutions into a CNN, termed mixed-context network (MCN)<sup>118</sup>, for phase recovery. By comparing in a one-sample-learning scheme, they found that MCN is more accurate and compact than the conventional U-Net. Ding *et al.*<sup>119</sup> added ViT into U-Net and trained it with low-resolution intensity as input and high-resolution phase as ground-truth using cycle-GAN. The trained neural network can do phase recovery while enhancing the resolution, and has higher accuracy than the conventional U-Net. In CDI, Ye *et al.*<sup>120</sup> used a multi-layer perceptron for feature extraction before a CNN, considering the property of the far-field (Fourier) intensity images where the data are globally correlated. Chen *et al.*<sup>121,122</sup> combined the spatial Fourier transform module with ResNet, termed Fourier imager network (FIN), to achieve holographic reconstruction with superior generalization to new types of samples and faster inference speed (9-fold faster than their previous recurrent neural network, 27-fold faster than conventional iterative algorithms). Shu *et al.*<sup>123</sup> applied neural architecture search (NAS) to automatically optimize the network architecture for phase recovery. Compared with the conventional U-Net, the peak signal-to-noise ratio (PSNR) of their NAS-based network is increased from 34.7 dB to 36.1 dB, and the inference speed is increased by 27-fold.

As a similar deep learning phase recovery strategy in adaptive optics, researchers demonstrated that neural networks could be used to infer the phase of the turbulence-induced aberration wavefront or its Zernike coefficient from the distortion intensity of target objects<sup>137</sup>. In these applications, only the wavefront that is subsequently used for aberration correction is of interest, not the RI distribution of turbulence itself that produces this aberration wavefront.

**Physics-driven approach.** Different from the dataset-driven approach that uses input-label paired dataset as an implicit prior for neural network training, physical models, such as numerical propagation, can be used as an *explicit prior* to guide/drive the inference or training of neural networks, termed physics-driven (PD) approach. On the one hand, this explicit prior can be used to iteratively optimize an untrained neural network to infer the

corresponding phase and amplitude from the measured intensity image as input, referred to as the untrained PD (uPD) scheme (Fig. 18a). On the other hand, this explicit prior can be used to train an untrained neural network with a large number of intensity images as input, which then can infer the corresponding phase from unseen intensity images, an approach called the trained PD (tPD) scheme (Fig. 18b).

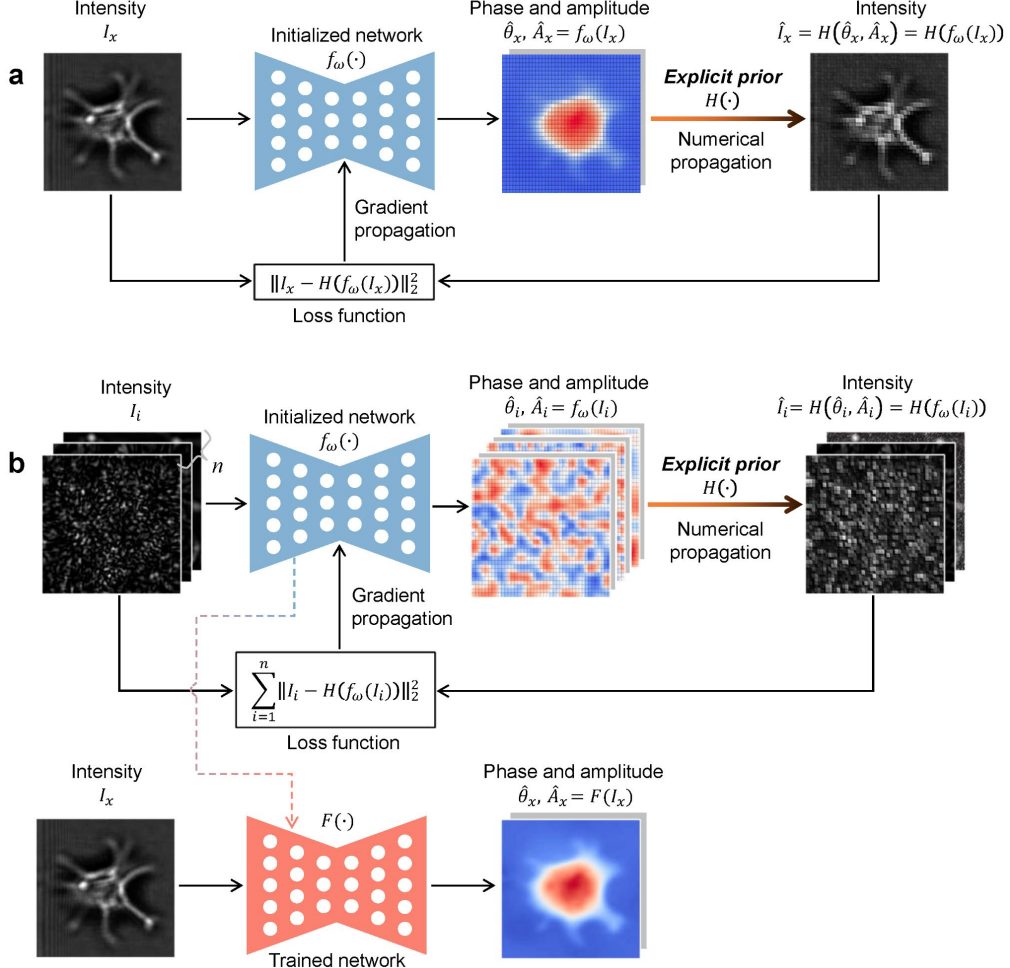


**Fig. 18 Description of physics-driven approach for phase recovery.** **a** Untrained PD (uPD) scheme. **b** Trained PD (tPD) scheme.

In order to more intuitively understand the difference and connection between the DD and PD approaches, let us compare the loss functions in Fig. 17 and Fig. 18:

$$Loss_{DD} = \sum_{i=1}^n \|f_\omega(I_i) - \theta_i\|_2^2, \quad (1)$$

$$Loss_{uPD} = \|I_x - H(f_\omega(I_x))\|_2^2, \quad (2)$$

$$Loss_{tPD} = \sum_{i=1}^n \|I_i - H(f_\omega(I_i))\|_2^2, \quad (3)$$

where  $\|\cdot\|_2^2$  denotes the square of the  $l_2$ -norm (or other distance functions),  $f_\omega(\cdot)$  is a neural network with trainable parameters  $\omega$ ,  $H(\cdot)$  is a physical model (such as numerical propagation, Fourier transform, or FP measurement model),  $I_i$  is the measured intensity image in the training dataset,  $\theta_i$  is the phase in the training dataset,  $I_x$  is the measured intensity image of a test sample, and  $n$  is the number of samples in the training dataset. In Eq. (1) for the DD approach, the priors used for network training are the measured intensity image and corresponding ground-truth phase. Meanwhile, in Eqs. (2) and (3) for the PD approaches, the priors used for network inference or training are the measured intensity image and physical model, instead of the phase.

This PD approach was first implemented in the work on Fourier Ptychography by Boominathan *et al.*<sup>124</sup>. They proposed it in the higher overlap case, including the scheme of directly using an untrained neural network for inference (uPD) and the scheme of training first and then inferring (tPD), and demonstrated the former by simulation.

For the uPD scheme, Wang *et al.*<sup>125</sup> used a U-Net-based scheme to iteratively infer the phase of an object from a measured diffraction image whose de-focus distance is known. Their method demonstrates higher accuracy than conventional algorithms (such as GS and TIE) and the DD scheme, at the expense of a longer inference time (about 10 minutes for an input with  $256 \times 256$  pixels). Zhang *et al.*<sup>126</sup> extended this work to the case where the defocus distance is unknown, by including it as another unknown parameter together with the phase to the loss function. Yang *et al.*<sup>127,128</sup> further generalized this to the complex field inference by introducing an aperture constraint into the loss function, and pointed out that it would cost as much as 600 hours to infer 3,600 diffraction images with this uPD scheme. Meanwhile, Bai *et al.*<sup>129</sup> extended this from a single-wavelength case to a dual-wavelength case. Galande *et al.*<sup>130</sup> found that this way of neural network optimization with a single-measurement intensity input lacks information diversity and can easily lead to overfitting of the noise, which can be mitigated by introducing an explicit denoiser. This way of using the object-related intensity image as the neural network input makes it possible to internalize the mapping relationship between intensity and phase into the neural network through pre-training. It is worth mentioning that some researchers proposed to make adjustments to the uPD scheme, using the initial phase and amplitude recovered by backward numerical propagation as the neural network input<sup>138–140</sup>, which reduces the burden on the neural network to obtain higher inference accuracy.

Although the phase can be inferred from the measured intensity image through an untrained neural network without any ground-truth, the uPD scheme inevitably requires a large number of iterations, which excludes its use in many dynamic applications. Therefore, to adapt the PD scheme to dynamic inference, Yang *et al.*<sup>127,128</sup> adjusted their previously proposed uPD scheme to the tPD scheme by pre-training the neural network using a small part of the measured diffraction images, and then using the pre-trained neural network to infer the remaining ones. Yao *et al.*<sup>131</sup> trained a 3D version of the Y-Net<sup>92</sup> with simulated diffraction images as input, and then used the pre-trained neural network for direct inference or iterative refinement, which is 100 and 10 times faster than conventional iterative algorithms, respectively. Li *et al.*<sup>132</sup> proposed a two-to-one neural network to reconstruct the complex field from two axially displaced diffraction images. They used 500 simulated diffraction images to pre-train the neural network, and then inferred an unseen diffraction image by refining the pre-trained neural network for 100 iterations. Bouchama *et al.*<sup>133</sup> further extended the tPD scheme to Fourier Ptychography of low overlap cases by simulated datasets. Different from the above ways of generating training datasets from natural images or real experiments, Huang *et al.*<sup>134</sup> proposed to generate training datasets from randomly synthesized artificial images with no connection or resemblance to real-world samples. They further trained a neural network with this generated dataset and a physics-consistency loss, which showed superior external generalization to holograms of real tissues with arbitrarily defocus distances.

### 3.2 Network-with-physics strategy

Different from the network-only strategy, in the network-with-physics strategy, either the physical model and neural network are connected in series for phase recovery (physics-connect-network, PcN), or the neural network is integrated into a physics-based algorithm for phase recovery (network-in-physics, NiP), or the physical model or physics-based algorithm is integrated into a neural network for phase recovery (physics-in-network, PiN). A summary of the network-with-physics strategy is presented in Table 3 and is described below.

**Table 3 Summary of network-with-physics strategy**

Task	Reference	Input	Output	Network	Training dataset	Loss function
(PcN) network connect-	Rivenson <i>et al.</i> <sup>141</sup>	Initial complex field	Pure complex field	CNN and ResNet	Expt.: 100 pairs	$l_2$ -norm
	Wu <i>et al.</i> <sup>142</sup>	Initial complex field	Pure complex field (in-focus)	U-Net and ResNet	Expt.: 704 pairs	$l_1$ -norm
	Huang <i>et al.</i> <sup>114</sup>	Initial complex field	Pure complex field	U-Net and Recurrent CNN	Expt.: 208 groups	GAN loss and $l_1$ -norm and SSIM

	Goy <i>et al.</i> <sup>98</sup>	Initial phase	Pure phase	U-Net and ResNet	Expt.: 9,500 pairs	NPCC
	Deng <i>et al.</i> <sup>143</sup>	Initial phase	Pure phase	U-Net and ResNet	Expt.: 9,500 pairs	$l_2$ -norm and features of VGG
	Deng <i>et al.</i> <sup>144</sup>	(i) Initial phase, (ii) LR and HR phase	(i) LR or HR phase, (ii) Phase (three)	U-Net and ResNet	Expt.: 9,500 pairs	NPCC
	Kang <i>et al.</i> <sup>145</sup>	Initial phase	Pure phase	U-Net and ResNet	Expt.: 5,000 pairs	NPCC or SSIM
	Zhang <i>et al.</i> <sup>146</sup>	Synthetic initial phase and amplitude	HR phase and amplitude	CNN and ResNet	Sim.: 23,040 groups	$l_1$ -norm
	Moon <i>et al.</i> <sup>147</sup>	initial superimposed phase	Pure phase	U-Net	Expt.: 1,500 pairs	GAN loss
Network-in-physics (NiP)	Metzler <i>et al.</i> <sup>148</sup>	Noisy phase	Denoised phase	DnCNN	Sim.: 300,000 pairs	---
	Wu <i>et al.</i> <sup>149</sup>	Noisy phase	Denoised phase	DnCNN	Sim.: ---	---
	Bai <i>et al.</i> <sup>150</sup>	Noisy phase	Denoised phase	DnCNN	Sim.: 300,000 pairs	---
	Wang <i>et al.</i> <sup>151</sup>	Noisy phase	Denoised phase	DnCNN	Sim.: ---	$l_2$ -norm
	Chang <i>et al.</i> <sup>152</sup>	Noisy phase and amplitude	Denoised phase and amplitude	FFDNet	Sim.: 10,000 pairs	---
	İşil <i>et al.</i> <sup>153</sup>	Noisy phase	Denoised phase	U-Net	Sim.: 3,000 pairs	$l_2$ -norm
	Kumar <i>et al.</i> <sup>154</sup>	Noisy phase	Denoised phase	U-Net and ResNet	---	---
	Jagatap <i>et al.</i> <sup>155,156</sup>	Fixed random vector	Phase	Decoder	Sim.: 1	$l_2$ -norm
	Zhou <i>et al.</i> <sup>157</sup>	Fixed random matrix	Phase	SegNet	Sim. and Expt.: 1	$l_2$ -norm
	Shamshad <i>et al.</i> <sup>158</sup>	Fixed random matrix	Phase	U-Net	Sim.: 1	$l_2$ -norm
	Boston <i>et al.</i> <sup>159</sup>	Fixed random vector and Zernike polynomials	Phase and aberrations	Decoder or fully connected network	Expt.: 1	$l_2$ -norm
	Lawrence <i>et al.</i> <sup>160</sup>	Fixed random vector	Phase	Decoder	Sim.: 1	Poisson likelihood
	Niknam <i>et al.</i> <sup>161</sup>	Fixed random vector	Phase and amplitude	Decoder	Expt.: 1	$l_2$ -norm
	Ma <i>et al.</i> <sup>162</sup>	Fixed random vector	Phase	Decoder	Sim.: 1	$l_2$ -norm
	Chen <i>et al.</i> <sup>163</sup>	Fixed random vector	Phase, amplitude, pupil aberration and illumination fluctuation factor	Decoders or fully connected networks	Sim.: 1	$l_2$ -norm
	Hand <i>et al.</i> <sup>164</sup>	Phase or random vector	Phase	VAE or DCGAN	Sim.: 60,000 and 200,000 pairs	$l_2$ -norm
	Shamshad <i>et al.</i> <sup>165–167</sup>	Random vector	Phase	DCGAN	Sim.: 60,000 pairs 73,257 pairs	$l_2$ -norm
	Hyder <i>et al.</i> <sup>168</sup>	Random vector	Phase	DCGAN	Sim.: 202,599 pairs	$l_2$ -norm
	Uelwer <i>et al.</i> <sup>169</sup>	Random vector	Phase	VAE, DCGAN or Style-GAN	Sim.: ---	$l_2$ -norm, LPIPS and Wasserstein adversarial loss
Physics-in-network (PiN)	Wang <i>et al.</i> <sup>170</sup>	Intensity	Phase	deGEC-SR-Net	Sim.: 100 pairs	$l_2$ -norm
	Naimipour <i>et al.</i> <sup>171,172</sup>	Intensity	Phase	Auto-encoder network	Sim.: 2,048 pairs	$l_2$ -norm
	Zhang <i>et al.</i> <sup>173</sup>	Intensity	Phase and amplitude	Complex U-Net (untrained)	Sim.: 1	$l_2$ -norm
	Shi <i>et al.</i> <sup>174</sup>	Intensity	Phase	Deep shrinkage network (DSN)	Sim.: 204,800 pairs	$l_2$ -norm
	Wu <i>et al.</i> <sup>175</sup>	Intensity	Phase	Cascaded CNN	Sim. and Expt.: 400 and 140 pairs	$l_2$ -norm
	Yang <i>et al.</i> <sup>176</sup>	Intensity	Phase	CNN in space and frequency domain	Sim.: 400 and 60,000 pairs	$l_2$ -norm and edge loss

**Physics-connect-network (PcN).** In this scheme, the role of the neural network is to extract and separate the pure phase from the initial estimate that may suffer from spatial artifacts or low resolution, which allows the neural network to perform a simpler task than the

network-only strategy; typically, the initial phase is calculated using a physical model (Fig. 19).

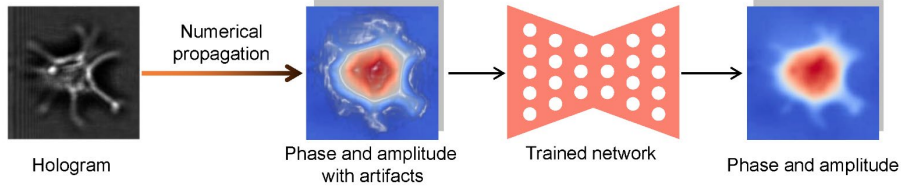


Fig. 19 Description of physics-connect-network (PcN).

Rivenson *et al.*<sup>141</sup> first applied this PcN scheme in holographic reconstruction in 2018. They used numerical propagation to calculate the initial complex field (including real and imaginary parts) from a single intensity-only hologram, which contained twin-image and self-interference-related spatial artifacts, then used a data-driven trained neural network to extract the pure complex field from the initial estimate. Compared with the axial multi-intensity alternating projection algorithm<sup>33–35</sup>, their PcN scheme reduces the number of required holograms by 2-3 times while improving the computation time by more than three times. Wu *et al.*<sup>142</sup> then extended the depth of field (DOF) based on this work, by training a neural network with pairs of randomly de-focused complex fields and the corresponding in-focus complex field. Meanwhile, Huang *et al.*<sup>114</sup> proposed to use a recurrent CNN<sup>177</sup> for the PcN scheme and the network-only strategy. They compared the performance of the neural networks with the hologram or initial complex field as input in the same background, and found that the network-only strategy is more robust to sparse samples while the PcN scheme performs better inference on dense samples. Goy *et al.*<sup>98</sup> applied the PcN scheme to phase recovery under weak-light illumination, which is more ill-posed than conventional phase recovery. They showed that the inference performance of the PcN scheme is stronger than that of the network-only strategy under weak-light illumination, especially for dense samples in the extreme photon level case (1 photon). Further, Deng *et al.*<sup>143</sup> introduced a default feature perceptual loss of the VGG layer into the loss function for neural network training, which inferred more fine details than that of the NPCC loss function. They also improved the spatial resolution and noise robustness by learning the low-frequency and high-frequency bands, respectively, through two neural networks and synthesizing these two bands into full-band reconstructions with a third neural network<sup>144</sup>. By introducing random phase modulation, Kang *et al.*<sup>145</sup> further improved the phase recovery ability of the PcN scheme under weak-light illumination. Zhang *et al.*<sup>146</sup> extended the PcN scheme to FP, inferring high-resolution phase and amplitude using the initial phase and amplitude synthesized from the intensity

images as input to a neural network. Moon *et al.*<sup>147</sup> extended the PCN scheme to off-axis holography, using numerical propagation to obtain the initial phase from the Gaber hologram as the input to the neural network.

**Network-in-physics (NiP).** Regarding phase recovery as one of the most general optimization problems, this approach can be expressed as

$$\arg \min_{\theta} \|I_x - H(\theta)\|_2^2 + R(\theta), \quad (4)$$

where  $H(\cdot)$  is the physical model (such as numerical propagation, Fourier transform, or FP measurement model),  $\theta$  is the phase,  $I_x$  is the measured intensity image of a test sample, and  $R(\theta)$  is a regularized constraint. According to the Regularization-by-Denoising (RED)<sup>178</sup> framework, a pre-trained neural network for denoising can be used as the regularized constraint:

$$\arg \min_{\theta} \|I_x - H(\theta)\|_2^2 + R(\theta), \quad \text{with } R(\theta) = \lambda \theta^T (\theta - D(\theta)), \quad (5)$$

where  $D(\theta)$  is a pre-trained neural network for denoising, and  $\lambda$  is a weight factor to control the strength of regularization. Metzler *et al.*<sup>148</sup> used the above algorithm for phase recovery and called it PrDeep. They used a DnCNN trained on 300,000 pairs of data as a denoiser and FASTA<sup>179</sup> as a solver. In comparison with other conventional iterative methods, PrDeep demonstrates excellent robustness to noise. Wu *et al.*<sup>149</sup> proposed an online extension of PrDeep, which adopts the online processing of data by using only a random subset of measurements at a time. Bai *et al.*<sup>150</sup> extended PrDeep to incorporate a contrast-transfer-function-based forward operator in  $H(\cdot)$  for phase recovery. Wang *et al.*<sup>151</sup> improved PrDeep by changing the solver from FASTA to ADMM, which further improved the noise robustness. Chang *et al.*<sup>152</sup> used a generalized-alternating-projection solver to further expand the performance of PrDeep and made it suitable for the recovery of complex fields. İşil *et al.*<sup>153</sup> embedded a trained neural network denoiser into HIO, removing artifacts from the results after each iteration. On this basis, Kumar *et al.*<sup>154</sup> added total-variation prior together with the denoiser for regularization.

In addition, according to the deep image prior (DIP)<sup>180,181</sup>, even an untrained neural network itself can be used as a structural prior for regularization (Fig. 20):

$$\arg \min_{\omega} \left\| I_x - H(g_{\omega}(z_f)) \right\|_2^2, \quad (6)$$

where  $g_\omega(\cdot)$  is an untrained neural network with trainable parameters  $\omega$  that usually takes a generative decoder architecture,  $I_x$  is the measured intensity image of a test sample, and  $z_f$  is a fixed random vector as latent code.

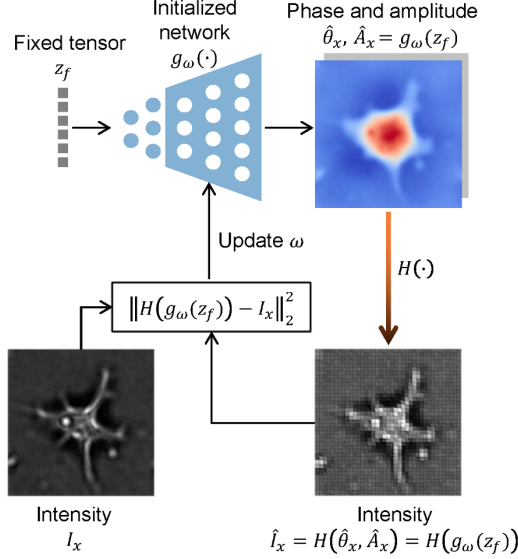


Fig. 20 Description of DIP-based phase recovery.

This DIP-based approach was first introduced to phase recovery by Jagatap *et al.*<sup>155</sup>. They solved Eq. (6) using the gradient descent and projected gradient descent algorithms by optimizing over trainable parameters  $\omega$ , both of which outperform sparse truncated amplitude flow (SPARTA) algorithm. In follow-up work, they provided rigorous theoretical guarantees for the convergence of their algorithm<sup>156</sup>. Zhou *et al.*<sup>157</sup> applied this DIP-based algorithm to ODT, alleviating the effects of the missing cone problem. Shamshad *et al.*<sup>158</sup> extended this DIP-based algorithm to subsampled FP, achieving better reconstructions at low subsampling ratios and high noise perturbations. In order to make the algorithm adaptive to different aberrations, Bostan *et al.*<sup>159</sup> added a fully connected neural network with Zernike polynomials as the fixed input, and used it as the second structural prior. In the holographic setting with a reference beam, Lawrence *et al.*<sup>160</sup> demonstrated the powerful information reconstruction ability of the DIP-based algorithm in extreme cases such as low photon counts, beamstop-obscured frequencies, and small oversampling. Niknam *et al.*<sup>161</sup> used the DIP-based algorithm to recover complex fields from an in-line hologram. They further improved the twin-image artifacts suppression capability through some additional regularization, such as bounded activation function, weight decay, and parameter perturbation. Ma *et al.*<sup>162</sup> embed an untrained generation network into the ADMM algorithm to solve the phase recovery at low subsampling ratios, and achieved better results than the gradient descent and projected

gradient descent algorithms of Jagatap *et al.*<sup>155</sup>. Chen *et al.*<sup>163</sup> extended the DIP-based algorithm to FP, in which four parallel untrained neural networks were used for generating phase, amplitude, pupil aberration, and illumination fluctuation factor correction, respectively.

Similarly, a pre-trained generative neural network can also be used as a generative prior, assuming that the target phase is in the range of the output of this trained neural network (Fig. 21):

$$\arg \min_z \|I_x - H(G(z))\|_2^2, \quad (7)$$

where  $G(\cdot)$  is a pre-trained fixed neural network that usually takes a generative decoder architecture,  $I_x$  is the measured intensity image of a test sample, and  $z$  is a latent code tensor to be searched. Due to the use of the generative neural network, the multi-dimensional phase that originally needed to be iteratively searched is converted into a low-dimensional tensor, and the solution space is also limited within the range of the trained generative neural network.

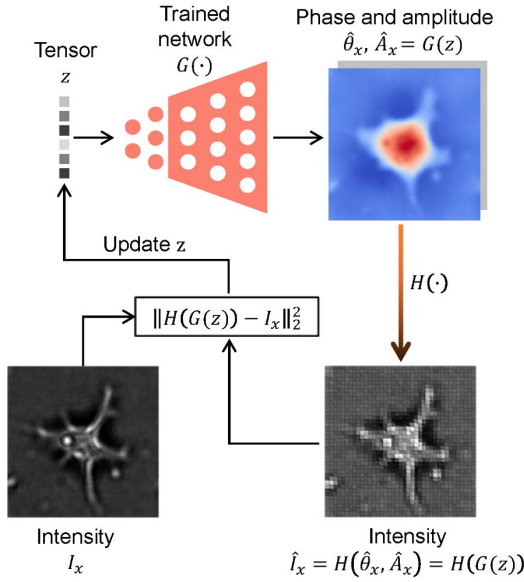


Fig. 21 Description of generative-prior-based phase recovery.

Hand *et al.*<sup>164</sup> used generative prior for phase recovery with rigorous theoretical guarantees for random Gaussian measurement matrix, showing better performance than SPARTA at low subsampling ratios. Later on, Shamshad *et al.*<sup>165</sup> experimentally verified the robustness of the generative-prior-based algorithm to low subsampling ratios and strong noise in the coded diffraction setup. Then, Shamshad *et al.*<sup>166</sup> extended this generative-prior-based algorithm to subsampled FP. Hyder *et al.*<sup>168</sup> improved over this by combining the gradient descent and projected gradient descent methods with AltMin-based non-convex optimization

methods. As a general defect, the trained generative neural network will limit the solution space to a specific range related to the training dataset, so that the iterative algorithm cannot search beyond this range. Therefore, Shamshad *et al.*<sup>167</sup> set both the input and previously fixed parameters of the trained generative neural network to be trainable. As another solution, Uelwer *et al.*<sup>169</sup> extended the range of the trained generative neural network by intermediate layer optimization.

**Physics-in-network (PiN).** According to the algorithm unrolling/unfolding technique proposed by Gregor and LeCun<sup>182</sup>, physics-based iterative algorithms can be unrolled as an interpretable neural network architecture (Fig. 22). Wang *et al.*<sup>170</sup> unrolled an algorithm called decentralized generalized expectation consistent signal recovery (deGEC-SR) into a neural network with trainable parameters, which exhibits stronger robustness using fewer iterations than the original deGEC-SR. Naimipour *et al.*<sup>171,172</sup> used the algorithm unrolling technique in reshaped Wirtinger flow and SPARTA. Zhang *et al.*<sup>173</sup> unrolled the iterative process of the alternative projection algorithm into complex U-Nets. Shi *et al.*<sup>174</sup> used a deep shrinkage network and dual frames to unroll the proximal gradient algorithm in coded diffraction imaging. Wu *et al.*<sup>175</sup> integrated the Fresnel forward operator and TIE inverse model into a neural network, which can be efficiently trained with a small number of datasets and is suitable for transfer learning. Yang *et al.*<sup>176</sup> unrolled the classic HIO algorithm into a neural network that combines information both in the spatial domain and frequency domain.

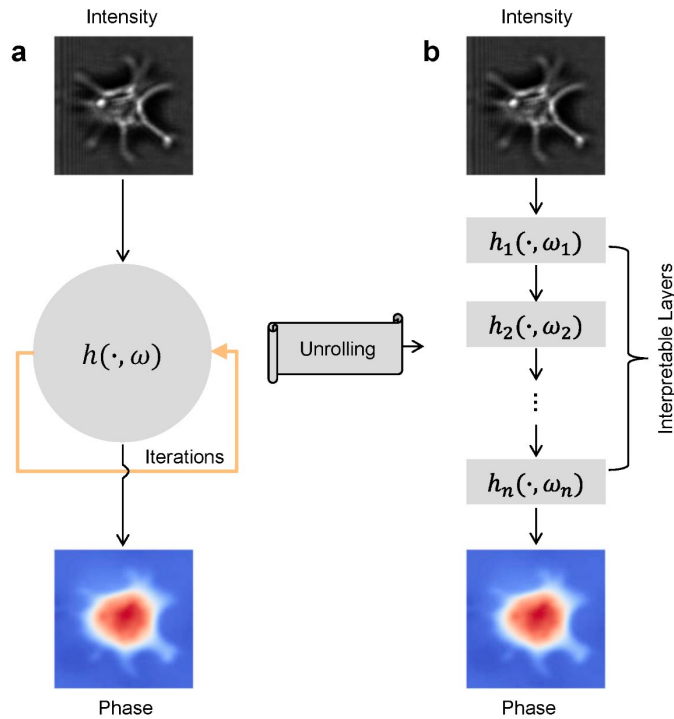


Fig. 22 Description of physics-in-network (PiN). **a** A physics-based iterative algorithm. **b** A corresponding unrolled neural network. The iteration step  $h$  with algorithm parameters  $\omega$  in (a) is unrolled and transferred to the network layers  $h_1, h_2, \dots, h_n$  with network parameters  $\omega_1, \omega_2, \dots, \omega_n$  in (b). The unrolled neural network is trained with the dataset in an end-to-end manner.

## 4. DL-post-processing for phase recovery

A summary of “DL-post-processing for phase recovery” is presented in Table 4 and is described below, including noise reduction (Section 4.1), resolution enhancement (Section 4.2), aberration correction (Section 4.3), and phase unwrapping (Section 4.4).

**Table 4 Summary of “DL-post-preprocessing for phase recovery”**

Task	Reference	Input	Output	Network	Training dataset	Loss function
Noise reduction	Jeon <i>et al.</i> <sup>183</sup>	Noisy hologram	Noise-free hologram	U-Net	Sim.: 384,000 pairs	$l_2$ -norm and Edge
	Choi <i>et al.</i> <sup>184</sup>	Noisy tomogram	Noise-free tomogram	U-Net	Expt.: 455 and 5,057 (unpaired)	Cycle-GAN loss
	Zhang <i>et al.</i> <sup>185</sup>	Noisy wrapped phase	Noise-free wrapped phase	CNN	Sim.: 500 pairs	---
	Yan <i>et al.</i> <sup>186,187</sup>	Noisy sine and cosine	Noise-free sine and cosine	ResNet	Sim.: 40,000 and 30,000 pairs	$l_2$ -norm
	Montresor <i>et al.</i> <sup>188</sup>	Noisy sine and cosine	Noise-free sine and cosine	DnCNN	Sim.: 40 pairs (15,360 patches)	$l_2$ -norm
	Tahon <i>et al.</i> <sup>189,190</sup>	Noisy sine and cosine	Noise-free sine and cosine	DnCNN	Sim.: 25 pairs and 128 pairs	$l_2$ -norm
	Fang <i>et al.</i> <sup>191</sup>	Noisy real, imaginary	Noise-free real, imaginary	U-Net	Sim.: 4,000 pairs	GAN loss
	Murdaca <i>et al.</i> <sup>192</sup>	Noisy real, imaginary, and amplitude	Noise-free real, imaginary, and amplitude	U-Net	Sim.: 5,400 pairs	$l_2$ -norm
Resolution enhancement	Tang <i>et al.</i> <sup>193</sup>	Fixed noise matrix	Noise-free phase	U-Net (untrained)	Expt.: 1	$l_2$ -norm, gradient, and variance
	Liu <i>et al.</i> <sup>194,195</sup>	LR phase and amplitude	HR phase and amplitude	U-Net	Expt.: >50,000 pairs	GAN loss
	Jiao <i>et al.</i> <sup>196</sup>	LR phase from DPM	HR phase from SLIM	U-Net	Expt.: >1,200 pairs (>100 cells)	$l_2$ -norm
	Butola <i>et al.</i> <sup>197</sup>	LR phase	HR phase	U-Net	Expt.: 2,355 pairs and 2,279 pairs	GAN loss
	Meng <i>et al.</i> <sup>198</sup>	LR phase from SI-DHM	HR phase from SI-DHM	U-Net	Expt.: 3,800 pairs	$l_2$ -norm
	Li <i>et al.</i> <sup>199</sup>	LR phase from qDPC	HR phase from qDPC	U-Net	Expt.: 1,680 pairs	$l_2$ -norm
	Gupta <i>et al.</i> <sup>200</sup>	LR phase	HR phase	U-Net	Expt.: 700-2,000 (unpaired)	Cycle-GAN loss
	Lim <i>et al.</i> <sup>201</sup>	LR 3D RI tomogram	HR 3D RI tomogram	Residual 3D U-Net	Sim.: 1,600 pairs	$l_2$ -norm
Aberration correction	Ryu <i>et al.</i> <sup>202</sup>	LR 3D RI tomogram	HR 3D RI tomogram	3D U-Net	Expt.: 217 and 614 pairs	$l_2$ -norm
	Nguyen <i>et al.</i> <sup>203</sup>	Phase	Binary segmentation	U-Net	Expt.: 1,836 pairs	Cross entropy
	Ma <i>et al.</i> <sup>204</sup>	Hologram	Binary segmentation	U-Net	Expt.: 1,000 pairs	Cross entropy
	Lin <i>et al.</i> <sup>205</sup>	Phase and its gradient	Binary segmentation	U-Net and ResNet	Expt.: 1,800 pairs	Dice loss
	Xiao <i>et al.</i> <sup>206</sup>	Phase	Zernike coefficient	CNN	Expt.: 10,000 pairs	$l_2$ -norm
	Zhang <i>et al.</i> <sup>207</sup>	Aberrated intensity and phase	Phase	U-Net	Sim.: >10,000 groups	$l_2$ -norm or $l_1$ -norm
	Tang <i>et al.</i> <sup>208</sup>	Fixed tensor	Zernike coefficient	MLP (untrained)	Expt. and Sim.: 1	$l_2$ -norm and sparse constraints
	Dardikman <i>et al.</i> <sup>209,210</sup>	Wrapped phase	Unwrapped phase	ResNet	Sim.: 7,936 pairs	$l_2$ -norm

Wang <i>et al.</i> <sup>211</sup>	Wrapped phase	Unwrapped phase	U-Net and ResNet	Sim.: 30,000 pairs	$l_2$ -norm
He <i>et al.</i> <sup>212</sup>	Wrapped phase	Unwrapped phase	3D-ResNet	Expt.: ---	---
Ryu <i>et al.</i> <sup>213</sup>	Wrapped phase	Unwrapped phase	ReNet	Expt. and Sim.: ---	Total variation and variance
Dardikman <i>et al.</i> <sup>214</sup>	Wrapped phase	Unwrapped phase	ResNet	Expt.: 7,500 pairs	$l_2$ -norm
Qin <i>et al.</i> <sup>215</sup>	Wrapped phase	Unwrapped phase	U-Net and ResNet	Sim.: 30,000 pairs	$L_1$ -norm
Perera <i>et al.</i> <sup>216</sup>	Wrapped phase	Unwrapped phase	U-Net and LSTM	Sim.: 6,000 pairs	Total variation and variance
Park <i>et al.</i> <sup>217</sup>	Wrapped phase	Unwrapped phase	U-Net	Expt.: 5,200 pairs	GAN loss
Zhou <i>et al.</i> <sup>218</sup>	Wrapped phase and wrap count	Unwrapped phase	U-Net and EfficientNet	Sim.: 6,000 pairs	$l_1$ -norm and residual
Xu <i>et al.</i> <sup>219</sup>	Wrapped phase	Unwrapped phase	U-Net	Sim.: 6,000 pairs	SSIM
Zhou <i>et al.</i> <sup>220</sup>	Wrapped phase	Unwrapped phase	U-Net	Sim.: 158 and 1,036 pairs	GAN loss
Xie <i>et al.</i> <sup>221</sup>	Wrapped phase	Unwrapped phase	U-Net	Sim.: 17,000 pairs	$l_2$ -norm
Zhao <i>et al.</i> <sup>222</sup>	Wrapped phase and weighted map	Unwrapped phase	U-Net and ResNet	Sim.: 22,500 pairs	$l_1$ -norm
Liang <i>et al.</i> <sup>223</sup>	Wrapped phase	Wrap count	---	---	---
Spoorthi <i>et al.</i> <sup>224</sup>	Wrapped phase	Wrap count	SegNet	Sim.: 10,000 pairs	Cross entropy
Spoorthi <i>et al.</i> <sup>225</sup>	Wrapped phase	Wrap count	SegNet and DenseNet	Sim.: 30,000 pairs	Cross entropy and residue and $l_1$ -norm
Zhang and Liang <i>et al.</i> <sup>185,226</sup>	Wrapped phase	Wrap count	U-Net	Sim.: 9,500 pairs	Cross entropy
Zhang <i>et al.</i> <sup>227</sup>	Wrapped phase	Wrap count	DeepLab-V3+	Sim.: 25,000 pairs	Cross entropy
Zhu <i>et al.</i> <sup>228</sup>	Wrapped phase	Wrap count	DeepLab-V3+	Sim.: 20,000 pairs	Cross entropy
Wu <i>et al.</i> <sup>229</sup>	Wrapped phase	Wrap count	U-Net and FRRNet	Sim.: 12,000 pairs	Cross entropy
Zhao <i>et al.</i> <sup>230</sup>	Wrapped phase	Wrap count	ResNet	Sim.: 22,000 pairs	Cross entropy
Vengala <i>et al.</i> <sup>231,232</sup>	Wrapped phase	Wrap count and denoised wrapped phase	Y-Net	Sim.: 2,000 pairs	Cross entropy and $l_2$ -norm
Zhang <i>et al.</i> <sup>233</sup>	Wrapped phase	Wrap count	U-Net and ASPP and PSA	Sim.: 10,000 pairs	Weighted cross entropy
Huang <i>et al.</i> <sup>234</sup>	Wrapped phase	Wrap count	HRNet	Sim.: 30,000 pairs	Cross entropy
Wang <i>et al.</i> <sup>235</sup>	Wrapped phase	Wrap count	U-Net, ASPP and EEB	Sim.: ---	Cross entropy
Zhou <i>et al.</i> <sup>236</sup>	Wrapped count	Wrap count gradient	CNN	Sim.: 52,391 pairs	Cross entropy
Wang <i>et al.</i> <sup>237</sup>	Wrapped count and quality map	Wrap count gradient	U-Net	Sim.: 164,726 pairs	Cross entropy and dice loss
Sica <i>et al.</i> <sup>238</sup>	Wrapped count	Wrap count gradient	U-Net	Sim.: >70,000 pairs	Cross entropy, Jaccard distance, and $l_1$ -norm
Li <i>et al.</i> <sup>239</sup>	Wrapped count	Wrap count gradient	U-Net and ResNet	Sim.: 14,100 pairs	Cross entropy
Wu <i>et al.</i> <sup>240,241</sup>	Wrapped count	Discontinuity map	CNN and ASPP	Sim.: 8,000 pairs	$l_2$ -norm, cross entropy, and dice loss
Zhou <i>et al.</i> <sup>242</sup>	Residue image	Branch-cut map	CNN	Sim.: 26,928 pairs	Cross entropy

#### 4.1 Noise reduction

In addition to being part of the pre-processing in Section 2.2, noise reduction can also be performed after phase recovery (Fig. 23). Jeon *et al.*<sup>183</sup> applied the U-Net to perform speckle noise reduction on digital holographic images in an end-to-end manner. Their deep learning method takes only 0.92 s for a reconstructed hologram of 2048×2048, while other conventional methods take tens of seconds because of the requirement of multiple holograms. Choi *et al.*<sup>184</sup> introduced the cycle-GAN to train neural networks for noise reduction by

unpaired datasets. They demonstrated the advantages of this un-paired-data-driven method with tomograms of different cell samples in optical diffraction chromatography: the non-data-driven ways either remove coherent noise by blurring the entire images or perform no effective denoising, whereas their method can simultaneously remove the noise and preserve the features of the sample.

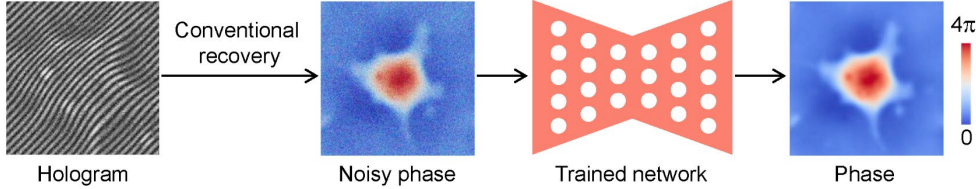


Fig. 23 Description of deep-learning-based phase noise reduction.

Zhang *et al.*<sup>185</sup> first proposed to suppress noise directly on the wrapped phase via a neural network. However, this direct way may lead to many wrong jumps in the wrapped phase, which results in larger errors in the unwrapped phase. Thus, Yan *et al.*<sup>186,187</sup> proposed to do noise reduction on the sine and cosine (numerator and denominator) images of the phase via a neural network, and then calculated the wrapped phase from denoised sine and cosine images by the arctangent function. Almost simultaneously, Montresor *et al.*<sup>188</sup> introduced the DnCNN into speckle noise reduction for phase data by their sine and cosine images. As it is difficult to simultaneously collect the phase data with and without speckle noise in an experimental manner, they used a simulator based on a double-diffraction system to numerically generate the dataset. Furthermore, their method yields comparable standard deviation to the WFT and better peak-to-valley, while costing less time. Building on this work, Tahon *et al.*<sup>189</sup> designed a dataset (HOLODEEP) for speckle noise reduction in soft conditions and used a shallower network for faster inference. To go further, they released a more comprehensive dataset for conditions of severe speckle noise<sup>190</sup>. Fang *et al.*<sup>191</sup> applied GAN to do speckle noise reduction for phase. Murdaca *et al.*<sup>192</sup> applied this deep-learning-based phase noise reduction to interferometric synthetic aperture radar (InSAR)<sup>243</sup>. The difference is that in addition to the sine and cosine images of the phase, the neural network also reduces noise for the amplitude images at the same time. Tang *et al.*<sup>193</sup> proposed to iteratively reduce the coherent noise in phase with an untrained U-Net.

#### 4.2 Resolution enhancement

Similar to Section 2.1, resolution enhancement can also be performed after phase recovery as post-processing (Fig. 24). Liu *et al.*<sup>194,195</sup> first used a neural network to infer the

corresponding high-resolution phase from the low-resolution phase. They trained two GANs with both a pixel super-resolution system and a diffraction-limited super-resolution system, which was demonstrated on biological thin tissue slices with the analysis of spatial frequency spectrum. Moreover, they pointed out that this idea can be extended to other resolution-limited imaging systems, such as using a neural network to build a passageway from off-axis holography to in-line holography. Later, Jiao *et al.*<sup>196</sup> proposed to infer the high-resolution noise-free phase from an off-axis-system-acquired low-resolution version with a trained U-Net. To collect the paired dataset, they developed a combined system with diffraction phase microscopy (DPM)<sup>244</sup> and spatial light interference microscopy (SLIM)<sup>22</sup> to generate both holograms from the same field of view. After training, the U-Net retains the advantages of both the high acquisition speed of DPM and the high transverse resolution of SLIM.

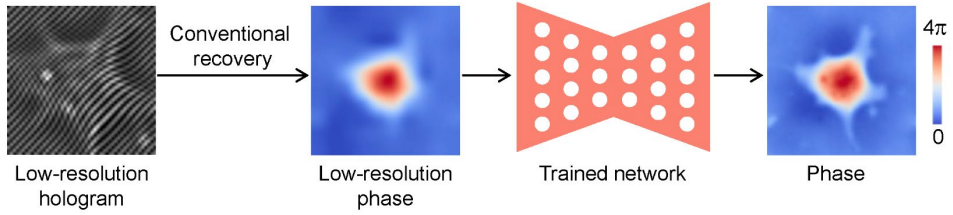


Fig. 24 Description of deep-learning-based phase resolution enhancement.

Subsequently, Butola *et al.*<sup>197</sup> extended this idea to partially spatially coherent off-axis holography, where the phase recovered at low-numerical-apertures objectives was used as input, and the phase recovered at high-numerical-apertures objectives was used as ground-truth. Since low-numerical-apertures objectives have a larger field of view, they aim to obtain a higher resolution at a larger field of view, i.e., a higher spatial bandwidth product. Meng *et al.*<sup>198</sup> used structured-illumination digital holographic microscopy (SI-DHM)<sup>245</sup> to collect the high-resolution phase as ground-truth. To supplement more high-frequency information by two cascaded neural networks, they used the low-resolution phase along with the high-resolution amplitude inferred from the first neural network both as inputs of the second neural network. Subsequently, Li *et al.*<sup>199</sup> extended this resolution-enhanced post-processing method to quantitative differential phase-contrast (qDPC)<sup>246</sup> imaging for high-resolution phase recovery from the least number of experimental measurements. To solve the problem of out-of-memory for the large size of the input, they disassembled the full-size input into some sub-patches. Moreover, they found that the U-Net trained on the paired dataset has a smaller error than the paired GAN and the unpaired GAN. While for GAN, there is more unreasonable information in the inferred phase, which is absent in the ground-truth. Gupta *et al.*<sup>200</sup> took

advantage of the high spatial bandwidth product of this method to achieve a classification throughput rate of 78,000 cells per second with an accuracy of 76.2%.

For ODT, due to the limited projection angle imposed by the numerical aperture of the objective lens, there are certain spatial frequency components that cannot be measured, which is called the missing cone problem. To address this problem via a neural network, Lim *et al.*<sup>201</sup> and Ryu *et al.*<sup>202</sup> built a 3D RI tomogram dataset for 3D U-Net training, in which the raw RI tomograms with poor axial resolution were used as input, and the resolution-enhanced RI tomograms from the iterative total variation algorithm were used as ground-truth. The trained 3D U-Net can infer the high-resolution version directly from the raw RI tomograms. They demonstrated the feasibility and generalizability using bacterial cells and a human leukemic cell line. Their deep-learning-based resolution-enhanced method outperforms conventional iterative methods by more than an order of magnitude in regularization performance.

#### 4.3 Aberration correction

For holography, especially in the off-axis case, the lens and the unstable environment of the sample introduce phase aberrations superimposing on the phase of the sample. To recover the pure phase of the sample, the unwanted phase aberrations should be eliminated physically or numerically. Physical approaches compensate for the phase aberrations by recovering the background phase without the sample from another hologram, which requires more setups and adjustments<sup>247,248</sup>.

As for numerical approaches, the compensation of the phase aberrations can be directly achieved by Zernike polynomial fitting (ZPF)<sup>249</sup> or principal-component analysis (PCA)<sup>250</sup>. Yet, in these numerical methods, the aberration is predicted from the whole phase, where the object area should not be considered as an aberration. Thus, before using the Zernike polynomial fitting, the neural network can be used to find out the object area and the background area to avoid the influence of the background area and improve the compensation effect (Fig. 25). This segmentation-based idea, namely CNN+ZPF, was first proposed by Nguyen *et al.*<sup>203</sup> in 2017. They manually made binary masks as ground-truth for each phase to distinguish the area of the background and sample. After comparison on different real samples, they found that the compensated result of the CNN+ZPF contains flatter background than that of PCA. However, the aberration in the initial phase makes it more difficult to do segmentation from the already weak phase distribution of the boundary features, especially for the large tilted phase aberrations. To address this problem, Ma *et al.*<sup>204</sup> proposed to do

segmentation with hologram instead of phase as neural network input. Lin *et al.*<sup>205</sup> applied the CNN+ZPF to real-time phase compensation with a phase-only SLM.

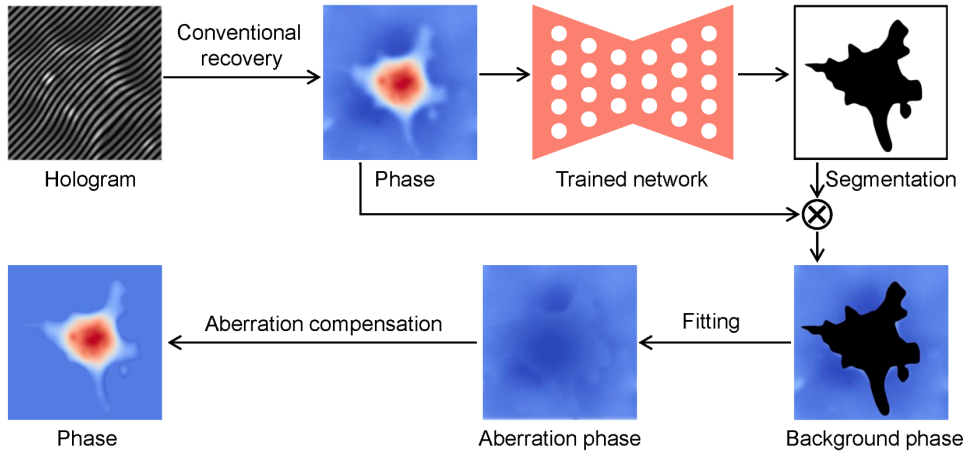


Fig. 25 Description of deep-learning-based phase aberration correction.

In addition to the way of CNN+ZPS, Xiao *et al.*<sup>206</sup> directly inferred the Zernike coefficient of aberration from the initial phase via a neural network, which costs less computation. They trained a neural network specifically for bone cells, and used this efficient method to achieve long-term morphological observation of living cells. Zhang *et al.*<sup>207</sup> used a trained neural network to infer the in-focus phase from the de-focus aberrated intensity and phase. Tang *et al.*<sup>208</sup> introduced the sparse constraint into the loss function and iteratively inferred the corresponding phase aberrations from the initial phase or fixed tensor with an untrained neural network and Zernike model.

#### 4.4 Phase unwrapping

In the interferometric and optimization-based phase recovery methods, the recovered light field is in the form of complex exponential. Hence the calculated phase is limited in the range of  $(-\pi, \pi]$  on account of the arctangent function. Therefore, the information of the sample cannot be obtained unless the absolute phase is first estimated from the wrapped phase, the so-called phase unwrapping. In addition to phase recovery, the phase unwrapping problem also arises in magnetic resonance imaging<sup>251</sup>, fringe projection profilometry<sup>252</sup>, and InSAR. Most conventional methods are based on the phase continuity assumption, and some cases, such as noise, breakpoints, and aliasing, all violate the Itoh condition and affect the effect of the conventional methods<sup>253</sup>. The advent of deep learning has made it possible to perform phase unwrapping in the above cases. According to the different use of the neural network, these deep-learning-based phase unwrapping methods can be divided into the following three

categories (Fig. 26)<sup>48</sup>. Deep-learning-performed regression method (dRG) estimates the absolute phase directly from the wrapped phase by a neural network (Fig. 26a)<sup>209–222</sup>. Deep-learning-performed wrap count method (dWC) first estimates the wrap count from the wrapped phase by a neural network, and then calculates the absolute phase from the wrapped phase and the estimate wrap count (Fig. 26b)<sup>185,223–233</sup>. Deep-learning-assisted method (dAS) first estimates the wrap count gradient or discontinuity from the wrapped phase by a neural network; next, either reconstruct the wrap count from the wrap count gradient and then calculate the absolute phase like dWC<sup>238,239</sup>, or directly use optimization-based or branch-cut algorithms to obtain the absolute phase from the warp count gradient or the discontinuity (Fig. 26c)<sup>236,237,240–242</sup>.

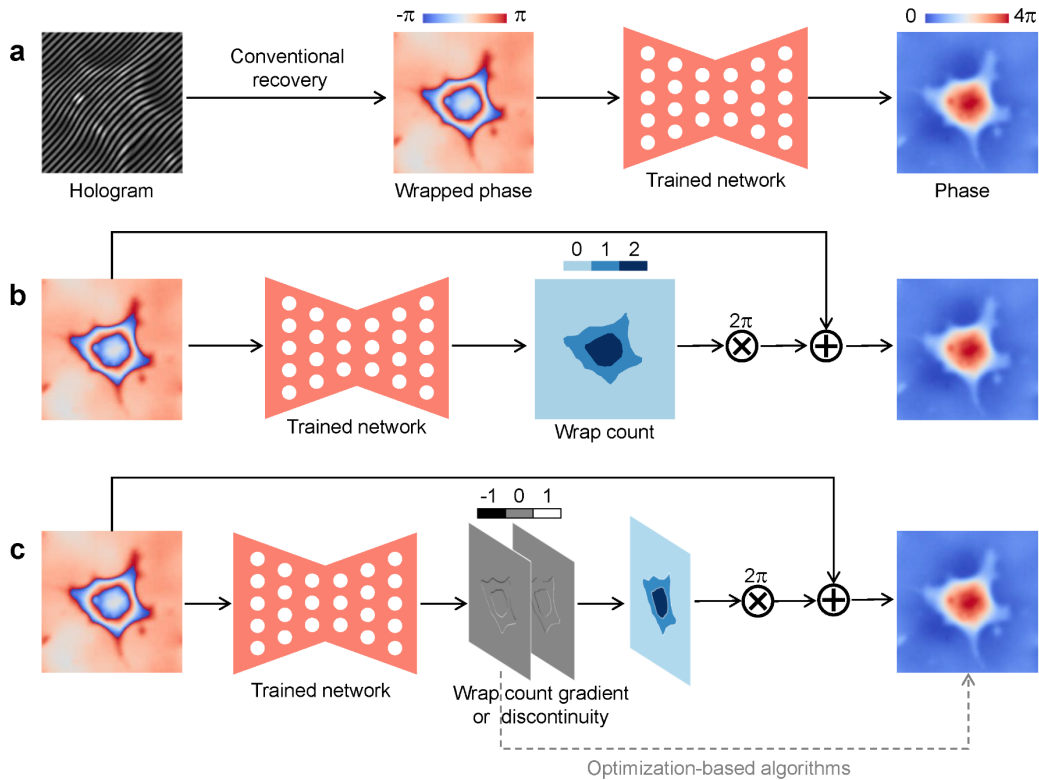


**Fig. 26 Description of deep-learning-based phase unwrapping.** **a** Deep-learning-performed regression method. **b** Deep-learning-performed wrap count method. **c** Deep-learning-assisted method.

**Deep-learning-performed regression method (dRG).** Dardikman *et al.*<sup>209</sup> presented the dRG method, which utilizes a residual-block-based CNN with a dataset of simulated steep cells. They also validated the dRG method post-processed by congruence in actual cells and compared it with the performance of the dWC method<sup>210</sup>. Then, Wang *et al.*<sup>211</sup> introduced the U-Net and a phase simulation generation method into the dRG method, wherein they

evaluated the trained network on real samples, examined the network's generalization ability through middle-layer visualization, and demonstrated the superiority of the dRG method over conventional methods in noisy and aliasing cases. In the same year, He *et al.*<sup>212</sup> and Ryu *et al.*<sup>213</sup> evaluated the ability of the 3D-ResNet and recurrent neural network (ReNet) to perform phase unwrapping using magnetic resonance imaging data. Dardikman *et al.*<sup>214</sup> released their real sample dataset as open-source. They demonstrated that the congruence could enhance the accuracy and robustness of the dRG method, particularly when dealing with a limited number of wrap count. Qin *et al.*<sup>215</sup> utilized a Res-UNet with a larger capacity to achieve higher accuracy and introduced two new evaluation indices. Perera *et al.*<sup>216</sup> and Park *et al.*<sup>217</sup> introduced the long short-term memory (LSTM) network and GAN into phase unwrapping. Zhou *et al.*<sup>218,254</sup> enhanced the robustness and efficiency of the dRG method by doing preprocessing and postprocessing steps for the U-Net with EfficientNet<sup>254</sup> backbone. Xu *et al.*<sup>219</sup> improved the accuracy and robustness of the U-Net by adding more middle-layers and skip connections and using a composite loss function. Zhou *et al.*<sup>220</sup> used the GAN in the InSAR phase unwrapping and avoided the blur in the unwrapped phase by combining the  $l_1$  loss and adversarial loss. Xie *et al.*<sup>221</sup> trained four networks for different noise levels, which made each network more focus on a specific noise level. Zhao *et al.*<sup>222</sup> added a weighted map as the prior to the neural network to make it more focused on the area near the jump edge, similar to an additional attention mechanism. Different from the above methods, Vithin *et al.*<sup>255,256</sup> proposed to use the Y-Net<sup>92</sup> to infer the phase gradients from a wrapped phase and then calculate the absolute phase.

**Deep-learning-performed wrap count method (dWC).** Liang *et al.*<sup>223</sup> and Spoorthi *et al.*<sup>224</sup> first proposed this idea in 2018. Spoorthi *et al.*<sup>224</sup> proposed a phase dataset generation method by adding and subtracting Gaussian functions with randomly varying mean and variance values, and used the clustering-based smoothness to alleviate the classification imbalance of the SegNet. Further, the prediction accuracy of their methods was improved by introducing the prior of absolute phase values and gradients into the loss function, which they called Phase-Net2.0<sup>225</sup>. Zhang and Liang *et al.*<sup>226,185</sup> sequentially used three networks to perform phase unwrapping by wrapped phase denoising, wrap count predicting, and post-processing. In addition, they proposed to generate a phase dataset by weighted adding Zernike polynomials of different orders. Immediately after, Zhang and Yan *et al.*<sup>227</sup> verified the performance of the network DeepLab-V3+, but the resulting wrap count still contained a small number of wrong pixels, which will propagate error through the whole phase maps in the conventional phase unwrapping process. They thus proposed to use refinement to correct

the wrong pixels. To further improve the unwrapped phase, Zhu *et al.*<sup>228</sup> proposed to use the median filter for the second post-processing to correct wrong pixels in the wrap count predictions. Wu *et al.*<sup>229</sup> enhanced the simulated phase dataset by adding the noise from real data. They also used the full-resolution residual network (FRRNet) with U-Net to further optimize the performance of the U-Net in the Doppler optical coherence tomography. By comparison with real data, their proposed network holds a higher accuracy than that of the Phase-Net and DeepLab-V3+. As for applying the dWC to point diffraction interferometer, Zhao *et al.*<sup>230</sup> proposed an image-analysis-based post-processed method to alleviate the classification imbalance of the task and adopted the iterative-closest-point stitching method to realize dynamic resolution. Vengala *et al.*<sup>92,231,232</sup> used the Y-Net<sup>92</sup> to reconstruct the wrap count and pure wrapped phase at the same time. Zhang *et al.*<sup>233</sup> added atrous spatial pyramid pooling (ASPP), positional self-attention (PSA), and edge-enhanced block (EEB) to the U-Net to get higher accuracy and stronger robustness than the networks used in the above methods. Huang *et al.*<sup>234</sup> applied the HRNet to the dWC methods. Their method still needs the median filter for post-processing, although the performance is better than that of the Phase-Net and DeepLab-V3+. Wang *et al.*<sup>235</sup> proposed another EEB based on Laplacian and Prewitt edge enhancement operators for the network, which further enhances classification accuracy and avoids the use of post-processing.

**Deep-learning-assisted method (dAS).** The conventional methods estimate the wrap count gradient under the phase continuity assumption, which hence is disturbed by disadvantages factors such as noise. To get rid of it, Zhou *et al.*<sup>236</sup> proposed to estimate the wrap count gradient via a neural network instead of conventional methods. Since the noisy wrapped phase and the corresponding correct wrap count gradient are used as training datasets, the trained neural network is able to estimate the correct wrap count gradient from the noisy wrapped phase without being limited by the phase continuity assumption. The correct result can be obtained by minimizing the difference between the unwrapped phase gradients and the network-output wrap count gradient. Further, Wang *et al.*<sup>237</sup> proposed to input a quality map, as the prior, together with the wrapped phase into the neural network to improve the accuracy of the estimated wrap count gradient. Almost simultaneously, Sica *et al.*<sup>238</sup> directly reconstructed the wrap count from the network-output wrap count gradient and then calculated the absolute phase, like dWC. On this basis, Li *et al.*<sup>239</sup> improved neural network estimation efficiency by using a single fusion gradient instead of the vertical and horizontal gradients. In addition to estimating the wrap count gradient via a neural network, Wu *et al.*<sup>240,241</sup> chose to estimate the horizontal and vertical discontinuities with a neural

network, and recover the absolute phase by the optimization-based algorithms. Instead of using the wrapped phase as the network input, Zhou *et al.*<sup>242</sup> embedded the neural network into the branch-cut algorithm to predict the branch-cut map from the residual image, which reduced the computational cost of the branch-cut algorithm.

## 5. Deep learning for phase processing

A summary of “Deep learning for phase processing” is presented in Table 5 and is described below, including segmentation (Section 5.1), classification (Section 5.2), and imaging modal transformation (Section 5.3).

**Table 5 Summary of “Deep learning for phase processing”**

Task	Reference	Input	Output	Network	Training dataset	Loss function
Segmentation	Yi <i>et al.</i> <sup>257</sup>	Phase of red blood cells	Segmentation map	FCN	Expt.: 35 pairs	---
	Ahmadvadah <i>et al.</i> <sup>258</sup>	Phase of cardiomyocyte	Segmentation map	FCN	Expt.: 2,000 pairs	---
	Kandel <i>et al.</i> <sup>259</sup>	Phase of sperm cells	Segmentation map	U-Net	Expt.: ---	Cross entropy
	Goswami <i>et al.</i> <sup>260</sup>	Phase of virus particles	Segmentation map	U-Net	Expt.: 1,000 pairs	Cross entropy
	Hu <i>et al.</i> <sup>261</sup>	Phase of ovary cells	Segmentation map	U-Net and EfficientNet	Expt.: 1,536 pairs	Focal loss and dice loss
	He <i>et al.</i> <sup>262</sup>	Phase of HeLa cells	Segmentation map	U-Net and EfficientNet	Expt.: 2,046 pairs	focal loss and dice loss
	Zhang <i>et al.</i> <sup>263</sup>	Phase of tissue slices	Segmentation map	mask R-CNN	Expt.: 196 pairs	Cross entropy
	Jiang <i>et al.</i> <sup>264</sup>	Phase and amplitude	Segmentation map	DeepLab-V3+	Expt.: 1,500 pairs	Cross entropy
Classification	Lee <i>et al.</i> <sup>265</sup>	2D RI tomogram	Segmentation map	U-Net	Expt.: 934 pairs	Cross entropy
	Choi <i>et al.</i> <sup>266</sup>	3D RI tomogram	Segmentation map	3D U-Net	Expt.: 105 pairs	Cross entropy and dice loss
	Jo <i>et al.</i> <sup>267</sup>	Phase of cells	Classification	CNN	Expt.: ---	Cross entropy
	Karandikar <i>et al.</i> <sup>268</sup>	Phase of cells	Classification	CNN	Expt.: 300	Cross entropy
	Zhang <i>et al.</i> <sup>269</sup>	Phase of tissue slices	Classification	VGG	Expt.: 1,660	Cross entropy
	Butola <i>et al.</i> <sup>270</sup>	Phase of sperm cells	Classification	CNN	Expt.: 10,163	Cross entropy
	Li <i>et al.</i> <sup>271</sup>	Phase of cells	Classification	AlexNet	Expt.: 272	Cross entropy
	Shu <i>et al.</i> <sup>272</sup>	Phase of cells	Classification	Cascaded ResNet	Expt.: 1,521	Cross entropy
	Pitkäaho <i>et al.</i> <sup>273</sup>	Phase and manual feature	Classification	CNN	Expt.: 2,451	---
	O'Connor <i>et al.</i> <sup>274</sup>	Transfer-learning and manual feature from phase	Classification	LSTM	Expt.: 303	---
	O'Connor <i>et al.</i> <sup>275</sup>	Transfer-learning and manual feature from phase	Classification for COVID-19	LSTM	Expt.: 1,474	---
	Ryu <i>et al.</i> <sup>276</sup>	3D RI tomogram	Classification (2 and 5 types)	3D CNN	Expt.: 1,782	Cross entropy
	Kim <i>et al.</i> <sup>277</sup>	3D RI tomogram	Classification (19 types)	3D CNN	Expt.: 10,556	Cross entropy
	Wang <i>et al.</i> <sup>278</sup>	Time-lapse amplitude and phase	Classification (3 types)	Pseudo-3D DensNet	Expt.: 16,309	Cross entropy
	Liu <i>et al.</i> <sup>279</sup>	Time-lapse phase	Classification	Pseudo-3D DensNet	Expt.: 5,622	Cross entropy
	Ben Baruch <i>et al.</i> <sup>280</sup>	Phase and spatio-temporal fluctuation map	Classification	ResNet	Expt.: 216 videos	Cross entropy
	Singla <i>et al.</i> <sup>281</sup>	Phase of three wavelengths	Classification	CNN	Expt.: 16,200	---
	İşil <i>et al.</i> <sup>282</sup>	Phase and amplitude of three wavelengths	Classification	DensNet	Expt.: 33,768	Cross entropy
	Pitkäaho <i>et al.</i> <sup>283</sup>	Phase and amplitude	Classification	CNN	Expt.: ---	---

Imaging modal transformation	Lam <i>et al.</i> <sup>284–286</sup>	Phase and amplitude	Classification	CNN	Sim.: >1,000 Expt.: 4,000	---
	Terbe <i>et al.</i> <sup>287</sup>	Phase and amplitude in different defocus distances	Classification (7 types)	3D ResNet	Expt.: >9,000	Cross entropy
	Wu <i>et al.</i> <sup>288</sup>	Real and imaginary	Classification (5 types)	ResNet	Expt.: 7,000	Cross entropy
	Wu <i>et al.</i> <sup>289</sup>	Real and imaginary	Bright-field image	U-Net	Expt.: 30,000 pairs	GAN loss
	Terbe <i>et al.</i> <sup>290</sup>	Amplitude and phase	Bright-field image	U-Net	Expt.: 3000 unpaired	Cycle-GAN loss
	Rivenson <i>et al.</i> <sup>291</sup>	Phase of tissue slices	Stained bright-field image	U-Net	Expt.: >2,000 pairs	GAN loss
	Wang <i>et al.</i> <sup>292</sup>	Phase of tissue slices	Stained bright-field or fluorescence image	U-Net	Expt.: 1,000 unpaired	Cycle-GAN loss
	Liu <i>et al.</i> <sup>293</sup>	Amplitude and phase of three wavelength	Stained bright-field image	U-Net	Expt.: 8,928 pairs	GAN loss
	Nygåte <i>et al.</i> <sup>294</sup>	Phase and gradients of sperm cells	Stained bright-field image	U-Net	Expt.: 1,100 pairs	GAN loss
	Guo <i>et al.</i> <sup>295</sup>	Phase, retardance and Orientation	Fluorescence image	2.5D U-Net	Expt.: 200 full brain sections	$l_1$ -norm
	Kandel <i>et al.</i> <sup>296,297</sup>	Phase	Fluorescence image	U-Net	Expt.: 30–3,000 pairs	$l_2$ -norm
	Guo <i>et al.</i> <sup>298</sup>	Phase at different depths	Fluorescence images at different depths	U-Net	Expt.: 200 pairs	$l_2$ -norm
	Chen <i>et al.</i> <sup>299,300</sup>	Three neighbouring phase	Corresponding central fluorescence image	U-Net and EfficientNet	Expt.: 20 z-stacks	$l_2$ -norm
	Jo <i>et al.</i> <sup>301</sup>	3D RI tomogram	3D fluorescence image	3D U-Net	Expt.: 1,600 pairs	$l_2$ -norm and gradient difference

## 5.1 Segmentation

Image segmentation, aiming to divide all pixels into different regions of interest, is widely used in biomedical analysis and diagnosis. For un-labeled cells or tissues, the contrast of the bright field intensity is low and thus inefficient to be used for image segmentation. Therefore, segmentation according to the phase distribution of cells or tissues becomes a potentially more efficient way. Given the great success of CNNs in semantic segmentation<sup>302</sup>, it seems that we can easily transplant it for phase segmentation, that is, doing segmentation with the phase as input of the neural network (Fig. 27).

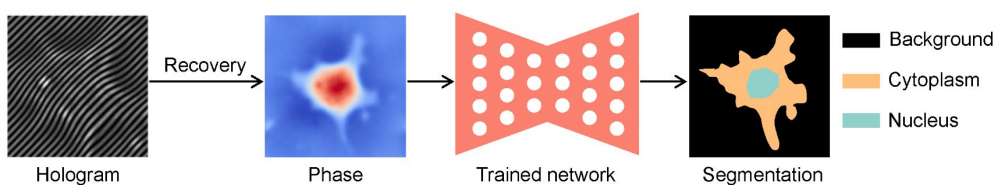


Fig. 27 Description of deep-learning-based segmentation from the phase.

To the best of our knowledge, early in 2013, Yi *et al.*<sup>303</sup> first proposed to do segmentation from the phase distribution for the red blood cells, although using a non-learning image-processing-based algorithm. To improve the segmentation accuracy in the case of heavily overlapped and multiple touched cells, they first introduced the fully convolutional network (FCN)<sup>302</sup> into phase segmentation<sup>257</sup>. Earlier in the same year, Nguyen *et al.*<sup>304</sup> used the random forest algorithm to segment prostate cancer tissue from the phase

distribution. Ahmadzadeh *et al.*<sup>258</sup> used the FCN-based phase segmentation to do nucleus extraction for cardiomyocyte characterization. Subsequently, the U-Net was used for phase segmentation in multiple biomedical applications, such as segmentation of the sperm cells' ultrastructure for assisted reproductive technologies<sup>259</sup>, SARS-CoV-2 detection<sup>260</sup>, cells live-dead assay<sup>261</sup>, and cells cycle-stage detection<sup>262</sup>. In addition, other types of neural networks were used for phase segmentation, including the mask R-CNN for cancer screening<sup>263</sup> and the DeepLab-V3+ for cytometric analysis<sup>264</sup>.

Further than the phase, the RI from ODT can be used to segment a sample in three dimensions. Lee *et al.*<sup>265</sup> obtained the 3D shape and position of the organelles by 2D segmentation of the RI tomograms at different depths, which are respectively used for the analysis of the morphological and biochemical parameters of breast cancer cells' nuclei. As a more direct and efficient way, Choi *et al.*<sup>266</sup> used a 3D U-Net to segment subcellular compartments directly from a single 3D RI tomogram.

## 5.2 Classification

Similar but different from the segmentation, the classification task is only responsible for giving the overall category of the input sample image, regardless of the specific pixels in the image. For the classification task, the phase provides more information related to the RI and three-dimensional topography of the sample, making it ideal for transparent samples such as cells, tissues, and microplastics<sup>267,305</sup>. Conventional machine learning algorithms first manually extract tens of features from the phase and then do classification with different models. Support vector machine<sup>306</sup>, as one of the most popular conventional machine learning strategies, is the most used strategy in phase classification<sup>307–314</sup>. In addition, some researchers used other conventional machine learning strategies, such as *k*-nearest neighbor<sup>315,316</sup>, fully-connected neural networks<sup>317,318</sup>, random forest<sup>319,320</sup>, and random subspace<sup>321</sup>. More generally, some researchers compared the accuracy of different conventional machine learning strategies in the same application context<sup>317,322–324</sup>.

Different from conventional machine learning strategies that require manual feature extraction, deep learning usually takes the phase or its further version directly as input, in which the deep CNNs will automatically perform feature extraction (Fig. 28). This automatic feature extraction strategy tends to achieve higher accuracy, but usually requires a larger number of paired input-label datasets as support. The use of phase as input to deep CNNs for classification was first reported in the work of Jo *et al.*<sup>267</sup>. They revealed that, for cells like anthrax spores, the accuracy of the neural network using phase as input is higher than that of

the neural network using binary morphology image obtained by conventional microscopy as input. Subsequently, this deep-learning-based phase classification method has been used in multiple applications, including assessment of T cell activation state<sup>268</sup>, cancer screening<sup>269</sup>, classification of sperm cells under different stress conditions<sup>270</sup>, prediction of living cells mitosis<sup>271</sup>, and classification of different white blood cells<sup>272</sup>. Accuracy in these applications is generally higher than 95% for the binary classification, but cannot achieve comparable accuracy in multi-type classification.

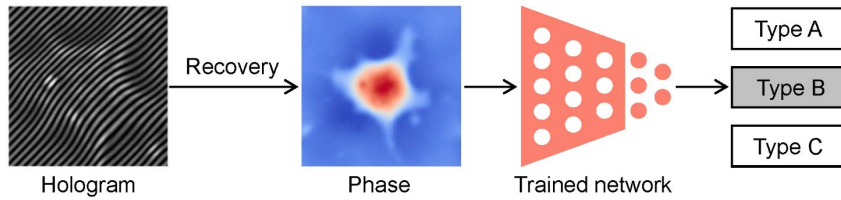


Fig. 28 Description of deep-learning-based classification from the phase.

On the one hand, combining the automatically extracted features of the neural network and the manually extracted features for classification can effectively improve the accuracy, which is because the manually extracted features add the prior of human experts to the classifier<sup>273–275</sup>. For instance, after adding the manual morphological features, the accuracy and area under the curve of healthy and sickle red blood cells classification are improved from 95.08% and 0.9665 to 98.36% and 1.0000<sup>274</sup>. On the other hand, the classification accuracy can also be enhanced by using higher dimensional data of the phase or other data together with the phase as the input of the neural network, such as 3D RI tomogram from the phase<sup>276,277</sup>, more phase in temporal dimension<sup>278–280</sup>, more phase in wavelength dimension<sup>281,282</sup>, and amplitude together with the phase<sup>283–288</sup>.

**3D RI tomogram from the phase (Fig. 29a).** Ryu *et al.*<sup>276</sup> used the 3D RI tomogram as the input of a neural network to classify different types of cells, and achieved an accuracy of 99.6% in the binary classification of lymphoid and myeloid cells, and of 96.7% even in five-type classification of white blood cells. For the multi-type classification, they also used the amplitude or phase of the same sample as input to train and test the same neural network, but only achieved an accuracy of 80.1% and 76.6%, respectively. Afterward, Kim *et al.*<sup>277</sup> from the same group applied this technology to microbial identification and reached 82.5% accuracy from an individual bacterial cell or cluster for the identification of 19 bacterial species.

**More phase in temporal dimension (Fig. 29b).** Wang *et al.*<sup>278</sup> used the amplitude and phase from time-lapse holograms as inputs to a pseudo-3D CNN to classify the type of

growing bacteria, shortening the detection time by >12 h compared with the environmental-protection-agency-approved methods. Likewise, Liu *et al.*<sup>279</sup> used the phase from time-lapse holograms as neural network inputs to infer the plaque-forming units probability for each pixel, achieving >90% plaque-forming units detection rate in <20 hours. By contrast, Batuch *et al.*<sup>280</sup> proposed to use the phase at a specific moment and the corresponding spatiotemporal fluctuation map as the inputs of a neural network to improve the accuracy of cancer cell classification.

**More phase in wavelength dimension (Fig. 29c).** Singla *et al.*<sup>281</sup> used the amplitude and phase of the red-green-blue color wavelengths as inputs of a neural network, thereby achieving a classification accuracy of 97.7% for healthy and malaria-infected red blood cells, and classification accuracy of 91.2% even for different stages of malaria-infection. Similarly, With the blessing of information from the red-green-blue color holograms, Isil *et al.*<sup>282</sup> achieved the high-accuracy four-type classification of algae, including accuracy of 94.5%, 96.7%, and 97.6% for *D. tertiolecta*, *Nitzschia*, and *Thalassiosira algae*, respectively.

**Amplitude together with the phase (Fig. 29d).** Lam *et al.*<sup>284,285</sup> used the amplitude and phase as the inputs of a neural network to do the classification of occluded and/or deformable objects, and achieved accuracy over 95%. With the same strategy, they performed a ten-type classification for biological tissues with an accuracy of 99.6%<sup>286</sup>. Further, Terbe *et al.*<sup>287</sup> proposed to use a type of volumetric network input by supplementing more amplitude and phase in different defocus distances. They built a more challenging dataset with seven classes by alga in different counts, small particles, and debris. The network with volumetric input outperforms the network with a single amplitude and phase inputs in all cases by approximately 4% accuracy. Similarly, Wu *et al.*<sup>288</sup> used real and imaginary parts of the complex field as network input to do a six-type classification for bioaerosols, and achieved an accuracy of over 94%.

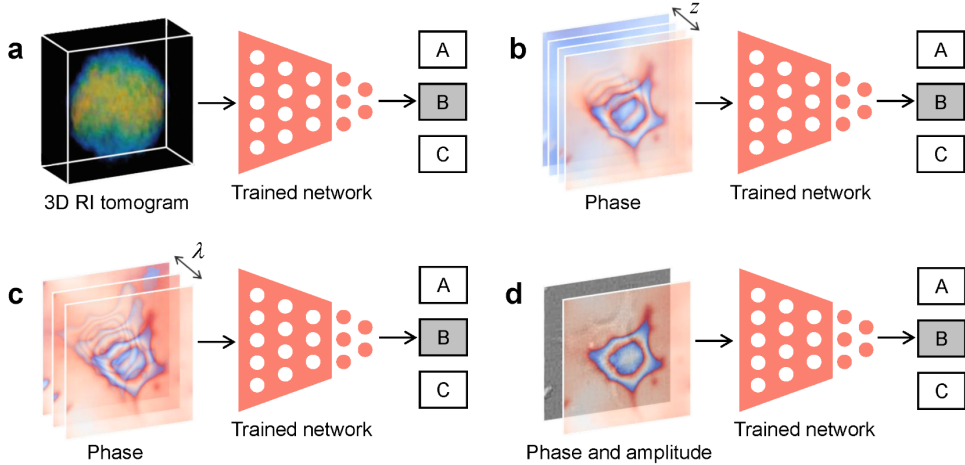


Fig. 29 Description of deep-learning-based classification from higher dimensional data of phase, including (a) 3D RI tomogram, (b) more phase in the temporal dimension, (c) more phase in wavelength dimension, and (d) amplitude together with the phase. **a** Adapted with permission from Ref. <sup>276</sup>. Distributed under Creative Commons (CC BY 4.0) license <http://creativecommons.org/licenses/by/4.0/>.

In pursuit of extreme speed for real-time classification, some researchers also choose to directly use the raw hologram recorded by the sensor as the input of the neural network to perform the classification tasks<sup>325–329</sup>. Since the information of amplitude and phase are encoded within a hologram, the hologram-trained neural network should achieve satisfactory accuracy with the support of sufficient feature extraction capabilities, which has been proven in practices including molecular diagnostics<sup>325</sup>, microplastic pollution assessment<sup>326–328</sup>, and neuroblastoma cells classification<sup>329</sup>.

### 5.3 Imaging modal transformation

Let us start this subsection with *image style transfer*, which aims to transfer a given image to another specified style under the premise of retaining the content of this image as much as possible<sup>330,331</sup>. Similarly, for a biological sample, its different parts usually have different RI, different chemical staining properties, or different fluorescent labeling properties, which makes it possible to achieve “image style transfer” from phase recovery/imaging to other different imaging modalities (Fig. 30).

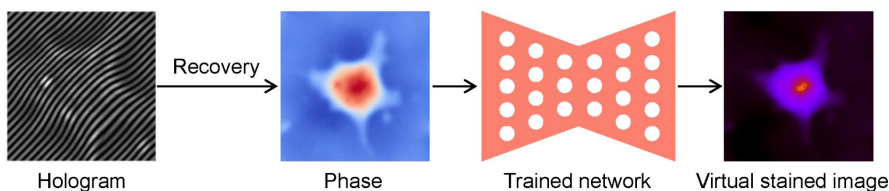


Fig. 30 Description of deep-learning-based imaging modal transformation.

The bright-field images of some color biological samples have sufficient contrast due to their strong absorption of visible light, so for such samples, bright-field imaging can be used as the target imaging modality, in which a neural network is used to transfer the complex image of the sample into its virtual bright-field image. In 2019, Wu *et al.*<sup>289</sup> presented the first implementation of this idea, called bright-field holography, in which a neural network was trained to transfer the back-propagated complex images from a single hologram to their corresponding speckle- and artifact-free bright-field images (Fig. 31a). This type of "bright-field holography" is able to infer a whole 3D volumetric image of a color sample like pollen from its single-snapshot hologram. Further, Terbe *et al.*<sup>290</sup> implemented "bright-field holography" with a cycle-GAN in the case of unpaired datasets.

For most transparent/colorless biological samples, chemical staining enables them to be clearly observed or imaged under bright-field microscopy. This allows the above "bright-field holography" to be used for transparent biological samples as well, which is called virtual staining. Rivenson *et al.*<sup>291</sup> applied this virtual staining technique to the inspection of histologically stained tissue slices and named it PhaseStain, in which a well-trained neural network was used to directly transfer the phase of tissue slices to their bright-field image of virtual staining (Fig. 31b). Using label-free slices of human skin, kidney, and liver tissue, they conducted an experimental demonstration of the efficacy of "PhaseStain" by imaging them with a holographic microscope. The resulting images were compared to those obtained through brightfield microscopy of the same tissue slices that were stained with HandE, Jones' stain, and Masson's trichrome stain, respectively. The reported "PhaseStain" greatly saves time and costs associated with the staining process. Similarly, Wang *et al.*<sup>292</sup> applied the "PhaseStain" in Fourier ptychographic microscopy and adapted it to unpaired dataset with a cycle-GAN. Liu *et al.*<sup>293</sup> used six images of amplitude and phase at three wavelengths as network input to infer the corresponding virtual staining version. In addition to tissue slices, Nygate *et al.*<sup>294</sup> demonstrated the advantages and potential of this deep learning virtual staining approach on a single biological cell like sperm (Fig. 31c). To improve the effectiveness of virtual staining, they used the phase gradients as an additional hand-engineered feature along with the phase as the input of the neural network. In order to assess the effectiveness of virtual staining, they used virtual staining images, phase, phase gradients, and stain-free bright-field images as input data for the five-type classification of sperm, and found that the recall values and F1 scores of virtual staining images were higher than those of other data twice or even four times. This type of single-cell staining approach provides ideal conditions for real-time analysis, such as rapid stain-free imaging flow cytometry.

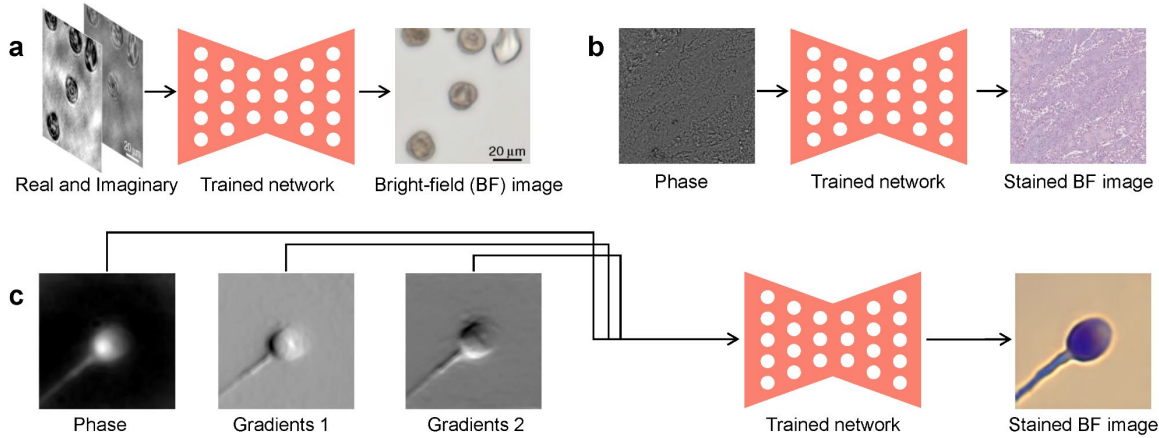


Fig. 31 Description of deep-learning-based virtual staining. **a** Inferring bright-field image from real and imaginary parts. **b** Inferring stained bright-field image from the phase. **c** Inferring stained bright-field image from the phase and its gradients. **a, b** Adapted with permission from ref.<sup>289,291</sup>. Distributed under Creative Commons (CC BY 4.0) license <http://creativecommons.org/licenses/by/4.0/>. **c** Adapted with permission from ref.<sup>294</sup>. Distributed under Creative Commons (CC BY-NC-ND 4.0) license <https://creativecommons.org/licenses/by-nc-nd/4.0/>.

Apart from imaging color or chemical-stained biological samples with bright-field microscopy, fluorescence microscopy can provide molecular-specific information by imaging fluorescence-labeled biological samples. As a labeled imaging method, fluorescence microscopy has insurmountable disadvantages, including phototoxicity and photobleaching. Guo *et al.*<sup>295</sup> proposed the concept of “transferring the physical-specific information to the molecular-specific information via a trained neural network” (Fig. 32a). Specifically, they used the phase and polarization of cell samples as multi-channel inputs to infer the corresponding fluorescence image, and further demonstrated its performance by imaging the architecture of brain tissue and prediction myelination in slices of a developing human brain. Almost simultaneously, Kandel *et al.*<sup>296</sup> used a neural network to infer the fluorescence-related subcellular specificity from a single phase, which they called phase imaging with computational specificity (Fig. 32b). With these label-free methods, they monitored the growth of both nuclei and cytoplasm for live cells and the arborization process in neural cultures over many days without loss of viability<sup>297</sup>. Guo *et al.*<sup>298</sup> further inferred the fluorescence images from the phase at different depths and performed 3D prediction for mitochondria. The above methods are performed on wide-field fluorescence microscopes, which cannot provide high-resolution 3D fluorescence data for neural networks as ground-truth. Hence, Chen *et al.*<sup>299,300</sup> presented an artificial confocal microscopy consisting of a commercial confocal microscope augmented by a laser scanning gradient light interference

microscopy system. To obtain the paired dataset, the artificial confocal microscopy can provide the phase of the samples in the same field of view as the fluorescence channel. With the support of deep learning, their proposed artificial confocal microscopy combines the benefits of non-destructive phase imaging with the depth sectioning and chemical specificity of confocal fluorescence microscopy.

Unlike inferring the fluorescence image from the phase, RI is an absolute and unbiased quantity of biological samples, so a neural network trained with RI as input is naturally applicable to new species. Jo *et al.*<sup>301</sup> thus built a bridge from ODT to fluorescence imaging via deep learning (Fig. 32c). They trained a neural network with the 3D RI tomogram as input and the corresponding fluorescence image as ground-truth. With the trained neural network, they performed various applications within the endogenous subcellular structures and dynamics profiling of intact living cells at unprecedented scales.

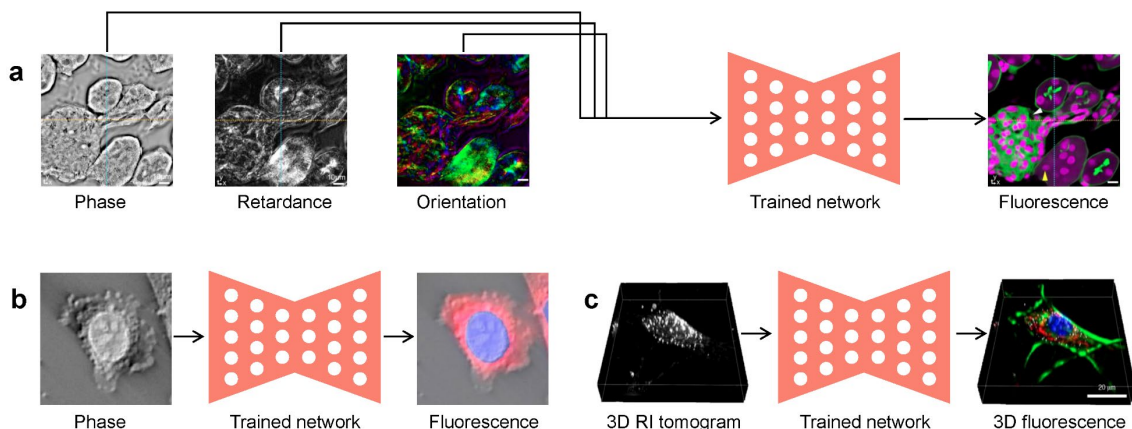


Fig. 32 Description of deep-learning-based label-free virtual fluorescence imaging. **a** Inferring fluorescence image from the phase, retardance, and orientation. **b** Inferring fluorescence image from the phase. **c** Inferring 3D fluorescence image from a 3D RI tomogram. **a, b** Adapted with permission from ref.<sup>295,296</sup>. Distributed under Creative Commons (CC BY 4.0) license <http://creativecommons.org/licenses/by/4.0/>. **c** Adapted with permission from ref.<sup>301</sup>. Springer Nature.

## 6. Conclusion and outlook

The introduction of deep learning provides a data-driven approach to various stages of phase recovery. Based on where they are used, we provided a comprehensive review of how neural networks work in phase recovery. Deep learning can provide pre-processing for phase recovery before it is performed, can be directly used to perform phase recovery, can post-process the initial phase obtained after phase recovery, or can use the recovered phase as input to implement specific applications. Despite the fact that deep learning provides

unprecedented efficiency and convenience for phase recovery, there are some common general points to keep in mind when using this learn-based tool.

**Datasets.** For supervised-learning mode, a good paired dataset provides enough rich and high-quality prior knowledge as a guide for neural network training. As one of the most common ways, some researchers choose to collect the intensity image of the real sample through the experimental setup as the input, and calculate the corresponding phase through conventional model-based methods as the ground-truth. Numerical simulations can be a convenient and efficient way to generate datasets for some cases, such as hologram resolution enhancement<sup>51</sup> and phase unwrapping<sup>48</sup>. The paired dataset thus implicitly contains the input-to-label mapping relationship in a large number of specific samples, which determines the upper limit of the ability of the trained neural network. For instance, if the dataset is collected under fixed settings, the trained neural network can only target a fixed device parameter (such as defocus distance, off-axis angle, and wavelength) or a certain class of samples, but cannot adapt to other situations that are not implied in the dataset. Of course, one can ameliorate this by using different settings and different types of samples when collecting datasets, thereby including various cases in the paired training samples, such as adapting to a certain range of defocus distance<sup>95,142</sup>, adapting to different aberrations<sup>99,108</sup>, adapting to different off-axis angles<sup>103</sup> and adapting to more types of samples<sup>107</sup>. One can use Shannon entropy to quantitatively represent the richness of the amount of information contained in the dataset, which directly affects the generalization ability of the trained neural network<sup>97</sup>. In addition, the spatial frequency content of the training samples in datasets also limits the ability of the trained neural network to resolve fine spatial features, which can be improved to some extent by pre-processing the power spectral density of the training samples<sup>96</sup>. For semi-supervised-learning mode, the cycle-GAN-based method uses an unpaired dataset to train the neural network for learning the mapping relationship between the input domain and the target domain, including phase recovery<sup>104,105,119</sup>, noise reduction<sup>184</sup>, resolution enhancement<sup>200</sup>, and imaging modal transformation<sup>290,292</sup>. As for self-supervised-learning mode, under the guidance of the input-only dataset and the forward physical model, neural networks can learn the inverse process<sup>127,128,131–134</sup>.

**Networks and loss functions.** Guided/Driven by the dataset, the neural network is trained to learn the mapping relationship from the input domain to the target domain by minimizing the difference between the actual output and the ground-truth (loss functions). Therefore, the fitting ability of the neural network itself and the perception ability of the loss function determines whether the implicit mapping relationship in the dataset can be well

internalized into the neural network. Conventional encoder-decoder-based neural networks have sufficient receptive fields and strong fitting capabilities, but down-sampling operations such as max-pooling lose some high-frequency information. Dilated convolutions can improve the receptive field while retaining more high-frequency information<sup>118</sup>. In addition, convolution in the Fourier frequency domain guarantees a global receptive field, since each pixel in the frequency domain contains contributions from all pixels in the spatial domain<sup>121,122</sup>. In order to make the neural network more focused on different spatial frequency information, one can also use two neural networks to learn the high- and low-frequency bands, respectively, and then use the third neural network to merge them into a full spatial frequency version<sup>144</sup>. Neural architecture search is another potential technology, which automatically searches out the optimal network structure from a large structure space<sup>123</sup>. As the most commonly used loss functions,  $l_2$ -norm and  $l_1$ -norm are more responsive to low-frequency information and less sensitive to high-frequency information. That is to say, the low-frequency information in the output of the neural network contributes more to the  $l_2$ -norm and  $l_1$ -norm loss functions than the high-frequency information. Therefore, some researchers have been trying to find more efficient loss functions, such as NPCC<sup>96</sup>, GAN loss<sup>109,116,117</sup>, and default feature perceptual loss of VGG layer<sup>143</sup>. So far, what kind of neural network and loss function is the best choice for phase recovery is still inconclusive.

**Network-only or physics-connect-network (PcN).** Network-only strategy aims to infer the final phase from the raw measured intensity image in an end-to-end fashion using a neural network. It's a one-shot approach, letting the neural network do it all in one go. Neural networks not only need to perform regularization to remove twin-image and self-interference-related spatial artifacts but also undertake the task of free-space light propagation. Therefore, the inference results of the network-only strategy are not satisfactory in some severely ill-posed cases, including weak-light illumination<sup>98</sup> and dense samples<sup>114</sup>. Since free-space light propagation is a well-characterized physical model that can be reproduced and enforced numerically, using numerical propagation in front can relieve the burden on the neural network and allow it to focus on learning regularization. In fact, PcN can indeed infer better results than network-only in the above ill-posed cases<sup>98,114</sup>. In another similar scheme, the neural network only performs the task of hologram generation before the phase-shifting algorithm, thus achieving better generalization ability than network-only<sup>62</sup>. In addition, using speckle-correlation processing before the neural network makes the trained neural network suitable for unknown scattering media and target objects<sup>332</sup>.

**Interpretability.** In phase recovery, learning-based deep learning techniques usually attempt to automatically learn a specific mapping relationship by optimizing/training neural network parameters with the real-world paired dataset. Deep neural networks usually adopt a multi-layer architecture and contain a large number of trainable parameters (even greater than millions), and are thus capable of learning complicated mapping relationships from datasets. Unlike physics-based algorithms, such network architectures that are general to various tasks often lack interpretability, meaning that it is difficult to discover what the neural network has learned internally and what the role of a particular parameter is by examining the trained parameters. This makes one helpless in practical applications when encountering a failure of neural network inference, in which they can neither analyze why the neural network failed for that sample nor make targeted improvements for the neural network to avoid this failure in subsequent uses. The algorithm unrolling/unfolding technique proposed by Gregor and LeCun gives hope for the interpretability of neural networks<sup>182</sup>, in which each iteration of physics-based iterative algorithms is represented as one layer of the neural network. One inference through such a neural network is equivalent to performing a fixed number of iterations of the physics-based iterative algorithm. Usually, physics-based parameters and regularization coefficients are transferred into the unrolled network as trainable parameters. In this way, the trained unrolled network can be interpreted as a physics-based iterative algorithm with a fixed number of iterations. In addition, the unrolled network naturally inherits prior structures and domain knowledge from a physics-based iterative algorithm, and thus its parameters can be efficiently trained with a small dataset.

**Uncertainty.** When actually using a trained neural network to do inference for a tested sample, its ground-truth is usually unknown, which makes it impossible to determine the reliability of the inferred results. To address this, Bayesian CNNs perform phase inference while giving uncertainty maps to describe the confidence measure of each pixel of the inferred result<sup>109,333–335</sup>. This uncertainty comes from both the model itself and the data, called epistemic uncertainty and aleatoric uncertainty, respectively. The network-output uncertainty maps are experimentally verified to be highly consistent with the real error map, which makes it possible to assess the reliability of inferred results in practical applications without any ground-truth<sup>109,335</sup>. In addition to Bayesian neural networks, there are three other uncertainty estimation techniques, including single deterministic methods, ensemble methods, and test time augmentation methods<sup>336</sup>.

**From electronic neural networks to optical neural networks.** So far, the artificial neural networks involved in this review mostly run in the hardware architecture with

electronics as the physical carrier such as the graphic processing unit, which is approaching its physical limit. Replacing electrons with photons is a potential route to high-speed, parallel and low-power artificial intelligence computing, especially optical neural networks<sup>337,338</sup>. Among them, spatial-structure-based optical neural networks, represented by the all-optical diffractive deep neural network<sup>339</sup>, are particularly suitable for image processing. Some examples have initially demonstrated the potential of using optical neural networks for phase recovery<sup>340,341</sup>.

There is enormous potential and efficiency in learning-based deep neural networks, while conventional physics-based methods are more reliable. We thus encourage the incorporation of physical models with deep neural networks, especially for those well modeling from the real world, rather than letting the deep neural network perform all tasks as *a black box*. One possible way is to consider the dataset, network structures, and loss functions as much as possible during the training stage to obtain a good pre-trained neural network; in actual use, the pre-trained neural network is used for one-time inference to deal with the situation with high real-time requirements, and the physical model is used to iteratively fine-tune the pre-trained neural network to obtain more accurate results.

## References

1. Born, M. & Wolf, E. *Principles of optics: electromagnetic theory of propagation, interference and diffraction of light.* (Pergamon Press, 1980).
2. Shechtman, Y. *et al.* Phase Retrieval with Application to Optical Imaging: A contemporary overview. *IEEE Signal Process. Mag.* **32**, 87–109 (2015).
3. Park, Y., Depeursinge, C. & Popescu, G. Quantitative phase imaging in biomedicine. *Nat. Photonics* **12**, 578–589 (2018).
4. Miao, J., Charalambous, P., Kirz, J. & Sayre, D. Extending the methodology of X-ray crystallography to allow imaging of micrometre-sized non-crystalline specimens. *Nature* **400**, 342–344 (1999).
5. Tyson, R. K. & Frazier, B. W. *Principles of Adaptive Optics.* (CRC Press, 2022).
6. Colomb, T. & Kühn, J. Digital Holographic Microscopy. in *Optical Measurement of Surface Topography* (ed. Leach, R.) 209–235 (Springer Berlin Heidelberg, 2011).
7. Klibanov, M. V., Sacks, P. E. & Tikhonravov, A. V. The phase retrieval problem. *Inverse Probl.* **11**, 1–28 (1995).
8. Goodman, J. W. *Introduction to Fourier optics.* (W.H. Freeman, Macmillan Learning, 2017).
9. Gabor, D. A New Microscopic Principle. *Nature* **161**, 777–778 (1948).
10. Teague, M. R. Deterministic phase retrieval: a Green's function solution. *J. Opt. Soc. Am.* **73**, 1434 (1983).
11. Zuo, C. *et al.* Transport of intensity equation: a tutorial. *Opt. Lasers Eng.* **135**, 106187 (2020).
12. Hartmann, J. Bemerkungen über den Bau und die Justirung von Spektrographen. *Z. Fuer Instrumentenkunde* **20**, 47–58 (1900).
13. Shack, R. V. & Platt, B. C. Production and use of a lenticular Hartmann screen. *J Opt Soc Am* **61**, 656–660 (1971).
14. Gerchberg, R. W. A practical algorithm for determination of phase from image and diffraction plane pictures. *Optik* **35**, 237–246 (1972).
15. Fienup, J. R. Phase retrieval algorithms: a comparison. *Appl. Opt.* **21**, 2758 (1982).

16. Fienup, J. R. Reconstruction of an object from the modulus of its Fourier transform. *Opt. Lett.* **3**, 27 (1978).
17. Faulkner, H. M. L. & Rodenburg, J. M. Movable Aperture Lensless Transmission Microscopy: A Novel Phase Retrieval Algorithm. *Phys. Rev. Lett.* **93**, 023903 (2004).
18. Rodenburg, J. M. & Faulkner, H. M. L. A phase retrieval algorithm for shifting illumination. *Appl. Phys. Lett.* **85**, 4795–4797 (2004).
19. Zheng, G., Horstmeyer, R. & Yang, C. Wide-field, high-resolution Fourier ptychographic microscopy. *Nat. Photonics* **7**, 739–745 (2013).
20. Yamaguchi, I. & Zhang, T. Phase-shifting digital holography. *Opt. Lett.* **22**, 1268 (1997).
21. Huang, P. S. & Zhang, S. Fast three-step phase-shifting algorithm. *Appl. Opt.* **45**, 5086 (2006).
22. Wang, Z. *et al.* Spatial light interference microscopy (SLIM). *Opt. Express* **19**, 1016 (2011).
23. Leith, E. N. & Upatnieks, J. Reconstructed Wavefronts and Communication Theory\*. *J. Opt. Soc. Am.* **52**, 1123 (1962).
24. Baek, Y., Lee, K., Shin, S. & Park, Y. Kramers–Kronig holographic imaging for high-space-bandwidth product. *Optica* **6**, 45 (2019).
25. Huang, Z. & Cao, L. High Bandwidth-Utilization Digital Holographic Multiplexing: An Approach Using Kramers–Kronig Relations. *Adv. Photonics Res.* **3**, 2100273 (2022).
26. Luo, G., He, Y., Shu, X., Zhou, R. & Blu, T. Complex wave and phase retrieval from a single off-axis interferogram. *J. Opt. Soc. Am. A* **40**, 85 (2023).
27. Kim, M. K. Principles and techniques of digital holographic microscopy. *J. Photonics Energy* 018005 (2010) doi:10.1117/6.0000006.
28. Guigay, J. P. Fourier transform analysis of Fresnel diffraction patterns and in-line holograms. *Optik* **49**, 121–125 (1977).
29. Paganin, D. & Nugent, K. A. Noninterferometric Phase Imaging with Partially Coherent Light. *Phys. Rev. Lett.* **80**, 2586–2589 (1998).
30. Arnison, M. R., Larkin, K. G., Sheppard, C. J. R., Smith, N. I. & Cogswell, C. J. Linear phase imaging using differential interference contrast microscopy. *J. Microsc.* **214**, 7–12 (2004).

31. Zuo, C., Sun, J., Feng, S., Zhang, M. & Chen, Q. Programmable aperture microscopy: A computational method for multi-modal phase contrast and light field imaging. *Opt. Lasers Eng.* **80**, 24–31 (2016).
32. Bon, P., Maucort, G., Wattellier, B. & Monneret, S. Quadriwave lateral shearing interferometry for quantitative phase microscopy of living cells. *Opt. Express* **17**, 13080 (2009).
33. Allen, L. J. & Oxley, M. P. Phase retrieval from series of images obtained by defocus variation. *Opt. Commun.* **199**, 65–75 (2001).
34. Pedrini, G., Osten, W. & Zhang, Y. Wave-front reconstruction from a sequence of interferograms recorded at different planes. *Opt. Lett.* **30**, 833 (2005).
35. Greenbaum, A. & Ozcan, A. Maskless imaging of dense samples using pixel super-resolution based multi-height lensfree on-chip microscopy. *Opt. Express* **20**, 3129 (2012).
36. Candes, E. J., Li, X. & Soltanolkotabi, M. Phase Retrieval via Wirtinger Flow: Theory and Algorithms. *IEEE Trans. Inf. Theory* **61**, 1985–2007 (2015).
37. Wang, G., Giannakis, G. B. & Eldar, Y. C. Solving Systems of Random Quadratic Equations via Truncated Amplitude Flow. *IEEE Trans. Inf. Theory* **64**, 773–794 (2018).
38. Candès, E. J., Strohmer, T. & Voroninski, V. PhaseLift: Exact and Stable Signal Recovery from Magnitude Measurements via Convex Programming. *Commun. Pure Appl. Math.* **66**, 1241–1274 (2013).
39. Goodfellow, I., Bengio, Y. & Courville, A. *Deep Learning*. (MIT Press, 2016).
40. Jin, K. H., McCann, M. T., Froustey, E. & Unser, M. Deep Convolutional Neural Network for Inverse Problems in Imaging. Preprint at <https://doi.org/10.48550/arXiv.1611.03679> (2016).
41. Mait, J. N., Euliss, G. W. & Athale, R. A. Computational imaging. *Adv. Opt. Photonics* **10**, 409 (2018).
42. Leijnen, S. & Veen, F. V. The Neural Network Zoo. in *IS4SI 2019 Summit* 9 (MDPI, 2020). doi:10.3390/proceedings2020047009.
43. LeCun, Y. *et al.* Backpropagation Applied to Handwritten Zip Code Recognition. *Neural Comput.* **1**, 541–551 (1989).

44. Barbastathis, G., Ozcan, A. & Situ, G. On the use of deep learning for computational imaging. *Optica* **6**, 921 (2019).
45. Rivenson, Y., Wu, Y. & Ozcan, A. Deep learning in holography and coherent imaging. *Light Sci. Appl.* **8**, 85 (2019).
46. Zeng, T., Zhu, Y. & Lam, E. Y. Deep learning for digital holography: a review. *Opt. Express* **29**, 40572 (2021).
47. Situ, G. Deep holography. *Light Adv. Manuf.* **3**, 1 (2022).
48. Wang, K., Kemao, Q., Di, J. & Zhao, J. Deep learning spatial phase unwrapping: a comparative review. *Adv. Photonics Nexus* **1**, 014001 (2022).
49. Dong, J. *et al.* Phase Retrieval: From Computational Imaging to Machine Learning: A tutorial. *IEEE Signal Process. Mag.* **40**, 45–57 (2023).
50. Luo, Z. *et al.* Pixel super-resolution for lens-free holographic microscopy using deep learning neural networks. *Opt. Express* **27**, 13581 (2019).
51. Byeon, H., Go, T. & Lee, S. J. Deep learning-based digital in-line holographic microscopy for high resolution with extended field of view. *Opt. Laser Technol.* **113**, 77–86 (2019).
52. Xin, L. *et al.* Three-dimensional reconstruction of super-resolved white-light interferograms based on deep learning. *Opt. Lasers Eng.* **145**, 106663 (2021).
53. Ren, Z., So, H. K.-H. & Lam, E. Y. Fringe Pattern Improvement and Super-Resolution Using Deep Learning in Digital Holography. *IEEE Trans. Ind. Inform.* **15**, 6179–6186 (2019).
54. Yan, K. *et al.* Fringe pattern denoising based on deep learning. *Opt. Commun.* **437**, 148–152 (2019).
55. Lin, B., Fu, S., Zhang, C., Wang, F. & Li, Y. Optical fringe patterns filtering based on multi-stage convolution neural network. *Opt. Lasers Eng.* **126**, 105853 (2020).
56. Hao, F., Tang, C., Xu, M. & Lei, Z. Batch denoising of ESPI fringe patterns based on convolutional neural network. *Appl. Opt.* **58**, 3338 (2019).
57. Zhou, W.-J. *et al.* Speckle noise reduction in digital holograms based on Spectral Convolutional Neural Networks (SCNN). in *Holography, Diffractive Optics, and Applications IX* (eds. Zhou, C., Sheng, Y. & Cao, L.) 6 (SPIE, 2019). doi:10.1117/12.2537685.

58. Zhou, W.-J., Liu, S., Zhang, H., Yu, Y. & Poon, T.-C. A Deep Learning Approach for Digital Hologram Speckle Noise Reduction. in *Imaging and Applied Optics Congress HTu5B.5* (Optica Publishing Group, 2020). doi:10.1364/DH.2020.HTu5B.5.
59. Reyes-Figueroa, A., Flores, V. H. & Rivera, M. Deep neural network for fringe pattern filtering and normalization. *Appl. Opt.* **60**, 2022 (2021).
60. Gurrola-Ramos, J., Dalmau, O. & Alarcón, T. U-Net based neural network for fringe pattern denoising. *Opt. Lasers Eng.* **149**, 106829 (2022).
61. Zhang, Q. *et al.* Deep Phase Shifter for Quantitative Phase Imaging. Preprint at <https://doi.org/10.48550/arXiv.2003.03027> (2020).
62. Zhang, Q. *et al.* Phase-shifting interferometry from single frame in-line interferogram using deep learning phase-shifting technology. *Opt. Commun.* **498**, 127226 (2021).
63. Yan, K., Khan, A., Asundi, A., Zhang, Y. & Yu, Y. Virtual temporal phase-shifting phase extraction using generative adversarial networks. *Appl. Opt.* **61**, 2525 (2022).
64. Zhao, Y., Hu, K. & Liu, F. One-shot phase retrieval method for interferometry using a multi-stage phase-shifting network. *IEEE Photonics Technol. Lett.* **35**, 577–580 (2022).
65. Huang, T. *et al.* Single-shot Fresnel incoherent correlation holography via deep learning based phase-shifting technology. *Opt. Express* **31**, 12349 (2023).
66. Wu, B., Zhang, Q., Liu, T., Ma, Q. & Li, J. RSAGAN: Rapid self-attention generative adversarial nets for single-shot phase-shifting interferometry. *Opt. Lasers Eng.* **168**, 107672 (2023).
67. Luo, H., Xu, J., Zhong, L., Lu, X. & Tian, J. Diffraction-Net: a robust single-shot holography for multi-distance lensless imaging. *Opt. Express* **30**, 41724 (2022).
68. Li, J. *et al.* Quantitative phase imaging in dual-wavelength interferometry using a single wavelength illumination and deep learning. *Opt. Express* **28**, 28140 (2020).
69. Li, J., Zhang, Q., Zhong, L. & Lu, X. Hybrid-net: a two-to-one deep learning framework for three-wavelength phase-shifting interferometry. *Opt. Express* **29**, 34656 (2021).

70. Xu, X., Xie, M., Ji, Y. & Wang, Y. Dual-wavelength interferogram decoupling method for three-frame generalized dual-wavelength phase-shifting interferometry based on deep learning. *J. Opt. Soc. Am. A* **38**, 321 (2021).
71. Pitkäaho, T., Manninen, A. & Naughton, T. J. Performance of Autofocus Capability of Deep Convolutional Neural Networks in Digital Holographic Microscopy. in *Digital Holography and Three-Dimensional Imaging* W2A.5 (OSA, 2017). doi:10.1364/DH.2017.W2A.5.
72. Ren, Z., Xu, Z. & Lam, E. Y. M. Autofocusing in digital holography using deep learning. in *Three-Dimensional and Multidimensional Microscopy: Image Acquisition and Processing XXV* (eds. Brown, T. G., Cogswell, C. J. & Wilson, T.) 56 (SPIE, 2018). doi:10.1117/12.2289282.
73. Son, K., Jeong, W., Jeon, W. & Yang, H. Autofocusing algorithm for a digital holographic imaging system using convolutional neural networks. *Jpn. J. Appl. Phys.* **57**, 09SB02 (2018).
74. Couturier, R., Salomon, M., Zeid, E. A. & Jaoude, C. A. Using Deep Learning for Object Distance Prediction in Digital Holography. in *2021 International Conference on Computer, Control and Robotics (ICCCR)* 231–235 (IEEE, 2021). doi:10.1109/ICCCR49711.2021.9349275.
75. Ren, Z., Xu, Z. & Lam, E. Y. Learning-based nonparametric autofocusing for digital holography. *Optica* **5**, 337 (2018).
76. Pitkäaho, T., Manninen, A. & Naughton, T. J. Focus prediction in digital holographic microscopy using deep convolutional neural networks. *Appl. Opt.* **58**, A202 (2019).
77. Jaferzadeh, K., Hwang, S.-H., Moon, I. & Javidi, B. No-search focus prediction at the single cell level in digital holographic imaging with deep convolutional neural network. *Biomed. Opt. Express* **10**, 4276 (2019).
78. Moon, I. & Jaferzadeh, K. Automated digital holographic image reconstruction with deep convolutional neural networks. in *Three-Dimensional Imaging, Visualization, and Display 2020* (eds. Martínez-Corral, M., Javidi, B., Stern, A. & Matoba, O.) 10 (SPIE, 2020). doi:10.1117/12.2554533.
79. Tang, J. *et al.* Single-Shot Diffraction Autofocusing: Distance Prediction via an Untrained Physics-Enhanced Network. *IEEE Photonics J.* **14**, 1–6 (2022).

80. Cuenat, S. & Couturier, R. Convolutional Neural Network (CNN) vs Vision Transformer (ViT) for Digital Holography. in *2022 2nd International Conference on Computer, Control and Robotics (ICCCR)* 235–240 (IEEE, 2022). doi:10.1109/ICCCR54399.2022.9790134.
81. Cuenat, S. *et al.* Fast autofocusing using tiny transformer networks for digital holographic microscopy. *Opt. Express* **30**, 24730 (2022).
82. Lee, J.-S. Autofocusing using deep learning in off-axis digital holography. in *Imaging and Applied Optics 2018 (3D, AO, AIO, COSI, DH, IS, LACSEA, LS&C, MATH, pcaOP)* DTh1C.4 (OSA, 2018). doi:10.1364/DH.2018.DTh1C.4.
83. Shimobaba, T., Kakue, T. & Ito, T. Convolutional Neural Network-Based Regression for Depth Prediction in Digital Holography. in *2018 IEEE 27th International Symposium on Industrial Electronics (ISIE)* 1323–1326 (IEEE, 2018). doi:10.1109/ISIE.2018.8433651.
84. Bishara, W., Su, T.-W., Coskun, A. F. & Ozcan, A. Lensfree on-chip microscopy over a wide field-of-view using pixel super-resolution. *Opt. Express* **18**, 11181 (2010).
85. Dong, C., Loy, C. C., He, K. & Tang, X. Image Super-Resolution Using Deep Convolutional Networks. *IEEE Trans. Pattern Anal. Mach. Intell.* **38**, 295–307 (2016).
86. Rivenson, Y. *et al.* Deep learning microscopy. *Optica* **4**, 1437 (2017).
87. Wang, H. *et al.* Deep learning enables cross-modality super-resolution in fluorescence microscopy. *Nat. Methods* **16**, 103–110 (2019).
88. Wang, Z., Simoncelli, E. P. & Bovik, A. C. Multiscale structural similarity for image quality assessment. in *The Thirty-Seventh Asilomar Conference on Signals, Systems & Computers, 2003* 1398–1402 (IEEE, 2003). doi:10.1109/ACSSC.2003.1292216.
89. Kemao, Q. Windowed Fourier transform for fringe pattern analysis. *Appl. Opt.* **43**, 2695 (2004).
90. Zhang, K., Zuo, W., Chen, Y., Meng, D. & Zhang, L. Beyond a Gaussian Denoiser: Residual Learning of Deep CNN for Image Denoising. *IEEE Trans. Image Process.* **26**, 3142–3155 (2017).
91. Zhang, K., Zuo, W. & Zhang, L. FFDNet: Toward a Fast and Flexible Solution for CNN-Based Image Denoising. *IEEE Trans. Image Process.* **27**, 4608–4622 (2018).

92. Wang, K., Dou, J., Kemao, Q., Di, J. & Zhao, J. Y-Net: a one-to-two deep learning framework for digital holographic reconstruction. *Opt. Lett.* **44**, 4765 (2019).
93. Zamir, S. W. *et al.* Multi-Stage Progressive Image Restoration. in *Proceedings of the IEEE/CVF Conference on Computer Vision and Pattern Recognition (CVPR)* 14821–14831 (2021).
94. Oh, S., Hwang, C.-Y., Jeong, I. K., Lee, S.-K. & Park, J.-H. Fast focus estimation using frequency analysis in digital holography. *Opt. Express* **22**, 28926 (2014).
95. Sinha, A., Lee, J., Li, S. & Barbastathis, G. Lensless computational imaging through deep learning. *Optica* **4**, 1117 (2017).
96. Li, S. & Barbastathis, G. Spectral pre-modulation of training examples enhances the spatial resolution of the phase extraction neural network (PhENN). *Opt. Express* **26**, 29340 (2018).
97. Deng, M. *et al.* On the interplay between physical and content priors in deep learning for computational imaging. *Opt. Express* **28**, 24152 (2020).
98. Goy, A., Arthur, K., Li, S. & Barbastathis, G. Low Photon Count Phase Retrieval Using Deep Learning. *Phys. Rev. Lett.* **121**, 243902 (2018).
99. Wang, H., Lyu, M. & Situ, G. eHoloNet: a learning-based end-to-end approach for in-line digital holographic reconstruction. *Opt. Express* **26**, 22603 (2018).
100. Nguyen, T., Xue, Y., Li, Y., Tian, L. & Nehmetallah, G. Deep learning approach for Fourier ptychography microscopy. *Opt. Express* **26**, 26470 (2018).
101. Cheng, Y. F. *et al.* Illumination pattern design with deep learning for single-shot Fourier ptychographic microscopy. *Opt. Express* **27**, 644 (2019).
102. Cherukara, M. J., Nashed, Y. S. G. & Harder, R. J. Real-time coherent diffraction inversion using deep generative networks. *Sci. Rep.* **8**, 16520 (2018).
103. Ren, Z., Xu, Z. & Lam, E. Y. End-to-end deep learning framework for digital holographic reconstruction. *Adv. Photonics* **1**, 1 (2019).
104. Yin, D. *et al.* Digital Holographic Reconstruction Based on Deep Learning Framework With Unpaired Data. *IEEE Photonics J.* **12**, 1–12 (2020).

105. Lee, C., Song, G., Kim, H., Ye, J. C. & Jang, M. Deep learning based on parameterized physical forward model for adaptive holographic imaging with unpaired data. *Nat. Mach. Intell.* **5**, 35–45 (2023).
106. Hu, L., Hu, S., Gong, W. & Si, K. Deep learning assisted Shack–Hartmann wavefront sensor for direct wavefront detection. *Opt. Lett.* **45**, 3741 (2020).
107. Wang, K. *et al.* Transport of intensity equation from a single intensity image via deep learning. *Opt. Lasers Eng.* **134**, 106233 (2020).
108. Pirone, D. *et al.* Speeding up reconstruction of 3D tomograms in holographic flow cytometry via deep learning. *Lab. Chip* **22**, 793–804 (2022).
109. Xue, Y., Cheng, S., Li, Y. & Tian, L. Reliable deep-learning-based phase imaging with uncertainty quantification. *Optica* **6**, 618 (2019).
110. Li, X. *et al.* Quantitative phase imaging via a cGAN network with dual intensity images captured under centrosymmetric illumination. *Opt. Lett.* **44**, 2879 (2019).
111. Wang, K., Kemao, Q., Di, J. & Zhao, J. Y4-Net: a deep learning solution to one-shot dual-wavelength digital holographic reconstruction. *Opt. Lett.* **45**, 4220 (2020).
112. Zeng, T., So, H. K.-H. & Lam, E. Y. RedCap: residual encoder-decoder capsule network for holographic image reconstruction. *Opt. Express* **28**, 4876 (2020).
113. Wu, L., Juhas, P., Yoo, S. & Robinson, I. Complex imaging of phase domains by deep neural networks. *IUCrJ* **8**, 12–21 (2021).
114. Huang, L. *et al.* Holographic Image Reconstruction with Phase Recovery and Autofocusing Using Recurrent Neural Networks. *ACS Photonics* **8**, 1763–1774 (2021).
115. Uelwer, T., Hoffmann, T. & Harmeling, S. Non-iterative Phase Retrieval with Cascaded Neural Networks. in *Artificial Neural Networks and Machine Learning – ICANN 2021* (eds. Farkaš, I., Masulli, P., Otte, S. & Wermter, S.) vol. 12892 295–306 (Springer International Publishing, 2021).
116. Castaneda, R., Trujillo, C. & Doblas, A. Video-Rate Quantitative Phase Imaging Using a Digital Holographic Microscope and a Generative Adversarial Network. *Sensors* **21**, 8021 (2021).

117. Jaferzadeh, K. & Fevens, T. HoloPhaseNet: fully automated deep-learning-based hologram reconstruction using a conditional generative adversarial model. *Biomed. Opt. Express* **13**, 4032 (2022).
118. Luo, W., Zhang, Y., Shu, X., Niu, M. & Zhou, R. Learning end-to-end phase retrieval using only one interferogram with mixed-context network. in *Quantitative Phase Imaging VIII* (eds. Popescu, G., Park, Y. & Liu, Y.) 26 (SPIE, 2022). doi:10.1117/12.2610502.
119. Ding, H. *et al.* ContransGAN: Convolutional Neural Network Coupling Global Swin-Transformer Network for High-Resolution Quantitative Phase Imaging with Unpaired Data. *Cells* **11**, 2394 (2022).
120. Ye, Q., Wang, L.-W. & Lun, D. P. K. SiSPRNet: end-to-end learning for single-shot phase retrieval. *Opt. Express* **30**, 31937 (2022).
121. Chen, H., Huang, L., Liu, T. & Ozcan, A. Fourier Imager Network (FIN): A deep neural network for hologram reconstruction with superior external generalization. *Light Sci. Appl.* **11**, 254 (2022).
122. Chen, H., Huang, L., Liu, T. & Ozcan, A. eFIN: Enhanced Fourier Imager Network for Generalizable Autofocusing and Pixel Super-Resolution in Holographic Imaging. *IEEE J. Sel. Top. Quantum Electron.* **29**, 1–10 (2023).
123. Shu, X., Niu, M., Zhang, Y. & Zhou, R. NAS-PRNet: Neural Architecture Search generated Phase Retrieval Net for Off-axis Quantitative Phase Imaging. Preprint at <https://doi.org/10.48550/arXiv.2210.14231> (2022).
124. Boominathan, L., Maniparambil, M., Gupta, H., Baburajan, R. & Mitra, K. Phase retrieval for Fourier Ptychography under varying amount of measurements. Preprint at <https://doi.org/10.48550/arXiv.1805.03593> (2018).
125. Wang, F. *et al.* Phase imaging with an untrained neural network. *Light Sci. Appl.* **9**, 77 (2020).
126. Zhang, X., Wang, F. & Situ, G. BlindNet: an untrained learning approach toward computational imaging with model uncertainty. *J. Phys. Appl. Phys.* **55**, 034001 (2022).
127. Yang, D. *et al.* Coherent modulation imaging using a physics-driven neural network. *Opt. Express* **30**, 35647 (2022).

128. Yang, D. *et al.* Dynamic coherent diffractive imaging with a physics-driven untrained learning method. *Opt. Express* **29**, 31426 (2021).
129. Bai, C. *et al.* Dual-wavelength in-line digital holography with untrained deep neural networks. *Photonics Res.* **9**, 2501 (2021).
130. Galande, A. S., Thapa, V., Gurram, H. P. R. & John, R. Untrained deep network powered with explicit denoiser for phase recovery in inline holography. *Appl. Phys. Lett.* **122**, 133701 (2023).
131. Yao, Y. *et al.* AutoPhaseNN: unsupervised physics-aware deep learning of 3D nanoscale Bragg coherent diffraction imaging. *Npj Comput. Mater.* **8**, 124 (2022).
132. Li, R., Pedrini, G., Huang, Z., Reichelt, S. & Cao, L. Physics-enhanced neural network for phase retrieval from two diffraction patterns. *Opt. Express* **30**, 32680 (2022).
133. Bouchama, L., Dorizzi, B., Klossa, J. & Gottesman, Y. A physics-inspired deep learning framework for an efficient FPM reconstruction under low overlap conditions. Preprint at <https://doi.org/10.1364/opticaopen.22310506.v1> (2023).
134. Huang, L., Chen, H., Liu, T. & Ozcan, A. GedankenNet: Self-supervised learning of hologram reconstruction using physics consistency. Preprint at <https://doi.org/10.48550/arXiv.2209.08288> (2022).
135. Neto, A. M. *et al.* Image processing using Pearson's correlation coefficient: Applications on autonomous robotics. in *2013 13th International Conference on Autonomous Robot Systems* 1–6 (IEEE, 2013). doi:10.1109/Robotica.2013.6623521.
136. Tayal, K., Lai, C.-H., Kumar, V. & Sun, J. Inverse Problems, Deep Learning, and Symmetry Breaking. Preprint at <https://doi.org/10.48550/arXiv.2003.09077> (2020).
137. Wang, K. *et al.* Deep learning wavefront sensing and aberration correction in atmospheric turbulence. *PhotoniX* **2**, 8 (2021).
138. Li, H., Chen, X., Chi, Z., Mann, C. & Razi, A. Deep DIH: Single-Shot Digital In-Line Holography Reconstruction by Deep Learning. *IEEE Access* **8**, 202648–202659 (2020).
139. Zhang, J. *et al.* The integration of neural network and physical reconstruction model for Fourier ptychographic microscopy. *Opt. Commun.* **504**, 127470 (2022).

140. Chen, X., Wang, H., Razi, A., Kozicki, M. & Mann, C. DH-GAN: a physics-driven untrained generative adversarial network for holographic imaging. *Opt. Express* **31**, 10114 (2023).
141. Rivenson, Y., Zhang, Y., Günaydin, H., Teng, D. & Ozcan, A. Phase recovery and holographic image reconstruction using deep learning in neural networks. *Light Sci. Appl.* **7**, 17141 (2018).
142. Wu, Y. *et al.* Extended depth-of-field in holographic imaging using deep-learning-based autofocusing and phase recovery. *Optica* **5**, 704 (2018).
143. Deng, M., Goy, A., Li, S., Arthur, K. & Barbastathis, G. Probing shallower: perceptual loss trained Phase Extraction Neural Network (PLT-PhENN) for artifact-free reconstruction at low photon budget. *Opt. Express* **28**, 2511 (2020).
144. Deng, M., Li, S., Goy, A., Kang, I. & Barbastathis, G. Learning to synthesize: robust phase retrieval at low photon counts. *Light Sci. Appl.* **9**, 36 (2020).
145. Kang, I., Zhang, F. & Barbastathis, G. Phase extraction neural network (PhENN) with coherent modulation imaging (CMI) for phase retrieval at low photon counts. *Opt. Express* **28**, 21578 (2020).
146. Zhang, J., Xu, T., Shen, Z., Qiao, Y. & Zhang, Y. Fourier ptychographic microscopy reconstruction with multiscale deep residual network. *Opt. Express* **27**, 8612 (2019).
147. Moon, I., Jaferzadeh, K., Kim, Y. & Javidi, B. Noise-free quantitative phase imaging in Gabor holography with conditional generative adversarial network. *Opt. Express* **28**, 26284 (2020).
148. Metzler, C. A., Schniter, P., Veeraraghavan, A. & Baraniuk, R. G. prDeep: Robust Phase Retrieval with a Flexible Deep Network. Preprint at <http://arxiv.org/abs/1803.00212> (2018).
149. Wu, Z., Sun, Y., Liu, J. & Kamilov, U. Online Regularization by Denoising with Applications to Phase Retrieval. in *2019 IEEE/CVF International Conference on Computer Vision Workshop (ICCVW)* 3887–3895 (IEEE, 2019). doi:10.1109/ICCVW.2019.00482.
150. Bai, C. *et al.* Robust contrast-transfer-function phase retrieval via flexible deep learning networks. *Opt. Lett.* **44**, 5141 (2019).
151. Wang, Y., Sun, X. & Fleischer, J. W. When deep denoising meets iterative phase retrieval. Preprint at <http://arxiv.org/abs/2003.01792> (2020).
152. Chang, X., Bian, L. & Zhang, J. Large-scale phase retrieval. *eLight* **1**, 4 (2021).

153. İşil, Ç., Oktem, F. S. & Koç, A. Deep iterative reconstruction for phase retrieval. *Appl. Opt.* **58**, 5422 (2019).
154. Kumar, S. Phase retrieval with physics informed zero-shot network. *Opt. Lett.* **46**, 5942 (2021).
155. Jagatap, G. & Hegde, C. Phase Retrieval using Untrained Neural Network Priors. in *NeurIPS 2019 Workshop on Solving Inverse Problems with Deep Networks* (2019).
156. Jagatap, G. & Hegde, C. Algorithmic Guarantees for Inverse Imaging with Untrained Network Priors. in *Advances in Neural Information Processing Systems 32* (2019).
157. Zhou, K. C. & Horstmeyer, R. Diffraction tomography with a deep image prior. *Opt. Express* **28**, 12872 (2020).
158. Shamshad, F., Hanif, A. & Ahmed, A. Subsampled Fourier Ptychography using Pretrained Invertible and Untrained Network Priors. Preprint at <http://arxiv.org/abs/2005.07026> (2020).
159. Bostan, E., Heckel, R., Chen, M., Kellman, M. & Waller, L. Deep phase decoder: self-calibrating phase microscopy with an untrained deep neural network. *Optica* **7**, 559 (2020).
160. Lawrence, H., Barmherzig, D. A., Li, H., Eickenberg, M. & Gabrié, M. Phase Retrieval with Holography and Untrained Priors: Tackling the Challenges of Low-Photon Nanoscale Imaging. Preprint at <http://arxiv.org/abs/2012.07386> (2021).
161. Niknam, F., Qazvini, H. & Latifi, H. Holographic optical field recovery using a regularized untrained deep decoder network. *Sci. Rep.* **11**, 10903 (2021).
162. Ma, L., Wang, H., Leng, N. & Yuan, Z. ADMM based Fourier phase retrieval with untrained generative prior. Preprint at <http://arxiv.org/abs/2210.12646> (2022).
163. Chen, Q., Huang, D. & Chen, R. Fourier ptychographic microscopy with untrained deep neural network priors. *Opt. Express* **30**, 39597 (2022).
164. Hand, P., Leong, O. & Voroninski, V. Phase Retrieval Under a Generative Prior. in *Advances in Neural Information Processing Systems 31* (2018).
165. Shamshad, F. & Ahmed, A. Robust Compressive Phase Retrieval via Deep Generative Priors. Preprint at <https://doi.org/10.48550/arXiv.1808.05854> (2018).

166. Shamshad, F., Abbas, F. & Ahmed, A. Deep Ptych: Subsampled Fourier Ptychography Using Generative Priors. in *ICASSP 2019 - 2019 IEEE International Conference on Acoustics, Speech and Signal Processing (ICASSP)* 7720–7724 (IEEE, 2019). doi:10.1109/ICASSP.2019.8682179.
167. Shamshad, F. & Ahmed, A. Compressed Sensing-Based Robust Phase Retrieval via Deep Generative Priors. *IEEE Sens. J.* **21**, 2286–2298 (2021).
168. Hyder, R., Shah, V., Hegde, C. & Asif, M. S. Alternating Phase Projected Gradient Descent with Generative Priors for Solving Compressive Phase Retrieval. in *ICASSP 2019 - 2019 IEEE International Conference on Acoustics, Speech and Signal Processing (ICASSP)* 7705–7709 (IEEE, 2019). doi:10.1109/ICASSP.2019.8682811.
169. Uelwer, T., Konietzny, S. & Harmeling, S. Optimizing Intermediate Representations of Generative Models for Phase Retrieval. Preprint at <https://doi.org/10.48550/arXiv.2205.15617> (2022).
170. Wang, C.-J., Wen, C.-K., Tsai, S.-H. & Jin, S. Phase Retrieval With Learning Unfolded Expectation Consistent Signal Recovery Algorithm. *IEEE Signal Process. Lett.* **27**, 780–784 (2020).
171. Naimipour, N., Khobahi, S. & Soltanalian, M. UPR: A Model-Driven Architecture for Deep Phase Retrieval. in *2020 54th Asilomar Conference on Signals, Systems, and Computers* 205–209 (IEEE, 2020). doi:10.1109/IEEECONF51394.2020.9443438.
172. Naimipour, N., Khobahi, S. & Soltanalian, M. Unfolded Algorithms for Deep Phase Retrieval. Preprint at <https://doi.org/10.48550/arXiv.2012.11102> (2020).
173. Zhang, F. *et al.* Physics-based Iterative Projection Complex Neural Network for Phase Retrieval in Lensless Microscopy Imaging. in *2021 IEEE/CVF Conference on Computer Vision and Pattern Recognition (CVPR)* 10518–10526 (IEEE, 2021). doi:10.1109/CVPR46437.2021.01038.
174. BaoShun, S. & QiuSheng, L. DualPRNet: Deep Shrinkage Dual Frame Network for Deep Unrolled Phase Retrieval. *IEEE Signal Process. Lett.* **29**, 1177–1181 (2022).
175. Wu, X., Wu, Z., Shanmugavel, S. C., Yu, H. Z. & Zhu, Y. Physics-informed neural network for phase imaging based on transport of intensity equation. *Opt. Express* **30**, 43398 (2022).

176. Yang, Y., Lian, Q., Zhang, X., Zhang, D. & Zhang, H. HIONet: Deep priors based deep unfolded network for phase retrieval. *Digit. Signal Process.* **132**, 103797 (2022).
177. Wang, W., Huang, Q., You, S., Yang, C. & Neumann, U. Shape Inpainting Using 3D Generative Adversarial Network and Recurrent Convolutional Networks. in *2017 IEEE International Conference on Computer Vision (ICCV)* 2317–2325 (IEEE, 2017).  
doi:10.1109/ICCV.2017.252.
178. Romano, Y., Elad, M. & Milanfar, P. The Little Engine That Could: Regularization by Denoising (RED). *SIAM J. Imaging Sci.* **10**, 1804–1844 (2017).
179. Goldstein, T., Studer, C. & Baraniuk, R. A Field Guide to Forward-Backward Splitting with a FASTA Implementation. Preprint at <https://doi.org/10.48550/arXiv.1411.3406> (2014).
180. Ulyanov, D., Vedaldi, A. & Lempitsky, V. Deep Image Prior. in *Proceedings of the IEEE Conference on Computer Vision and Pattern Recognition (CVPR)* 9446–9454 (2018).
181. Heckel, R. & Hand, P. Deep Decoder: Concise Image Representations from Untrained Non-convolutional Networks. Preprint at <https://doi.org/10.48550/arXiv.1810.03982> (2018).
182. Gregor, K. & LeCun, Y. Learning Fast Approximations of Sparse Coding. in *Proceedings of the 27th International Conference on International Conference on Machine Learning* 399–406 (Omnipress, 2010).
183. Jeon, W., Jeong, W., Son, K. & Yang, H. Speckle noise reduction for digital holographic images using multi-scale convolutional neural networks. *Opt. Lett.* **43**, 4240 (2018).
184. Choi, G. *et al.* Cycle-consistent deep learning approach to coherent noise reduction in optical diffraction tomography. *Opt. Express* **27**, 4927 (2019).
185. Zhang, J., Tian, X., Shao, J., Luo, H. & Liang, R. Phase unwrapping in optical metrology via denoised and convolutional segmentation networks. *Opt. Express* **27**, 14903 (2019).
186. Yan, K., Yu, Y., Sun, T., Asundi, A. & Kemo, Q. Wrapped phase denoising using convolutional neural networks. *Opt. Lasers Eng.* **128**, 105999 (2020).
187. Yan, K., Chang, L., Andrianakis, M., Tornari, V. & Yu, Y. Deep Learning-Based Wrapped Phase Denoising Method for Application in Digital Holographic Speckle Pattern Interferometry. *Appl. Sci.* **10**, 4044 (2020).

188. Montresor, S., Tahon, M., Laurent, A. & Picart, P. Computational de-noising based on deep learning for phase data in digital holographic interferometry. *APL Photonics* **5**, 030802 (2020).
189. Tahon, M., Montresor, S. & Picart, P. Towards Reduced CNNs for De-Noising Phase Images Corrupted with Speckle Noise. *Photonics* **8**, 255 (2021).
190. Tahon, M., Montrésor, S. & Picart, P. Deep Learning Network for Speckle De-Noising in Severe Conditions. *J. Imaging* **8**, 165 (2022).
191. Fang, Q. *et al.* Speckle denoising based on deep learning via a conditional generative adversarial network in digital holographic interferometry. *Opt. Express* **30**, 20666 (2022).
192. Murdaca, G., Rucci, A. & Prati, C. Deep Learning for InSAR Phase Filtering: An Optimized Framework for Phase Unwrapping. *Remote Sens.* **14**, 4956 (2022).
193. Tang, J., Zhang, J., Wu, J., Di, J. & Zhao, J. Coherent Noise Suppression of Single-Shot Digital Holographic Phase Via an Untrained Self-Supervised Network. *Front. Photonics* **3**, 907847 (2022).
194. Liu, T. *et al.* Deep learning-based super-resolution in coherent imaging systems. Preprint at <https://doi.org/10.48550/arXiv.1810.06611> (2018).
195. Liu, T. *et al.* Deep learning-based super-resolution in coherent imaging systems. *Sci. Rep.* **9**, 3926 (2019).
196. Jiao, Y. *et al.* Computational interference microscopy enabled by deep learning. *APL Photonics* **6**, 046103 (2021).
197. Butola, A. *et al.* High space-bandwidth in quantitative phase imaging using partially spatially coherent digital holographic microscopy and a deep neural network. *Opt. Express* **28**, 36229 (2020).
198. Meng, Z. *et al.* DL-SI-DHM: a deep network generating the high-resolution phase and amplitude images from wide-field images. *Opt. Express* **29**, 19247 (2021).
199. Li, A.-C. *et al.* Patch-Based U-Net Model for Isotropic Quantitative Differential Phase Contrast Imaging. *IEEE Trans. Med. Imaging* **40**, 3229–3237 (2021).

200. Gupta, R. K., Hempler, N., Malcolm, G. P. A., Dholakia, K. & Powis, S. J. High throughput hemogram of T cells using digital holographic microscopy and deep learning. *Opt. Contin.* **2**, 670 (2023).
201. Lim, J., Ayoub, A. B. & Psaltis, D. Three-dimensional tomography of red blood cells using deep learning. *Adv. Photonics* **2**, 1 (2020).
202. Ryu, D. *et al.* DeepRegularizer: Rapid Resolution Enhancement of Tomographic Imaging Using Deep Learning. *IEEE Trans. Med. Imaging* **40**, 1508–1518 (2021).
203. Nguyen, T. *et al.* Automatic phase aberration compensation for digital holographic microscopy based on deep learning background detection. *Opt. Express* **25**, 15043 (2017).
204. Ma, S. *et al.* Phase-aberration compensation via deep learning in digital holographic microscopy. *Meas. Sci. Technol.* **32**, 105203 (2021).
205. Lin, L.-C., Huang, C.-H., Chen, Y.-F., Chu, D. & Cheng, C.-J. Deep learning-assisted wavefront correction with sparse data for holographic tomography. *Opt. Lasers Eng.* **154**, 107010 (2022).
206. Xiao, W. *et al.* Sensing morphogenesis of bone cells under microfluidic shear stress by holographic microscopy and automatic aberration compensation with deep learning. *Lab. Chip* **21**, 1385–1394 (2021).
207. Zhang, G. *et al.* Fast phase retrieval in off-axis digital holographic microscopy through deep learning. *Opt. Express* **26**, 19388 (2018).
208. Tang, J. *et al.* Phase aberration compensation via a self-supervised sparse constraint network in digital holographic microscopy. *Opt. Lasers Eng.* **168**, 107671 (2023).
209. Dardikman, G. & Shaked, N. T. Phase Unwrapping Using Residual Neural Networks. in *Imaging and Applied Optics 2018 (3D, AO, AIO, COSI, DH, IS, LACSEA, LS&C, MATH, pcaOP)* CW3B.5 (OSA, 2018). doi:10.1364/COSI.2018.CW3B.5.
210. Dardikman, G., Turko, N. A. & Shaked, N. T. Deep learning approaches for unwrapping phase images with steep spatial gradients: a simulation. in *2018 IEEE International Conference on the Science of Electrical Engineering in Israel (ICSEE)* 1–4 (IEEE, 2018). doi:10.1109/ICSEE.2018.8646266.

211. Wang, K., Li, Y., Kemao, Q., Di, J. & Zhao, J. One-step robust deep learning phase unwrapping. *Opt. Express* **27**, 15100 (2019).
212. He, J. J., Sandino, C., Zeng, D., Vasanawala, S. & Cheng, J. Deep spatiotemporal phase unwrapping of phase-contrast MRI data. in *Proceedings of the 27th ISMRM Annual Meeting & Exhibition, Montréal, QC, Canada* 11–16 (2019).
213. Ryu, K., Gho, S.-M., Nam, Y., Koch, K. & Kim, D.-H. Development of a deep learning method for phase unwrapping MR images. in *Proc. Intl. Soc. Mag. Reson. Med.* vol. 27 ,4707 (2019).
214. Dardikman, G. *et al.* PhUn-Net: ready-to-use neural network for unwrapping quantitative phase images of biological cells. *Biomed. Opt. Express* **11**, 1107 (2020).
215. Qin, Y. *et al.* Direct and accurate phase unwrapping with deep neural network. *Appl. Opt.* **59**, 7258 (2020).
216. Perera, M. V. & De Silva, A. A Joint Convolutional and Spatial Quad-Directional LSTM Network for Phase Unwrapping. in *IEEE International Conference on Acoustics, Speech and Signal Processing (ICASSP)* 4055–4059 (2021). doi:10.1109/ICASSP39728.2021.9414748.
217. Park, S., Kim, Y. & Moon, I. Automated phase unwrapping in digital holography with deep learning. *Biomed. Opt. Express* **12**, 7064 (2021).
218. Zhou, H. *et al.* The PHU-NET: A robust phase unwrapping method for MRI based on deep learning. *Magn. Reson. Med.* **86**, 3321–3333 (2021).
219. Xu, M., Tang, C., Shen, Y., Hong, N. & Lei, Z. PU-M-Net for phase unwrapping with speckle reduction and structure protection in ESPI. *Opt. Lasers Eng.* **151**, 106824 (2022).
220. Zhou, L., Yu, H., Pascazio, V. & Xing, M. PU-GAN: A One-Step 2-D InSAR Phase Unwrapping Based on Conditional Generative Adversarial Network. *IEEE Trans. Geosci. Remote Sens.* **60**, 1–10 (2022).
221. Xie, X. *et al.* Deep learning phase-unwrapping method based on adaptive noise evaluation. *Appl. Opt.* **61**, 6861 (2022).
222. Zhao, J. *et al.* VDE-Net: a two-stage deep learning method for phase unwrapping. *Opt. Express* **30**, 39794 (2022).

223. Liang, R., Zhang, J., Tian, X. & Shao, J. Phase unwrapping using segmentation. *US Provisional Pat.* 62/768,624 (2018).
224. Spoorthi, G. E., Gorthi, S. & Gorthi, R. K. S. S. PhaseNet: A Deep Convolutional Neural Network for Two-Dimensional Phase Unwrapping. *IEEE Signal Process. Lett.* **26**, 54–58 (2018).
225. Spoorthi, G. E., Sai Subrahmanyam Gorthi, R. K. & Gorthi, S. PhaseNet 2.0: Phase Unwrapping of Noisy Data Based on Deep Learning Approach. *IEEE Trans. Image Process.* **29**, 4862–4872 (2020).
226. Liang, R., Zhang, J., Tian, X. & Shao, J. Phase unwrapping using segmentation. *Int. Pat.* WO2020102814A1 (2020).
227. Zhang, T. *et al.* Rapid and robust two-dimensional phase unwrapping via deep learning. *Opt. Express* **27**, 23173 (2019).
228. Zhu, S. *et al.* Phase unwrapping in ICF target interferometric measurement via deep learning. *Appl. Opt.* **60**, 10 (2021).
229. Wu, C. *et al.* Phase unwrapping based on a residual en-decoder network for phase images in Fourier domain Doppler optical coherence tomography. *Biomed. Opt. Express* **11**, 1760 (2020).
230. Zhao, Z., Li, B., Kang, X., Lu, J. & Liu, T. Phase unwrapping method for point diffraction interferometer based on residual auto encoder neural network. *Opt. Lasers Eng.* **138**, 106405 (2020).
231. Vengala, K. S., Paluru, N. & Subrahmanyam Gorthi, R. K. S. 3D deformation measurement in digital holographic interferometry using a multitask deep learning architecture. *J. Opt. Soc. Am. A* **39**, 167 (2022).
232. Vengala, K. S., Ravi, V. & Sai Subrahmanyam, G. R. K. A Multi-task Learning for 2D Phase Unwrapping in Fringe Projection. *IEEE Signal Process. Lett.* **29**, 797–801 (2022).
233. Zhang, J. & Li, Q. EESANet: edge-enhanced self-attention network for two-dimensional phase unwrapping. *Opt. Express* **30**, 10470 (2022).
234. Huang, W. *et al.* Two-dimensional phase unwrapping by a high-resolution deep learning network. *Measurement* **200**, 111566 (2022).

235. Wang, Y., Zhou, C. & Qi, X. PEENet for phase unwrapping in fringe projection profilometry. in *Thirteenth International Conference on Information Optics and Photonics (CIOP 2022)* (ed. Yang, Y.) 163 (SPIE, 2022). doi:10.1117/12.2654763.
236. Zhou, L., Yu, H. & Lan, Y. Deep Convolutional Neural Network-Based Robust Phase Gradient Estimation for Two-Dimensional Phase Unwrapping Using SAR Interferograms. *IEEE Trans. Geosci. Remote Sens.* **58**, 4653–4665 (2020).
237. Wang, H., Hu, J., Fu, H., Wang, C. & Wang, Z. A Novel Quality-Guided Two-Dimensional InSAR Phase Unwrapping Method via GAUNet. *IEEE J. Sel. Top. Appl. Earth Obs. Remote Sens.* **14**, 7840–7856 (2021).
238. Sica, F., Calvanese, F., Scarpa, G. & Rizzoli, P. A CNN-Based Coherence-Driven Approach for InSAR Phase Unwrapping. *IEEE Geosci. Remote Sens. Lett.* **19**, 1–5 (2020).
239. Li, L., Zhang, H., Tang, Y., Wang, C. & Gu, F. InSAR Phase Unwrapping by Deep Learning Based on Gradient Information Fusion. *IEEE Geosci. Remote Sens. Lett.* **19**, 1–5 (2021).
240. Wu, Z., Wang, T., Wang, Y. & Ge, D. A New Phase Unwrapping Method Combining Minimum Cost Flow with Deep Learning. in *2021 IEEE International Geoscience and Remote Sensing Symposium IGARSS* 3177–3180 (IEEE, 2021). doi:10.1109/IGARSS47720.2021.9554886.
241. Wu, Z., Wang, T., Wang, Y., Wang, R. & Ge, D. Deep-Learning-Based Phase Discontinuity Prediction for 2-D Phase Unwrapping of SAR Interferograms. *IEEE Trans. Geosci. Remote Sens.* **60**, 1–16 (2021).
242. Zhou, L., Yu, H., Lan, Y. & Xing, M. Deep Learning-Based Branch-Cut Method for InSAR Two-Dimensional Phase Unwrapping. *IEEE Trans. Geosci. Remote Sens.* **60**, 1–15 (2021).
243. Yu, H., Lan, Y., Yuan, Z., Xu, J. & Lee, H. Phase Unwrapping in InSAR : A Review. *IEEE Geosci. Remote Sens. Mag.* **7**, 40–58 (2019).
244. Popescu, G., Ikeda, T., Dasari, R. R. & Feld, M. S. Diffraction phase microscopy for quantifying cell structure and dynamics. *Opt. Lett.* **31**, 775 (2006).
245. Gao, P., Pedrini, G. & Osten, W. Structured illumination for resolution enhancement and autofocusing in digital holographic microscopy. *Opt. Lett.* **38**, 1328 (2013).

246. Tian, L. & Waller, L. Quantitative differential phase contrast imaging in an LED array microscope. *Opt. Express* **23**, 11394 (2015).
247. Ferraro, P. *et al.* Compensation of the inherent wave front curvature in digital holographic coherent microscopy for quantitative phase-contrast imaging. *Appl. Opt.* **42**, 1938 (2003).
248. Colomb, T. *et al.* Total aberrations compensation in digital holographic microscopy with a reference conjugated hologram. *Opt. Express* **14**, 4300 (2006).
249. Miccio, L. *et al.* Direct full compensation of the aberrations in quantitative phase microscopy of thin objects by a single digital hologram. *Appl. Phys. Lett.* **90**, 041104 (2007).
250. Zuo, C., Chen, Q., Qu, W. & Asundi, A. Phase aberration compensation in digital holographic microscopy based on principal component analysis. *Opt. Lett.* **38**, 1724 (2013).
251. Jenkinson, M. Fast, automated,N-dimensional phase-unwrapping algorithm. *Magn. Reson. Med.* **49**, 193–197 (2003).
252. Su, X. & Chen, W. Fourier transform profilometry: a review. *Opt. Lasers Eng.* **35**, 263–284 (2001).
253. Ghiglia, D. C. & Pritt, M. D. *Two-dimensional phase unwrapping: theory, algorithms, and software*. (Wiley, 1998).
254. Tan, M. & Le, Q. EfficientNet: Rethinking Model Scaling for Convolutional Neural Networks. in *Proceedings of the 36th International Conference on Machine Learning* (eds. Chaudhuri, K. & Salakhutdinov, R.) vol. 97 6105–6114 (PMLR, 2019).
255. Vithin, A. V. S., Vishnoi, A. & Gannavarpu, R. Phase derivative estimation in digital holographic interferometry using a deep learning approach. *Appl. Opt.* **61**, 3061 (2022).
256. Satya Vithin, A. V., Ramaiah, J. & Gannavarpu, R. Deep learning based single shot multiple phase derivative retrieval method in multi-wave digital holographic interferometry. *Opt. Lasers Eng.* **162**, 107442 (2022).
257. Yi, F., Moon, I. & Javidi, B. Automated red blood cells extraction from holographic images using fully convolutional neural networks. *Biomed. Opt. Express* **8**, 4466 (2017).

258. Ahmadzadeh, E., Jaferzadeh, K., Shin, S. & Moon, I. Automated single cardiomyocyte characterization by nucleus extraction from dynamic holographic images using a fully convolutional neural network. *Biomed. Opt. Express* **11**, 1501 (2020).
259. Kandel, M. E. *et al.* Reproductive outcomes predicted by phase imaging with computational specificity of spermatozoon ultrastructure. *Proc. Natl. Acad. Sci.* **117**, 18302–18309 (2020).
260. Goswami, N. *et al.* Label-free SARS-CoV-2 detection and classification using phase imaging with computational specificity. *Light Sci. Appl.* **10**, 176 (2021).
261. Hu, C. *et al.* Live-dead assay on unlabeled cells using phase imaging with computational specificity. *Nat. Commun.* **13**, 713 (2022).
262. He, Y. R. *et al.* Cell Cycle Stage Classification Using Phase Imaging with Computational Specificity. *ACS Photonics* **9**, 1264–1273 (2022).
263. Zhang, J. K., Fanous, M., Sobh, N., Kajdacsy-Balla, A. & Popescu, G. Automatic Colorectal Cancer Screening Using Deep Learning in Spatial Light Interference Microscopy Data. *Cells* **11**, 716 (2022).
264. Jiang, S. *et al.* High-throughput digital pathology via a handheld, multiplexed, and AI-powered ptychographic whole slide scanner. *Lab. Chip* **22**, 2657–2670 (2022).
265. Lee, J. *et al.* Deep-Learning-Based Label-Free Segmentation of Cell Nuclei in Time-Lapse Refractive Index Tomograms. *IEEE Access* **7**, 83449–83460 (2019).
266. Choi, J. *et al.* Label-free three-dimensional analyses of live cells with deep-learning-based segmentation exploiting refractive index distributions. Preprint at <https://doi.org/10.1101/2021.05.23.445351> (2021) doi:10.1101/2021.05.23.445351.
267. Jo, Y. *et al.* Holographic deep learning for rapid optical screening of anthrax spores. *Sci. Adv.* **3**, e1700606 (2017).
268. Karandikar, S. H. *et al.* Reagent-Free and Rapid Assessment of T Cell Activation State Using Diffraction Phase Microscopy and Deep Learning. *Anal. Chem.* **91**, 3405–3411 (2019).
269. Zhang, J. K., He, Y. R. & Sobh, N. Label-free colorectal cancer screening using deep learning and spatial light interference microscopy (SLIM). *APL Photonics* **5**, 040805 (2020).

270. Butola, A. *et al.* High spatially sensitive quantitative phase imaging assisted with deep neural network for classification of human spermatozoa under stressed condition. *Sci. Rep.* **10**, 13118 (2020).
271. Li, Y., Di, J., Ren, L. & Zhao, J. Deep-learning-based prediction of living cells mitosis via quantitative phase microscopy. *Chin. Opt. Lett.* **19**, 051701 (2021).
272. Shu, X. *et al.* Artificial-Intelligence-Enabled Reagent-Free Imaging Hematology Analyzer. *Adv. Intell. Syst.* **3**, 2000277 (2021).
273. Pitkäaho, T., Manninen, A. & Naughton, T. J. Classification of Digital Holograms with Deep Learning and Hand-Crafted Features. in *Imaging and Applied Optics 2018 (3D, AO, AIO, COSI, DH, IS, LACSEA, LS&C, MATH, pcAOP)* DW2F.3 (OSA, 2018).  
doi:10.1364/DH.2018.DW2F.3.
274. O'Connor, T., Anand, A., Andemariam, B. & Javidi, B. Deep learning-based cell identification and disease diagnosis using spatio-temporal cellular dynamics in compact digital holographic microscopy. *Biomed. Opt. Express* **11**, 4491 (2020).
275. O'Connor, T., Shen, J.-B., Liang, B. T. & Javidi, B. Digital holographic deep learning of red blood cells for field-portable, rapid COVID-19 screening. *Opt. Lett.* **46**, 2344 (2021).
276. Ryu, D. *et al.* Label-Free White Blood Cell Classification Using Refractive Index Tomography and Deep Learning. *BME Front.* **2021**, 2021/9893804 (2021).
277. Kim, G. *et al.* Rapid species identification of pathogenic bacteria from a minute quantity exploiting three-dimensional quantitative phase imaging and artificial neural network. *Light Sci. Appl.* **11**, 190 (2022).
278. Wang, H. *et al.* Early detection and classification of live bacteria using time-lapse coherent imaging and deep learning. *Light Sci. Appl.* **9**, 118 (2020).
279. Liu, T. *et al.* Stain-free, rapid, and quantitative viral plaque assay using deep learning and holography. Preprint at <https://doi.org/10.48550/arXiv.2207.00089> (2022).
280. Ben Baruch, S., Rotman-Nativ, N., Baram, A., Greenspan, H. & Shaked, N. T. Cancer-Cell Deep-Learning Classification by Integrating Quantitative-Phase Spatial and Temporal Fluctuations. *Cells* **10**, 3353 (2021).

281. Singla, N. & Srivastava, V. Deep learning enabled multi-wavelength spatial coherence microscope for the classification of malaria-infected stages with limited labelled data size. *Opt. Laser Technol.* **130**, 106335 (2020).
282. Işıl, Ç. *et al.* Phenotypic Analysis of Microalgae Populations Using Label-Free Imaging Flow Cytometry and Deep Learning. *ACS Photonics* **8**, 1232–1242 (2021).
283. Pitkäaho, T., Manninen, A. & Naughton, T. J. Temporal Deep Learning Classification of Digital Hologram Reconstructions of Multicellular Samples. in *Biophotonics Congress: Biomedical Optics Congress 2018 (Microscopy/Translational/Brain/OTS)* JW3A.14 (OSA, 2018). doi:10.1364/TRANSLATIONAL.2018.JW3A.14.
284. Lam, H. H., Tsang, P. W. M. & Poon, T.-C. Ensemble convolutional neural network for classifying holograms of deformable objects. *Opt. Express* **27**, 34050 (2019).
285. Lam, H. H. S., Tsang, P. W. M. & Poon, T.-C. Hologram classification of occluded and deformable objects with speckle noise contamination by deep learning. *J. Opt. Soc. Am. A* **39**, 411 (2022).
286. Lam, H., Zhu, Y. & Buranasiri, P. Off-Axis Holographic Interferometer with Ensemble Deep Learning for Biological Tissues Identification. *Appl. Sci.* **12**, 12674 (2022).
287. Terbe, D., Orzó, L. & Zarányi, Á. Classification of Holograms with 3D-CNN. *Sensors* **22**, 8366 (2022).
288. Wu, Y. *et al.* Label-Free Bioaerosol Sensing Using Mobile Microscopy and Deep Learning. *ACS Photonics* **5**, 4617–4627 (2018).
289. Wu, Y. *et al.* Bright-field holography: cross-modality deep learning enables snapshot 3D imaging with bright-field contrast using a single hologram. *Light Sci. Appl.* **8**, 25 (2019).
290. Terbe, D., Orzó, L. & Zarányi, Á. Deep-learning-based bright-field image generation from a single hologram using an unpaired dataset. *Opt. Lett.* **46**, 5567 (2021).
291. Rivenson, Y. *et al.* PhaseStain: the digital staining of label-free quantitative phase microscopy images using deep learning. *Light Sci. Appl.* **8**, 23 (2019).
292. Wang, R. *et al.* Virtual brightfield and fluorescence staining for Fourier ptychography via unsupervised deep learning. *Opt. Lett.* **45**, 5405 (2020).

293. Liu, T. *et al.* Deep learning-based color holographic microscopy. *J. Biophotonics* **12**, e201900107 (2019).
294. Nygate, Y. N. *et al.* Holographic virtual staining of individual biological cells. *Proc. Natl. Acad. Sci.* **117**, 9223–9231 (2020).
295. Guo, S.-M. *et al.* Revealing architectural order with quantitative label-free imaging and deep learning. *eLife* **9**, e55502 (2020).
296. Kandel, M. E. *et al.* Phase imaging with computational specificity (PICS) for measuring dry mass changes in sub-cellular compartments. *Nat. Commun.* **11**, 6256 (2020).
297. Kandel, M. E. *et al.* Multiscale Assay of Unlabeled Neurite Dynamics Using Phase Imaging with Computational Specificity. *ACS Sens.* **6**, 1864–1874 (2021).
298. Guo, S., Ma, Y., Pan, Y., Smith, Z. J. & Chu, K. Organelle-specific phase contrast microscopy enables gentle monitoring and analysis of mitochondrial network dynamics. *Biomed. Opt. Express* **12**, 4363 (2021).
299. Chen, X. *et al.* Artificial confocal microscopy for deep label-free imaging. Preprint at <https://doi.org/10.48550/arXiv.2110.14823> (2021).
300. Chen, X. *et al.* Artificial confocal microscopy for deep label-free imaging. *Nat. Photonics* **17**, 250–258 (2023).
301. Jo, Y. Label-free multiplexed microtomography of endogenous subcellular dynamics using generalizable deep learning. *Nat. Cell Biol.* **23**, 1329–1337 (2021).
302. Long, J., Shelhamer, E. & Darrell, T. Fully Convolutional Networks for Semantic Segmentation. in *Proceedings of the IEEE Conference on Computer Vision and Pattern Recognition (CVPR)* (2015).
303. Yi, F., Moon, I., Javidi, B., Boss, D. & Marquet, P. Automated segmentation of multiple red blood cells with digital holographic microscopy. *J. Biomed. Opt.* **18**, 026006 (2013).
304. Nguyen, T. H. *et al.* Automatic Gleason grading of prostate cancer using quantitative phase imaging and machine learning. *J. Biomed. Opt.* **22**, 036015 (2017).
305. Valentino, M. *et al.* Digital holographic approaches to the detection and characterization of microplastics in water environments. *Appl. Opt.* **62**, D104 (2023).

306. Chang, C.-C. & Lin, C.-J. LIBSVM: A library for support vector machines. *ACM Trans. Intell. Syst. Technol.* **2**, 1–27 (2011).
307. Roitshtain, D. *et al.* Quantitative phase microscopy spatial signatures of cancer cells. *Cytometry A* **91**, 482–493 (2017).
308. Mirsky, S. K., Barnea, I., Levi, M., Greenspan, H. & Shaked, N. T. Automated analysis of individual sperm cells using stain-free interferometric phase microscopy and machine learning: Sperm Analysis Using Interferometry and Machine Learning. *Cytometry A* **91**, 893–900 (2017).
309. Ozaki, Y. *et al.* Label-free classification of cells based on supervised machine learning of subcellular structures. *PLOS ONE* **14**, e0211347 (2019).
310. Bianco, V. *et al.* Microplastic Identification via Holographic Imaging and Machine Learning. *Adv. Intell. Syst.* **2**, 1900153 (2020).
311. Belashov, A. V. *et al.* In vitro monitoring of photoinduced necrosis in HeLa cells using digital holographic microscopy and machine learning. *J. Opt. Soc. Am. A* **37**, 346 (2020).
312. Lam, V. K. *et al.* Quantitative scoring of epithelial and mesenchymal qualities of cancer cells using machine learning and quantitative phase imaging. *J. Biomed. Opt.* **25**, 026002–026002 (2020).
313. Nissim, N., Dudaie, M., Barnea, I. & Shaked, N. T. Real-Time Stain-Free Classification of Cancer Cells and Blood Cells Using Interferometric Phase Microscopy and Machine Learning. *Cytometry A* **99**, 511–523 (2021).
314. Bianco, V., Pirone, D., Memmolo, P., Merola, F. & Ferraro, P. Identification of Microplastics Based on the Fractal Properties of Their Holographic Fingerprint. *ACS Photonics* **8**, 2148–2157 (2021).
315. Yoon, J. *et al.* Identification of non-activated lymphocytes using three-dimensional refractive index tomography and machine learning. *Sci. Rep.* **7**, 6654 (2017).
316. Park, S. *et al.* Label-Free Tomographic Imaging of Lipid Droplets in Foam Cells for Machine-Learning-Assisted Therapeutic Evaluation of Targeted Nanodrugs. *ACS Nano* **14**, 1856–1865 (2020).
317. Chen, C. L. *et al.* Deep Learning in Label-free Cell Classification. *Sci. Rep.* **6**, 21471 (2016).

318. Kim, G., Jo, Y., Cho, H., Min, H. & Park, Y. Learning-based screening of hematologic disorders using quantitative phase imaging of individual red blood cells. *Biosens. Bioelectron.* **123**, 69–76 (2019).
319. Javidi, B. *et al.* Sickle cell disease diagnosis based on spatio-temporal cell dynamics analysis using 3D printed shearing digital holographic microscopy. *Opt. Express* **26**, 13614 (2018).
320. Paidi, S. K. *et al.* Raman and quantitative phase imaging allow morpho-molecular recognition of malignancy and stages of B-cell acute lymphoblastic leukemia. *Biosens. Bioelectron.* **190**, 113403 (2021).
321. Pirone, D. *et al.* Identification of drug-resistant cancer cells in flow cytometry combining 3D holographic tomography with machine learning. *Sens. Actuators B Chem.* **375**, 132963 (2023).
322. Li, Y. *et al.* Accurate label-free 3-part leukocyte recognition with single cell lens-free imaging flow cytometry. *Comput. Biol. Med.* **96**, 147–156 (2018).
323. Memmolo, P. *et al.* Differential diagnosis of hereditary anemias from a fraction of blood drop by digital holography and hierarchical machine learning. *Biosens. Bioelectron.* **201**, 113945 (2022).
324. Valentino, M. *et al.* Intelligent polarization-sensitive holographic flow-cytometer: Towards specificity in classifying natural and microplastic fibers. *Sci. Total Environ.* **815**, 152708 (2022).
325. Kim, S.-J. *et al.* Deep transfer learning-based hologram classification for molecular diagnostics. *Sci. Rep.* **8**, 17003 (2018).
326. Zhu, Y., Yeung, C. H. & Lam, E. Y. Digital holographic imaging and classification of microplastics using deep transfer learning. *Appl. Opt.* **60**, A38 (2021).
327. Zhu, Y., Yeung, C. H. & Lam, E. Y. Microplastic pollution monitoring with holographic classification and deep learning. *J. Phys. Photonics* **3**, 024013 (2021).
328. Zhu, Y., Lo, H. K. A., Yeung, C. H. & Lam, E. Y. Microplastic pollution assessment with digital holography and zero-shot learning. *APL Photonics* **7**, 076102 (2022).
329. Delli Priscoli, M. *et al.* Neuroblastoma Cells Classification Through Learning Approaches by Direct Analysis of Digital Holograms. *IEEE J. Sel. Top. Quantum Electron.* **27**, 1–9 (2021).

330. Zhu, J.-Y., Park, T., Isola, P. & Efros, A. A. Unpaired Image-to-Image Translation using Cycle-Consistent Adversarial Networks. in *Proceedings of the IEEE International Conference on Computer Vision (ICCV)* 2223–2232 (2017).
331. Gatys, L. A., Ecker, A. S. & Bethge, M. Image Style Transfer Using Convolutional Neural Networks. in *Proceedings of the IEEE Conference on Computer Vision and Pattern Recognition (CVPR)* 2414–2423 (2016).
332. Zhu, S., Guo, E., Gu, J., Bai, L. & Han, J. Imaging through unknown scattering media based on physics-informed learning. *Photonics Res.* **9**, B210 (2021).
333. Kendall, A. & Gal, Y. What Uncertainties Do We Need in Bayesian Deep Learning for Computer Vision? in *Advances in Neural Information Processing Systems* (eds. Guyon, I. et al.) vol. 30 (Curran Associates, Inc., 2017).
334. Wei, Z. & Chen, X. Uncertainty Quantification in Inverse Scattering Problems With Bayesian Convolutional Neural Networks. *IEEE Trans. Antennas Propag.* **69**, 3409–3418 (2021).
335. Feng, S., Zuo, C., Hu, Y., Li, Y. & Chen, Q. Deep-learning-based fringe-pattern analysis with uncertainty estimation. *Optica* **8**, 1507 (2021).
336. Gawlikowski, J. *et al.* A Survey of Uncertainty in Deep Neural Networks. Preprint at <https://doi.org/10.48550/arXiv.2107.03342> (2021).
337. Wetzstein, G. *et al.* Inference in artificial intelligence with deep optics and photonics. *Nature* **588**, 39–47 (2020).
338. Shastri, B. J. *et al.* Photonics for artificial intelligence and neuromorphic computing. *Nat. Photonics* **15**, 102–114 (2021).
339. Lin, X. *et al.* All-optical machine learning using diffractive deep neural networks. *Science* **361**, 1004–1008 (2018).
340. Sakib Rahman, M. S. & Ozcan, A. Computer-Free, All-Optical Reconstruction of Holograms Using Diffractive Networks. *ACS Photonics* **8**, 3375–3384 (2021).
341. Mengu, D. & Ozcan, A. All-Optical Phase Recovery: Diffractive Computing for Quantitative Phase Imaging. *Adv. Opt. Mater.* **10**, 2200281 (2022).